
**UCGE Reports**

**Number 20249**

Department of Geomatics Engineering

# Selected GPS Receiver Enhancements for Weak Signal Acquisition and Tracking

**(URL: http://www.geomatics.ucalgary.ca/research/publications/GradTheses.html)**

**By**

**Wei Yu**

**February 2007**

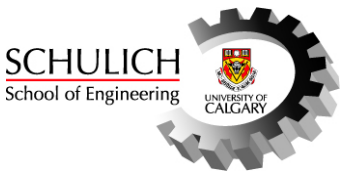

THE UNIVERSITY OF CALGARY

# Selected GPS Receiver Enhancements for Weak Signal Acquisition and Tracking

by

Wei Yu

A THESIS

SUBMITTED TO THE FACULTY OF GRADUATE STUDIES

IN PARTIAL FULFILLMENT OF THE REQUIREMENTS FOR THE

DEGREE OF MASTER OF SCIENCE

DEPARTMENT OF GEOMATICS ENGINEERING

CALGARY, ALBERTA

February, 2007

# Abstract

The sensitivity of a baseband signal processing unit, including both acquisition and tracking, is critical for a GPS receiver to function in perturbed signal enviroments such as indoors and under ionospheric scintillation.. To improve acquisition sensitivity, the differential combining approach, which allows a 2.5 dB improvement in processing loss as compared to noncoherent methods, is proposed herein. This results in a sensitivity improvement ranging from 1.2 dB to 1.6 dB for a given probability of false alarm and missed detection.

Based on an analysis of the Costas-family PLLs, carrier tracking is enhanced by optimizing loop configurations. The decision-directed loop , exhibits a 2 -dB sensitivity improvement as compared to other types of PLLs. Bandwidth and root deviation caused by bilinear or boxcar transforms are solved by implementing a root-controled method. Using this design makes the bandwidth of the digital loop close to desired values, and thus improves carrier tracking by another 1 to 2 dB. A Kalman Filter adopts a soft-mode to deal with the bit sign uncertainty and adjusts the bandwidth to minimize the mean square carrier tracking error. This leads to a 4 dB and 7 dB sensitivity improvement during weak and strong amplitude ionospheric scintillations, respectively.

# Acknowledgements

First of all, I can accomplish this thesis program thanks to the full support from my wife. I can’t imagine where I would be without her support.

Second, I would like to extend my sincere appreciation to my supervisors, Professor Gérard Lachapelle and Professor Susan Skone. Their valuable supervision and constant encouragement makes it possible to accomplish this work.

By taking this opportunity, I extend thanks to my parents for their support to my pursuit in natural science and engineering studies.

The Alberta Informatics Circle of Research Excellence (iCORE) and the GEOIDE Network of Centres of Excellence are acknowledged for their financial support.

I greatly appreciate my colleagues and associates in the PLAN group who helped me to acquire this professional experience. I owe special thanks to Mr. Rob Watson and Dr. Ning Luo for their efforts and patience to make technical comments on my research work. I also thank other PLAN members, namely Mark Petovello, John Schleppe, Jianchen Gao, Gao Mao, Bo Zheng, Jianning Qiu, Donghua Yao, Olivier Julien, Cécile Mongrédien, Surendran Shanmugam, Sanjeet Singh and many others, for their valuable assistence during my stay.

# Table of Contents

# List of Tables

# List of Figures

# Notation

**List of Abbreviations**

| | |
|---|---|
| ABAS | Airborne-Based Augmentation Systems |
| ADC | Analog to Digital Converter |
| AGC | Automatic Gain Controller |
| AGPS | Assisted Global Positioning System |
| ALI | Automatic location identification |
| AVAR | Allan VARiance |
| BER | Bit Error Rate |
| BOC | Binary Offset Carrier |
| BPSK | Binary Phase Shift Keying |
| C/A | GPS Coarse/Acquisition code |
| CBPLL | Constant Bandwidth Phase-Locked Loop |
| CC | Conventional Costas |
| CDMA | Code Division Multiple Access |
| COH | Coherent |
| DD | Decision Directed |
| DFC | Differential Combining |
| DLL | Delay-Locked Loop |

| | |
|---|---|
| DMF | Digital Matched Filter |
| DOD | Department of Defense |
| DOP | Dilution of Precision |
| DOT | Department of Transportation |
| DSP | Digital Signal Processor |
| DV | Decision Variable |
| EGNOS | European Geostationary Navigational Overlay Service |
| ESA | European Space Agency |
| EU | European Union |
| FCC | Federal Communications Commission |
| FE | Front End |
| FFM | Flicker Frequency Modulation |
| FFT | Fast Fourier Transform |
| FLL | Frequency-Locked Loop |
| GBAS | Ground-Based Augmentation Systems |
| GLONASS | GLObal NAvigation Satellite System |
| GM | Gauss-Markov |
| GNSS | Global Navigation Satellite System |
| GPS | Global Positioning System |
| IF | Intermediate Frequency |

| | |
|---|---|
| i.i.d | Independent Identical Distribution |
| KF | Kalman Filter |
| LAAS | Local Area Augmentation System |
| LBS | Location-Based Service |
| LNA | Low Noise Amplifier |
| LO | Local Oscillator |
| LOS | Line Of Sight |
| LS | Least Square |
| MAI | Multiple Access Interference |
| MBCR | Mean Bit Correction Rate |
| MBER | Mean Bit Error Rate |
| MMSE | Minimum Mean Square Error |
| MTBF | Mean Time Between Failure |
| NCH | Noncoherent |
| NLOS | Non Line Of Sight |
| OSC | OSCillator |
| OX | Crystal oscillator |
| P(Y) | GPS Precise (encrypted) code |
| PHN | PHase Noise |
| PLL | Phase-Locked Loop |

| | |
|---|---|
| PSAP | Public-Safety Answering Point |
| PD | Phase Detector (discriminator) |
| PDE | Partial Differential Equation |
| PDF | Probability Density Function |
| PFD | Phase and Frequency Detector (discriminator) |
| PSD | Power Spectrum Density |
| RF | Radio Frequency |
| RHCP | Right Hand Circular Polarization |
| RMS | Root Mean Square |
| RWFM | Random Walk Frequency Modulation |
| SBAS | Satellite-Based Augmentation Systems |
| SDE | Stochastic Differential Equation |
| SL | Squaring Loss |
| SNR | Signal to Noise Ratio |
| SoS | Sum of Square |
| SRIF | Square Root Information Filtering |
| WAAS | Wide Area Augmentation System |
| WFM | White Frequency Modulation |
| WGN | White Gaussian Noise |

**List of Symbols**

| | |
|---|---|
| $\bar{A}$ | Average signal amplitude during one coherent interval |
| $B_{FE}$ | Single-sided bandwidth of front-end |
| $B_L$ | Single-sided target loop bandwidth |
| $B_n$ | Single-sided equivalent noise bandwidth of the loop |
| $C/N_0$ | Carrier to noise density ratio |
| $c(t)$ | Waveform of PRN code sequence |
| $\tilde{c}(t)$ | Filtered waveform of PRN code sequence |
| $d(t)$ | GPS navigation message |
| $d_{correlator}$ | Correlator spacing |
| $\delta A^{Scint}$ | Amplitude variation induced by ionospheric scintillation |
| $\delta I^{Scint}$ | Power variation induced by ionospheric scintillation |
| $\delta t_v$ | Signal transmission delay due to effect of $v$ |
| $\delta\theta^v$ | Signal carrier phase jitter induced by $v$ |
| $E(\cdot)$ | Statistical expectation |
| $f_0^{Osc}$ | Center oscillating frequency |
| $f_s$ | Sampling frequency |
| $f_c$ | PRN code chipping rate |
| $\Gamma(\cdot)$ | Gamma function |
| $H_0$ | Null hypothesis where signal is assumed to be absent |

| | |
|---|---|
| $H_1$ | Alternative hypothesis where signal is assumed to be present |
| $H(f)$ | Transfer function for a linear system |
| $I_{v,k}$ | In-phase output from $v$ correlator |
| $\bar{I}_{v,k}^{m}$ | In-phase output from $v$ correlator normalized by $m$ |
| $I_v(\cdot)$ | $v$-order modified Bessel function of the first kind |
| $K_B$ | Boltzman constant |
| $L_{NCH/DFC}$ | Nonlinear processing loss induced by noncoherent accumulation or DFC |
| $L_Q$ | Largest threshold for quantization |
| $MP(t)$ | Reflected signal due to multipath |
| $n(t)$ | Additive white Gaussian noise |
| $N_0$ | One-sided power spectrum density of thermal noise |
| $N_{NCH}$ | Number of noncoherent accumulations |
| $\omega_d$ | Angle carrier Doppler in radian |
| $\dot{\omega}_d$ | Drift of angle carrier Doppler in rad/s |
| $\hat{\omega}_d$ | Local estimation of angle carrier Doppler |
| $P$ | Signal power at receiver end |
| $P_{FA}$ | Probability of false alarm |
| $P_D$ | Probability of detection |
| $\tilde{P}(\cdot)$ | Priori covariance for Kalman filter's prediction |

| | |
|---|---|
| $\bar{\varphi}$ | Average phase misalignment during one coherent interval |
| $\Phi(\cdot)$ | Transition matrix of system dynamic model |
| $Q_{v,k}$ | Quadra-phase output from $v$ correlator |
| $\bar{Q}_{v,k}^{m}$ | Quadra-phase output from $v$ correlator normalized by $m$ |
| $Q(\cdot)$ | Right tail of the unit-variance Gaussian distribution |
| $R_{GM}$ | Reciprocal of the time constant for a Gauss-Markov process |
| $\tilde{R}(t)$ | Filtered waveform of PRN autocorrelation function |
| $r(t)$ | Waveform of received GPS signal |
| $S_4$ | Intensity indicator of amplitude scintillation |
| $S_v(f)$ | Power spectrum density of $v$ |
| $\sigma_{\delta\theta^{Scint}}$ | Intensity indicator of phase scintillation |
| $\sigma_v$ | Standard deviation for measurement of $v$ |
| $T_b$ | Data bit period |
| $T_c$ | Spreading code chip duration |
| $T_{COH}$ | Coherent integration time |
| $T_d$ | Total signal transmission delay |
| $T_{sys}$ | System noise temperature |
| $T(\cdot)$ | Test statitic for signal detection |
| $\theta(t)$ | Carrier phase of received signal |
| $\hat{\theta}(t)$ | Local estimation of carrier phase |

| | |
|---|---|
| $Var(\cdot)$ | Statistical variance |
| $\tilde{x}$ | A Priori estimate of the system states |
| $\hat{x}$ | A Posteriori estimate of the system states |

# Chapter 1 Introduction

## 1.1 Background and Motivation

The Global Positioning System (GPS) has been established as a dominant positioning technology to provide location and navigation capabilities with a high reliability and accuracy, low cost, and portability.

Various emerging applications require location of users in challenging environments where typical GPS receivers suffer degraded performance or complete failure. The Enhanced 911 Mandate by Federal Communications Commission (FCC) is one of the most important indoor and new applications. It requires the wireless carrier to provide automatic location identification (ALI) of the emergency caller, based on which the public-safety answering point (PSAP) then dispatches the rescue team (Sugrue 2001). Solely cellular-based positioning has difficulties providing the level of accuracy required in a cost effective manner; therefore systems such as assisted GPS (AGPS) have recently been adopted to improve location-based services (LBS). Rising consumers' demands require the enhancement of stand-alone GPS to continuously offer positioning information in environments where the signal is greatly attenuated or severely corrupted by strong interference (Lachapelle 2005, Julien 2005). Typical interference in the context of the radio communication include signal masking, multipath, external radio frequency interference (RFI) and inter-satellite cross correlations (Lachapelle 2005, Ray 2005, Parkinson &

Spilker 1996). Attenuation and interference degrade the ability of GPS to acquire and track signals effectively. To extend and improve the availability, reliability and accuracy of GPS, innovative receiver algorithms for acquisition and tracking are required.

Klobuchar (1996) describes degradation of GPS performance in the presence of the ionospheric scintillation. Amplitude fading and rapid phase variations associated with strong ionospheric activity deteriorate signal tracking, or even worse lead to a loss of positioning and navigation capabilities. Augmentations to improve the sensitivity and robustness of signal tracking can extend the availability of GPS and benefit studies of the atmosphere's properties. By applying advanced estimation methods, the tracking reliability can be optimized in the presence of geomagnetic storms. By doing so, delay-locked loops (DLL) and phase-locked loops (PLL) can maintain continuous tracking of the incoming signals affected by scintillation; valid raw measurements are thus produced. By compiling and studying these measurements, the physical properties of scintillation at auroral latitudes can be identified and then modeled to mitigate measurement errors.

In terms of the availability, reliability and accuracy, the operation of GPS indoors or in urban canyons suffers from four limitations: (1) tracking of a multipath-affected signal degrades the accuracy (Watson 2005), (2) tracking failure occurs once the signal strength falls below a given threshold (Watson 2005), (3) frequency offsets and drift of the oscillator (OSC) driving the GPS receivers prevent the receiver from acquiring and tracking very weak signals (Lachapelle 2005, Kaplan 1996, Kaplan & Hegarty 2006), and (4)

cross-correlation interference from strong channels interrupts acquisition and tracking of the weak channels (Kohno et al 1983, Norman & Cahn 2005). To overcome these limitations, the space segment is being modernized and new receiver technologies are being developed (e.g., Watson 2005, Julien 2005, Lachapelle 2005, Cannon 2005). Both the satellite systems' modernization and the state-of-art receiver technologies will be briefly reviewed in the remainder of this section. For readers who are unfamiliar with GPS technology, a review of GPS fundamentals, the basics of GPS signal structures, and the principles of code division multiple access (CDMA) are provided in Appendix A. More comprehensive resources for GPS information include Parkinson & Spilker (1996), Kaplan (1996), and Hoffman-Wellenhof et al. (2001).

The GPS I, initialized in 1973 to reduce the proliferation of navigation aids, is the only satellite-based radionavigation system that is operated and maintained by the United States Department of Defense (DoD). Although navigation messages are simultaneously broadcast on several channels by GPS I, only one channel can be fully accessed by civil users. Special techniques, although making it possible to obtain measurements from the L2 encrypted channel, result in lower quality and availability of the measurements. In order to capitalize on the increasing demand from the civil market for more performance, several projects were launched to give birth to the second generation of Global Navigation Satellite Systems (GNSSs) in the 1990's (Kovach & Van Dyke 1997). This paragraph, plus the next two paragraphs, describes the main components of general GNSS modernization: 1. Augmentation systems 2. New satellite systems 3. GPS modernization. GPS modernization starts with the development of augmentation systems complementary

to GPS I (Misra & Enge 2001). These external systems provide additional information and thus reduce uncertainties in the final positioning or navigation solutions while improving availability and reliability. These systems are, however, essentially dedicated to specialized applications such as civil aviation or marine applications, and can be classified as satellite-based augmentation systems (SBAS), ground-based augmentation systems (GBAS) or airborne-based augmentation systems (ABAS). Well-known systems include the US wide area augmentation system (WAAS) (Enge & Van Dierendonck 1996), local area augmentation system (LAAS) (Misra & Enge 2001), and the European Geostationary Navigational Overlay Service (EGNOS) (Toran-Marti & Ventura-Traveset 2004). Although effective, they are very expensive to build and are often are dedicated to the authorized GNSS users. The overall performance is constrained by inherent factors limiting the capability of GPS I (Kovach & Van Dyke 1997).

The successful operation of GPS has allowed a variety of potential applications and resulted in a substantial growth of demands in positioning and timing applications (Onidi 2001); previous success has motivated the development of new systems and considerable efforts to modernize GPS I. In the 1990's, The US DoD and Department of Transportation (DoT) initiated the GPS modernization program with GPS II and GPS III (Kovach & van Dyke 1997, Kaplan & Hegarty 2006). The European Union (EU) and the European Space Agency (ESA) reached a unanimous agreement to launch the European Civil Satellite Navigation Program, Galileo (European Commission 1999; Onidi 2002). Recently, Russia has decided to enhance its GLONASS program (GPS World 2005).

Both the GPS II system and Galileo will broadcast wideband signals on three civil (open) frequencies (Lachapelle 2005) designed for frequency diversity and ionosphere estimation purposes. Once the Galileo and GPS II systems have been fully deployed, any GNSS user would be able to freely access six types of differently modulated signals in three frequency bands; therefore, users will be able to obtain more accurate and reliable positioning solutions. In addition, the modernized systems include new signal structures designed to reduce the main weaknesses of GPS I. Two deliberate modifications include the binary offset carrier (BOC) modulation and the presence of a dataless channel. Figure 1-1 shows the spectral density in the L1 frequency band for GPS and Galileo systems. The legacy C/A code signal uses the binary phase shift keying (BPSK) modulation. The modernized GPS II M code and the Galileo L1F code will employ the BOC modulation to separate them from the other signals (Betz 2002, Julien 2005). The dataless channel will greatly improve the sensitivity of acquisition and tracking (Lachapelle 2005). Betz (2002), Julien (2005), and Barker (2000) have determined that the BOC modulation outperforms in the corresponding GPS I BPSK modulation in terms of resistance to thermal noise, narrow-band interference rejection, and multipath mitigation.

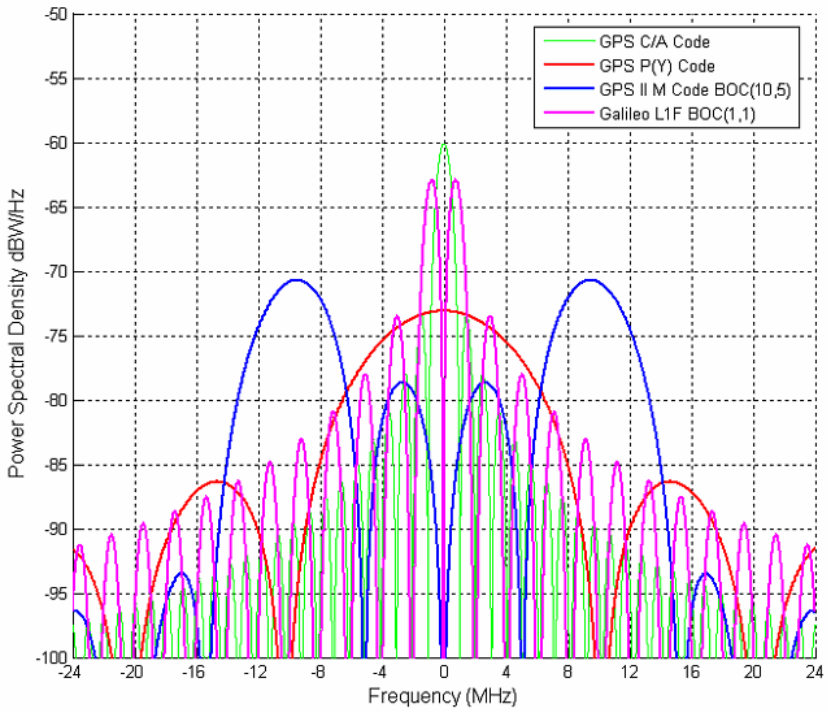


Figure 1-1: Power Spectral Density (PSD) of GPS I, GPS II, and Galileo L1F Signals

However there are still several years of implementation and development required for the modernized systems to become fully operational. Since 2002, the EU Galileo system has been in the development and validation phase. The constellation deployment phase will consist of gradually launching all the operational satellites into orbit and ensuring the full deployment of ground infrastructure necessary to offer an operational service from 2008-10 onwards. Assuming that the proposed schedule is followed, GPS II would be complete by approximately 2010. As a result, the current increasing user demands have resulted in much research to enhance receiver acquisition and tracking algorithms, and therefore extend positioning availability in the context of the existing conventional space infrastructure for GPS I (Cannon et al 2003).

Improving state-of-art receiver technologies is one of the most efficient ways to fully achieve the potential of GPS I. Not only is this approach cost effective and surpass the limitations of cellular LBS (Pomerantz 2002), it also contributes to the receiver technology necessary for the next generation GNSS. Economy, accuracy, and continuous availability are GPS advantages that users can access to help make the world a safer and more secure place in which to live (Pomerantz 2002). Since the late-20th century, the power of digital signal processors (DSP) has rapidly increased, allowing new developments in signal processing and advanced estimation theories (Psiaki 2001). Both foster continued development of the latest GPS receiver technologies, which aim to maximize the capabilities of GPS I with respect to accuracy, availability and reliability. Receiver innovations are focused on meeting the following challenges inherent to GPS.

(1) GPS is fundamentally a timing system, measuring the line-of-sight (LOS) radio propagation delays between satellites and a user to derive accurate ranges, and therefore positions. This contrasts with digital communication systems, which quantify the service quality by measuring the bit error rate (BER). In communication systems, the propagation path is unimportant if the desired bit-error-rate can be achieved (Watson 2005). However any deviation from the LOS path compromises the GPS position accuracy. The LOS signal propagation channel consists of free space and the Earth's atmosphere. Lachapelle (2005), Parkinson & Spilker (1996), and Cannon (2005) discuss modeling routines designed to mitigate the timing errors on LOS channels. More often than not,

non-line-of-sight (NLOS) propagation paths, known as multipaths, cause effects more significant on the timing error than on the BER (Watson 2005); therefore the multipath essentially decays the positioning accuracy while not necessarily compromising the receiver's capability in tracking and decoding the message (Watson 2005).

(2) ICD200C (2000) states that, for a receiver antenna with hemispherical gain pattern, the minimum received strength of the GPS signal under open-sky conditions is defined as -158.5 dBW for the L1 coarse/acquisition (C/A) code. This power is spread over a large bandwidth by the CDMA technique, leading to a peak PSD near -220 dBW/Hz, which is significantly lower than average ambient noise levels of about -208 to –204 dBW/Hz (Parkinson & Spilker, 1996; Ray, 2005). Thus, even under normal conditions, a significant processing gain is required to extract the signal from the noise. The signal levels decay rapidly in weak signal environments such as urban canyons or indoors. For signals propagating through a wall, the signal strength is generally 10 to 30 dB weaker than those signals received from the LOS directions (MacGougan et al 2002, Klukas et al 2004). In addition to the insertion loss, destructive interference through combination of several NLOS rays causes signal fading. Fading is particularly detrimental to GPS reception because signal levels vary rapidly and, even worse, drop deeply in some occasions; the variations are dependent on the characteristics of the environment (Watson 2005). In the presence of strong multipath, extremely deep fades can persist for seconds, minutes, or longer depending on the geometry.

(3) The ability of the data processing system to correctly recover the information carried by weak incoming signals relies on the OSC's frequency stability. To illustrate the GPS receiver as a specific case, the on-board/external OSC is the driver for the operation of every component in the receiver. This OSC provides the receiver's front-end (FE) with an oscillating reference (Ray 2005, Parkinson & Spilker 1996), based on which the frequency synthesizers establish all required timing standards for signal processing in both the radio frequency (RF) domain and the baseband domain. Ideally, the local OSCs (LOs) are expected to provide the pure spectrum signals. There should be no unwanted amplitude or frequency/phase modulation in the output spectrum (Stephens 2002). However the spectrum of output signals from real LOs is smeared by undesired phase noise (PHN) modulations (Hajimiri 1998). PHN sources in the circuit of the FE can be divided into two groups: device noise and interference. Thermal, shot, and flicker noise are examples of the former, while substrate and supply noise are in the latter group. In principle, these fluctuations can be classified into systematic (deterministic) and random variations. The systematic variations degrade receiver performance in acquiring and tracking very weak signals: as the processing intervals extend, the phase of the local carrier replica oscillating at the ideal frequency deviates from the phase of incoming signals (Zheng 2006). Once the phase misalignment exceeds a given threshold, the GPS receiver, a type in the family of coherent (COH) receivers, fails to acquire and track the signal. Fortunately, in healthy operation, the receiver can mitigate OSC-induced errors by estimating the deterministic

variations. Also, the deterministic fluctuations can be minimized by applying appropriate circuit techniques (Gierkink 1999) at the expense of the cost, size, power consumption, and complexity of the circuits. Random phase variations are caused by noise, produced in the active and passive components of the OSC circuit, which modulate the frequency of oscillation. These variations limit the achievable performance of GPS receivers in terms of measurement accuracy.

(4) The use of 1,023-chip Gold-codes for the GPS C/A PRN codes represents a compromise between the need for rapid acquisition and the cross-correlation dynamic range of the PRN codes (Norman & Cahn 2005, Glennon & Dempster 2004). Although these Gold codes generally work well, Gold codes have a significant difficulty in situations where weak signal detection is required in the presence of other strong GPS signals. If the power level difference between the weak and strong channels is sufficient, the cross-correlation peak for a strong signal can effectively jam other auto-correlation peaks resulting from the remaining weak signals (Norman & Cahn 2005). In the context of GPS, the cross-correlation interference depends on differences in the power levels and Doppler offsets between strong and weak signals. Assuming that the power difference is fixed, the maximum cross-correlation jamming occurs at the Doppler difference of ±M kHz, where M is an integer. A correlation pattern test can differentiate the autocorrelation from the cross-correlation (Zheng 2005).

Investigating the major above weaknesses and potential solutions for weak signal applications, constitutes the core of this thesis. Evaluating the limitations in conventional tracking and acquisition methods, and developing new methods to overcome limitations of sensitivity, reliability and accuracy, are the motivating factors.

## 1.2 Objectives

The aim of this thesis is to evaluate the performance of traditional GPS receivers in the presence of weak signals and other selected interference, and to propose new strategies for improved performance. This major objective includes the following research goals:

1. **To find a differential approach-based detector**, which reduces the squaring loss (SL) compared with the traditional noncoherent (NCH) detector. A smaller squaring loss necessarily represents an improvement in the sensitivity.
2. **To measure the stochastic stability of the oscillator and quantify the PHN induced by the receiver's front-end**. Stochastic differential equations (SDE) are employed to model the clock behavior modulated by random noise. The relationship between diffusion coefficients of the model and those stability measures is established. The phase fluctuation of the digital outputs from the front-end is measured by taking into account the major noise sources in the frequency synthesizers.
3. **To optimize the tracking capability of constant bandwidth PLLs (CBPLLs) in various types of interferences, and implement bandwith-variable PLLs**. This research examines the PLL behavior in the presence of the main error sources includ-

ing thermal noise, the phase noise, and the ionospheric scintillation. Nonlinear approach avoids the underestimation of the phase-error variance occurring at the region of low signal to noise ratio (SNR) (Viterbi 1966). Therefore, the optimal configurations improve tracking performance compared to the CBPLL. Advanced estimation and adaptive filtering are used to optimize the bandwidth of the PLL to minimize the phase-error variance induced by disturbances.

4. **To evaluate the oscillator stability and to test new algorithms using a simulator and a software receiver**. This consists of two sub-objectives: (1) to investigate the effects of PHN, characterized by Allan variance (AVAR), on the performance of the CBPLL, and (2) to confirm the results obtained theoretically in this thesis. Simulation tools are adopted to measure the phase error resulting from the OSC instability. Recent advances in computer processing make it possible to modify existing software packages, or to create new ones, in order to develop relevant and versatile simulation tools. The goal is to develop two complementary software tools:

   - **Development of a software OSC noise generator,** and
   - **Development of a set of software receiver tracking loops.**

The organization of the thesis is determined by the nature of these four research goals, and the tasks required to meet these goals, as described in Section 1.4.

## 1.3 Contributions

The major contributions of this thesis are given as follows:

- Development of a differential approach-based detector, namely differential combining (DFC) based detector, with SL that turns out to be 2.5 dB lower than that of the NCH detectors.
- Propose a general linearized model for Costas loops, which accounts for the nonlinearity of the discriminator by examining the response of the discriminator in the presence of disturbances.
- Capability to model the OSC's PHN in the digital samples.
- Development and implementation of an adaptive carrier tracking algorithm, which minimizes the phase tracking errors induced by noise and ionospheric scintillation.

Above advances extend the potential of the receiver to acquire and track weak signals. They not only maximize the availability of the current GPS I system, but can be applied to future receivers designed for the next generation satellite systems.

## 1.4 Thesis Outline

This thesis consists of five chapters. Chapter 1 addresses the challenges for continuous signal tracking by GPS receivers in the context of GPS I. Advanced receiver technologies provide cost- and time- effective solutions to maximize the potential of GPS I and, additionally, effective implementation in receivers being developed for the forthcoming satellite systems. To meet these challenges, the thesis objectives and contributions are clarified and the outline of the thesis is provided.

Chapter 2 describes the software tools used throughout this thesis to test algorithms and techniques. The software GPS intermediate frequency (IF) generator is reviewed; then a survey of the acquisition and tracking strategies in the software GPS receiver is provided. The following section describes the measures to quantify the instability of OSCs, based on which the model for simulating the OSC-induced PHN is developed. Finally, the ionospheric scintillation model, used in Chapter 4 to evaluate its impact on receiver's tracking behavior, is presented.

Chapter 3 presents a DFC-based detector that improves the acquisition sensitivity. The performance of this detector is evaluated in statistical sense.

Chapter 4 investigates the tracking behavior of CBPLLs and bandwidth-variable PLLs in the presence of perturbations. The critical parameters that affect the behavior of a CBPLL are investigated based on a statistical examination in the presence of perturbations. Section 4.1 examines the CBPLL with four types of discriminators and three configurations of loop filters. The performances of all these CBPLLs are investigated under disturbance of thermal noise, PHN and ionospheric scintillation. Beyond examination of CBPLLs, a Kalman filter-based PLL is described to enhance the tracking capability. Its tracking behavior is examined under the same conditions as those for CBPLLs. The results are used to quantify the sensitivity and accuracy improvements.

Finally Chapter 5 emphasizes the main conclusions of this thesis and presents the recommendations for future work.

# Chapter 2 Simulation Tools

Simulation tools provide an effective way to evaluate the tracking performance in a controlled environment. The impact of some irregular phenomenon such as ionospheric scintillation on the GPS receiver's tracking capability can be examined using an existing scintillation model, as described in Section 2.5. Besides these, specific interferences can be separated from others, and therefore their impact on the tracking performance can be quantified. This performance evalution provides a useful insight in tracking optimization and enhancement mechanisms.

## 2.1 IF GPS Signal Generator

Global Navigation Satellite System (GNSS) receiver development and optimization is a complex task. Control over a repeatable test environment essentially enables meaningful GNSS research and development. Such capabilities are offered by a GNSS signal simulator with high accuracy. A GNSS signal simulator

(1) extensively reduces the demand to perform field trials that are always limited by the incontrollable elements imposed by real-world testing, therefore exhibiting ultimate flexibility and significantly shortening development cycles.

(2) evaluates navigation capability of a GNSS receiver in the presence of selectable disturbances. To acquire and tightly track the signal is critical to maintain the navigation capability. However, both units (acquisition and tracking) exhibit se-

vere performance degradation when operating at the threshold region or experience a malfunction. This failure results in a loss of navigation capability. A deep understanding of the units' behaviour in the presence of perturbations provides insight necessary for determining methods required to enhance immunity to the interferences, therefore extending the availability of the navigation solution.

(3) examines the achievable performance for different processing strategies in a repeatable and controllable context. A controllable environment provides the ability to compare various approaches under exactly identical conditions, and to distinguish effect of one interference from another. These interference effects are usually coupled and indistinguishable from each other in the real world.

(4) validates the theoretical results in practice.

In the context of this thesis, both hardware and software simulators are used to validate theoretical results, and are used to quantify the improvement resulting from advanced signal processing and estimation techniques. Using SimGEN$^{TM}$ with the Spirent 7700 hardware simulator provides the user flexibility in configuring the following errors and interferences as needed: satellite errors, atmospheric signal degradation, obscurations, multipath and antenna characteristics. It does not however provide users at this time with a platform to create new scenarios such as the occurrence of ionospheric scintillation, and cannot separate errors that are naturally stemming from the limitations of the hardware simulator components.

A software simulator however provides enough flexibility to characterize the conditions that occur irregularly in the natural world, and thus to assess the receiver's operation under those situations. The user can configure the GPS signal propagation and processing chain, allowing the introduction of specialized situations to create digitized IF GPS signals with specific properties as required. This makes it convenient to test and evaluate various acquisition and tracking algorithms and to investigate the navigation capability of a receiver in the presence of specific interference conditions. A software simulator also makes it possible to separate the ambient noise from other disturbances at the FE, such as OSC-induced fractional phase jitter. This jitter creates a tracking error that is unidentifiable under nominal SNR conditions (Kaplan 1996, Yu 2006a). Fortunately, the software simulator is able to decouple disturbance of OSC from ambient noise; therefore, this separation provides a way to validate the rule-of-thumb quantifications presented by Kaplan (1996, 2006) and Raquet (2006).

### 2.1.1 Summary of GPS IF Signal Simulator

Dong (2003) describes the development and verification of a basic digitized IF GPS signal simulator. This software simulator may be used for leading-edge research into various acquisition, tracking and navigation algorithms for receivers; The software simulator

(1) provides a basic user-friendly interface to flexibly manipulate the error sources that are coupled with the signal component at the receiver end, and thus can be

used to investigate the performance degradation of the receiver resulting from various combinations of interference conditions and thus

(2) forms a critical component of the objective to develop a series of generic GNSS software modules to quantify the effect of various types of interference and external aiding on system performance, and to enhance the receiver's navigation capability by optimizing the acquisition and tracking configurations or by applying new signal processing techniques to build the receiver.

The overall structure of this IF GPS simulator is summarized in Figure 2-1. The GPS constellation is loaded using a broadcast ephemeris file that can be downloaded, for example, from the *Crustal Dynamics Data Information System* website. This knowledge forms the basis for the true satellites' trajectory during the simulation interval. In addition, the satellite constellation can be derived from the above ephemeris. The resultant position, combined with the receiver's location, allows rejection of the satellites situated below the horizon, or under a specific mask elevation.

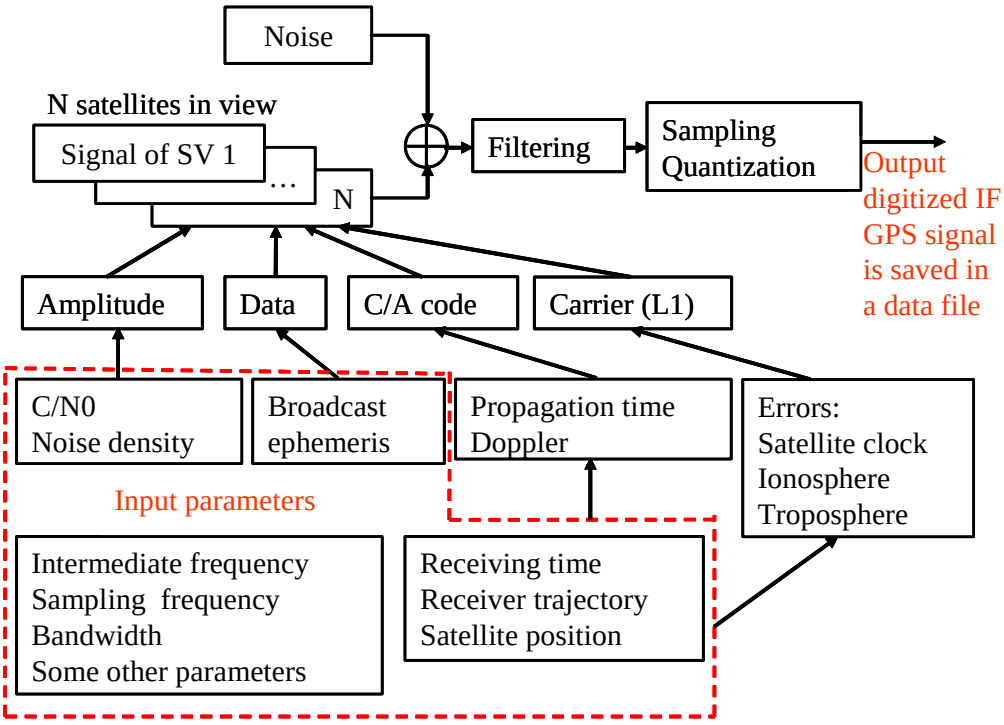


Figure 2-1: IF GPS simulator structure (Dong 2003)

Once the satellites in view and their trajectory are determined, the signal coming from each satellite has to be modeled at the receiver end. The model used in the GPS IF signal generator takes the following form:

$$r_{IF}(t) = \sqrt{2P_{C/A}}\, d\left(t - T_d - \delta t_{Iono}^{L1}\right)\tilde{c}\left(t - T_d - \delta t_{Iono}^{L1}\right) \times \cos\left(2\pi f_{IF} t - 2\pi f_{L1}\left(T_d - \delta t_{Iono}^{L1}\right) + \theta_0\right) + n(t) + MP(t) \tag{2.1}$$

with

$$T_d = \delta t_{Sat} + \delta t_{Eph} + \delta t_{Tropo} + t_p \tag{2.2}$$

where

$P_{C/A}$ denotes the received power of L1 C/A code waveform

$d(\cdot)$ is the waveform of the navigation message,

$\tilde{c}(\cdot)$ is the filtered waveform of the PRN serial for a satellite,

$f_{IF}$ is the IF frequency,

$\delta t_{Iono}^{L1}$ is the delay due to the ionosphere on the L1 frequency,

$\theta_0$ is the initial phase,

$n(t)$ is additive ambient noise assumed with Gaussian distribution,

$MP$ represents reflected rays due to multipath effects,

$\delta t_{Sat}$ models the satellite on-board clock error,

$\delta t_{Eph}$ is the satellite orbit error resulting from errors in the ephemeris,

$\delta t_{Tropo}$ is the delay due to the troposphere,

$t_p$ is the free-space propagation delay.

This model accounts for the errors resulting from the signal propagation and from the errors in satellites' clocks and orbits. The characteristics of these errors provides the required information to model their behaviour and to evaluate their effects on the receiver's acquisition and tracking performance, as intended in this research.

### 2.1.2 Error Sources for GPS Signal Propagation

This section describes the errors induced during signal propagation. Based on the characteristics of these errors, their impacts on the tracking performance are described. Dong (2003) proposes error models for satellite clocks, ephemeris, the ionosphere and troposphere, and the ambinent noise. The simulator does not however provide the simulation of atmospheric errors, namely the troposphere and ionosphere. The present research enables the simulation of receiver's PHN and of the ionospheric scintillation. The models for simulating these two perturbations conclude this chapter.

*Satellite clock and ephemeris errors*

Ephemeris errors result from a difference between the actual trajectory of the on-orbit satellite and the predicted version of position broadcast through the navigation message. This prediction is calculated from previous satellites' constellation and knowledge of Earth's gravity field (Julien 2005). The ground station uploads this forecast to GPS satellites at most three times per day, i.e. every prediction is valid for at least eight hours.

Since this error varies slowly with time, it can be regarded as a constant bias over the update interval of a tracking loop. The receiver's tracking loop, with respect to different loop orders, is designed to measure variation of the phase, Doppler, or the Doppler drift; therefore the deficiency of this prediction doesn't alter the tracking performance once the loop is already in tight lock. Olynik (2003) demonstrated satellite orbital errors have a temporal correlation greater than 90% over the interval of five minutes. This means that the tracking error resulting from orbit variation can be neglected.

A GPS receiver computes the user's position by measuring the ranges between the receiver and at least four satellites, and by employing the a priori knowledge of satellites'

position inherited in the navigation message; the satellites clock errors contribute to pseudorange errors (Lachapelle 2005, Cannon 2005). The final position error is a function of range inaccuracy multiplied by a factor termed dilution of precision (DOP). The small timing misalignment by the satellites oscillators can cause an unacceptable error due to the high speed of EM waves. To mitigate this effect, the GPS control system is able to predict the on-board clock behaviour that is modeled by a second-order polynomial (Kaplan 1996, Lachapelle 2005). Such information is included in the data package for transmission, and thus can be obtained by the receiver.

*Ionosphere*

Due to the free electrons in the ionosphere, GPS signals don't propagate in a vacuum and signal velocities are altered as the signal travels through this region, about 50 to 1500 km above the surface of the earth. The resulting effect is a range error. The ionosphere causes an effect equal in magnitude and opposite in sign on the code and carrier phase components of the signal. It delays the code by an amount proportional to the total number of the free electrons encountered and inversely proportional to the carrier frequency squared. The carrier phase is advanced by the identical amount due to this effect.

The Doppler shift at L1 from the ionospheric delay in normal case is approximately 0.085 Hz (Parkinson & Spilker 1996); thus the 3$^{rd}$-order carrier tracking loop is not sensitive to this small change. The carrier-code divergence prohibits setting a too narrow DLL bandwidth. In this case, the DLL is not able to track the divergence.

Typically, the ionospheric effect results in a ranging error of about 2-7 m for a satellite at zenith (Lachapelle 2005). It causes a larger error for low-elevation satellites because the

slant path through the ionosphere is longer. This measurement inaccuracy can be usually mitigated in three ways:

(1) Acquire the latest corrections from the received navigation message. This information is the applied in the form of a diurnal model to produce the corrections for the measured pseudoranges (Lachapelle 2005).

(2) The L band signals, with different carrier frequency, travel through this region at different speeds thus resulting in a discrepancy in code delay or carrier advance (Misra & Enge 2001). Therefore the dual-frequency receiver can eliminate this error by measuring the signal at both frequencies.

(3) The differential approach is able to reduce the error by utilizing the spatial correlation of number of free electrons over the baseline, typically within 10 km (Petrovski et al. 2002).

Activity of the ionosphere varies periodically over a day and over the 11-year solar cycle. The maximum diurnal value occurs at 14:00, and the last solar cycle peak occured in the middle of year 2000 (Lachapelle 2005, Cannon 2005). During solar maximum, the effects of ionospheric scintillation induce deep power fades and rapid phase variation. These high dynamics due to the ionosphere significantly impact GPS operation in susceptible areas: (1) the high latitude regions, such as Canada, where scintillations effects are dominated by phase variations associated with the auroral effects (Skone et al. 2005), and (2) the equatorial region, such as Brazil, where the power fades — not the phase fluctuation — are the dominant component in the presence of scintillations (Doherty et al. 2000). This creates a particular concern for investigation of the ionospheric characteristics by

interpreting the observations delivered from a receiver. Nevertheless, the strong scintillations may jeopardize the receiver's carrier tracking performance, and cause failure of the carrier tracking operation. The optimizations and advances in development of carrier tracking approaches, as described in this thesis, enable better receiver tracking performance in the presence of scintillations. Since current ionospheric effects are low due to solar minimum, it was not possible to collect real scintillation data. In order to evaluate improvements through development of optimized and advanced tracking strategies under scintillation occurrence, models of scintillation phenomena are implemented as an effective way to derive representative results. The detailed description of this phenomenon and a scintillation model will be described in Section 2.5.

*Troposphere*

The troposphere extends from the Earth's surface to altitudes of 70 km and the region below 10 km altitude includes most of the water vapour. Variations in pressure, humidity, and temperature jointly contribute to variations in radio transit speed. Unlike the ionosphere, the troposphere is non-dispersive for L band frequencies. It induces the same delay on both signal code and phase. Troposphere typically induces an error of 2.5 m for zenith observations, and this can increase to 9 m for a satellite elevation angle of 15 degrees (Misra & Enge 2001). Simple models can usually estimate the tropospheric error to within 20 centimetres (Cannon 2005). Olynik (2003) shows that temporal correlation for tropospheric effects is higher than that for the ionospheric delay (90% over 10 minute). Apart from tropospheric scintillation, this delay on the signal propagation does not affect the behaviour of the tracking loops.

*Multipath*

Multipath is one of the major sources of error in GNSS signal tracking. In real situations, the received signal comprises a direct ray and several reflections. Each reflection is a delayed version of the direct signal, and can be classified as either diffuse or specular. Large smooth surfaces result in a specular multipath that satisfies Snell's law. The power attenuation of such multipath, with respect to the direct signal, is small. Diffuse multipath originates from rough surfaces that scatter the direct ray. It usually results in unstable multipath with a large power loss (Ray 2005). In general, a triplet (amplitude attenuation, time delay, and phase delay) can approximately model each channel through which a reflection travels. The presence of multipath causes inaccuracies in estimating code delay by distorting the autocorrelation shapes as the dot curves presented in Figure 2-2. The solid line in this figure illustrates the autocorrelation function $\tilde{R}_{LOS}$ for the direct ray. The multipath, at the same time, yields a delayed and attenuated version $\tilde{R}_{MP}$ with respect to $\tilde{R}_{LOS}$. The constructive multipath (the red and blue) produces a positive correlation between $\tilde{R}_{MP}$ and $\tilde{R}_{LOS}$, leading to an over-measure of the range. However the destructive multipath yields a negative correlation, resulting in an underestimation of the range.

The maximum phase error due to multipath is $1/4$ cycle (Lachapelle 2005). Figure 2-3 quantifies the phase tracking error caused by multipath interference, where the delay of the reflection ranges from 0 to 1 chip and the signal-to-multipath ratio is 6 dB. The attenuated sinusoidal pattern characterizes the phase tracking error, and the envelope is depicted by the blue lines. Thus far, research efforts have been focused on multipath impact

on pseudorange measurements. Few methods, such as the multi-antenna system by Ray (2000), Strobe & Enhanced correlator in Ray (2005) and Vision correlator by Fenton & Jones (2005), are effective to reduce multipath impact on carrier phase estimation.

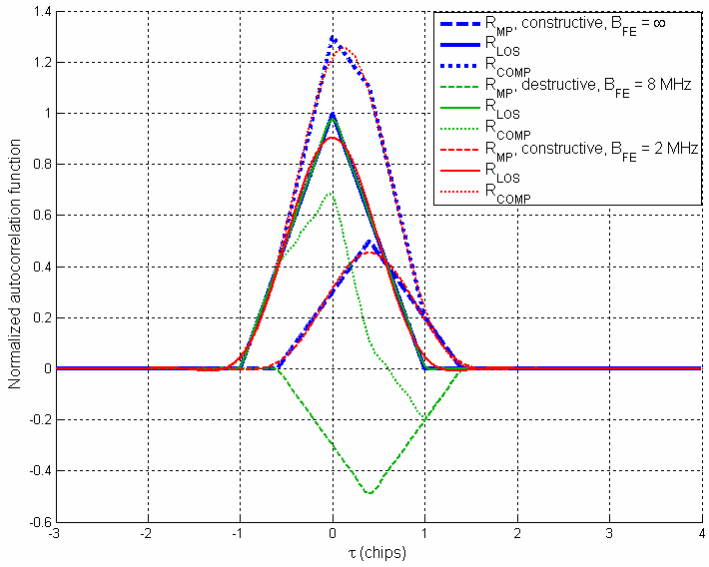


Figure 2-2: Multipath impact on code autocorrelation function

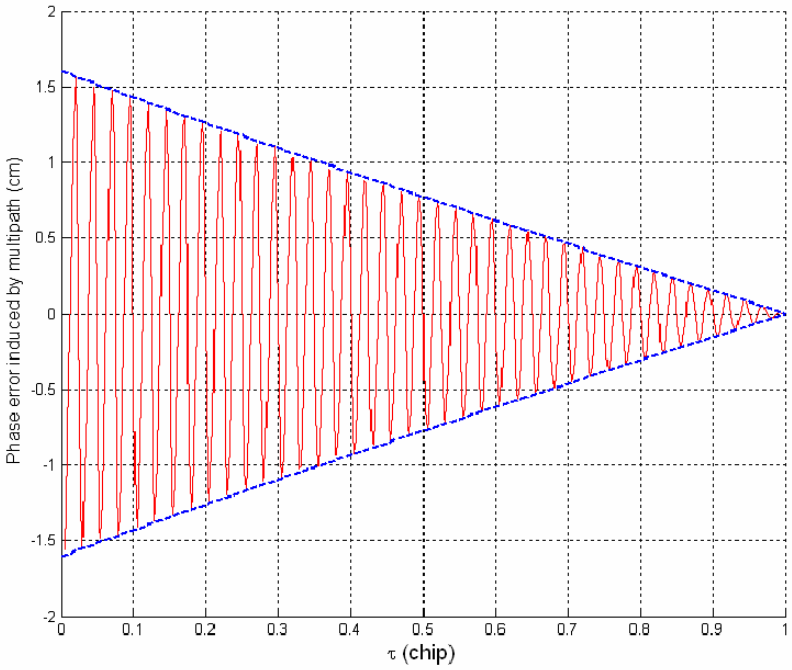


Figure 2-3: Multipath impact on phase tracking error

*Ambient noise*

Thermal noise corresponds to the ambient noise present at the receiver antenna level. It is assumed to be white and Gaussian with a PSD equal to:

$$N_0 = K_B T_{sys} \tag{2.3}$$

where $K_B$ is the Boltzman constant (= -228.6 dBW/K/Hz), and

$T_{sys}$ is the system noise temperature, dependent upon the FE architecture (filters and low noise amplifiers (LNA)), and defined through Friis formula (Raquet 2006, Ray 2005).

For a typical receiver, it is common to assume that $N_0 = -205$ dBW/Hz.

*Receiver oscillator frequency noise*

The operation of the OSC behaves in both a deterministic and random manner (Allan 1987, Zucca & Tavella 2005). The deterministic variation stems from the internal changes in the OSC and is predictable. A second-order polynomial is used predict this behaviour similar to the method for the more stable satellite clocks. The random part, however, exhibits a time-varying property that is usually quantified using statistical considerations. This part critically influences the receiver's performance, particularly for operation under harsh SNR conditions, and is not accounted for by Dong (2003). This instability, termed PHN, in the OSC is divided into "internal" and "external" components. The former reveals system-inherent flaws and is modeled by a combination of several stochastic processes. The "external" PHN is induced by the crystal vibration and becomes apparent in dynamic applications. The model in Zucca & Tavella (2005) doesn't account for the $1/f$ noise, flicker frequency fluctuation. Davis (2005) reviews the approaches in simulating $1/f$ noise, but does not express the model in discrete form suitable for numerical simulation. Based on the aforementioned work, a comprehensive OSC's discrete model is discussed in detail and validated later in this chapter.

### 2.1.3 Implementation Loss of FE

It is worth noting here that $\tilde{c}(\cdot)$ in eq. (2.1) represents the filtered version of the C/A waveform of $c(\cdot)$ due to the band limit of receivers' FE. The precorrelation filtering is essential to prevent aliasing at the sampling stage in a digital receiver. This filtering, however, results in a correlation loss, and the round-off autocorrelation discontinuity, like the solid red curves as opposed to the solid blue curves in Figure 2-2. The filter is char-

acterized by a response with a sharp cutoff, linear phase shift, and a unit gain within the bandpass. The correlation loss, originating from the elimination of the sidelobes of the C/A code spectrum, is shown in Figure 2-4. The plot shows the correlation degradation versus the ratio of the filter's single-sided bandwidth $B_{FE}$ to PRN code chipping rate. This figure includes two cases: in the presence of wideband interference, the filtering band-limits the noise, reducing the effective correlation loss; while the energy of the narrowband noise is concentrated inside bandpass, where the filtering carries the loss of signal sidelobes without altering the noise power.

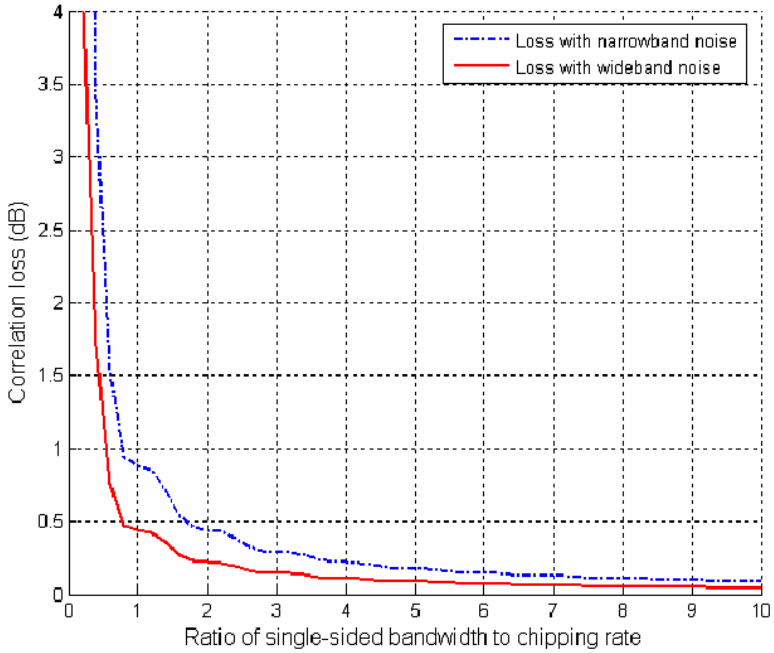


Figure 2-4: Precorrelation filtering loss (after Parkinson & Spilker 1996)

The filtered signal plus noise in eq. (2.1) is sampled and quantized by the analog to digital converter (ADC). The sampling rate, $f_s$, is selected to satisfy the Nyquist criterion (Ziemer & Tranter 2002) for the input signal, i.e. $f_s$ is twice the two-sided band-

width for the IF signal or is twice the single-sided bandwidth for the baseband signal. Using such sampling strategies, the noise samples are uncorrelated with a constant PSD within the sampling bandwidth. The quantization causes a degradation arising from the residual in approximating the analog measurement by a set of limited digital values. The degradation, termed quantization loss, is associated with quantization bits and bandwidth of the precorrelation filtering. An n-bit quantization determines $2^n - 1$ threshold levels; the quantization deviation decreases once more bits are employed. As per Chang (1982), Figure 2-5 and Figure 2-6 extend the results of Parkinson and Spilker (1996) by accommodating the degradation arising from an over 5-bit quantization scheme, where $T_c$ is the PRN code chip duration. The quantization is illustrated as a function of the ratio of the largest threshold $L_Q$ to the root mean square (RMS) of noise level.

Figure 2-5 presents the case close to the operation of a MAGR receiver for P code processing (Parkinson & Spilker 1996), where the single-sided bandwidth equals the code chipping rate. The configuration of threshold levels necessarily determines the performance of a quantizer. An inappropriate $L_Q$ reduces the potential brought by using more quantization bits, making the multi-bit quantizer asymptotic to the performance of 1-bit quantization diagram. The degradation presented here includes the precorrelation filtering loss of 0.45 dB shown as the blue curve in Figure 2-4. For a low-cost commercial receiver employing a narrow bandwidth with 1-bit quantization, the implementation loss in FE is nearly 3.5 dB.

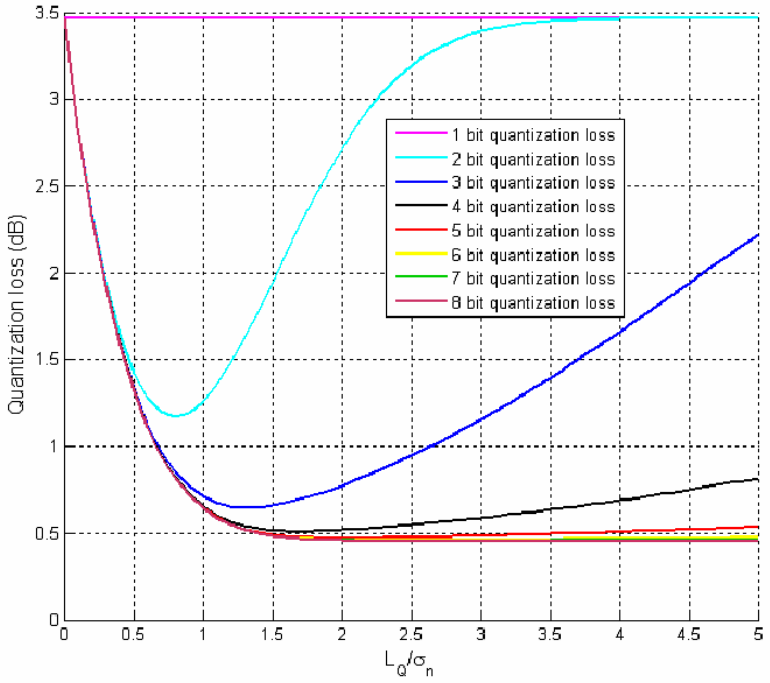


Figure 2-5: Quantization loss for narrowband $(1/T_c)$ filtering

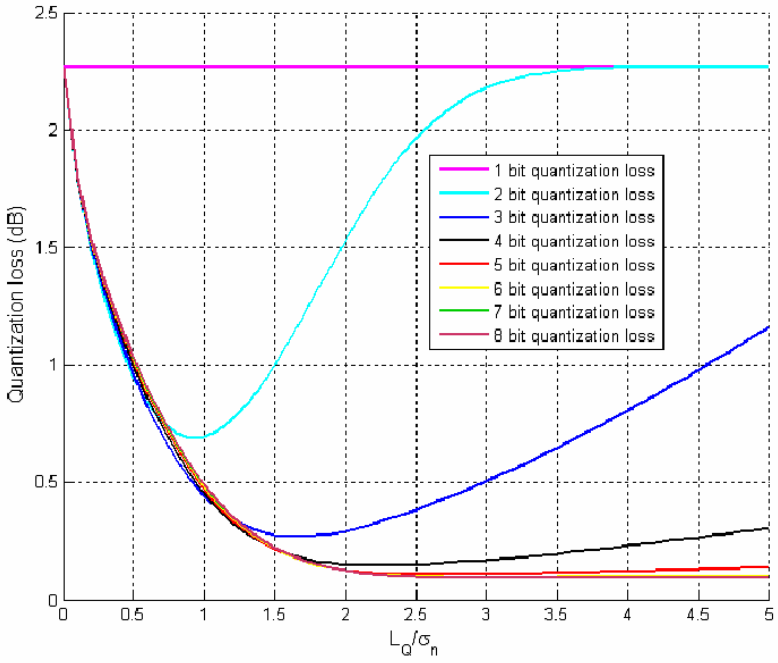


Figure 2-6: Quantization loss for wideband $(5/T_c)$ filtering

Figure 2-6 illustrates a sample of wideband precorrelation filtering, where the bandwidth is five times the code chipping rate, close to that of the GPSCard$^{TM}$ for C/A code processing (Parkinson & Spilker 1996). The minimum loss is achieved approximately at $L_Q/\sigma_n = 1$ for 2-bit quantization and $L_Q/\sigma_n = 1.5$ for a 3-8 bit system. Both figures demonstrate that the improvement appears indistinct by using 5-bit quantization as opposed to the adoption of an over 5-bit scheme.

## 2.2 IF GPS Software Receiver Review

The review of the software receiver accomplishes three purposes: (1) to coherently provide the signal processing flowchart in a GPS receiver; (2) to introduce the basic equations that will be used in subsequent chapters to assess the acquisition and tracking performance; (3) to examine the squaring loss and discriminators of DLLs using statistical consideration. The generic architecture of a GPS receiver is illustrated in Figure 2-7. As mentioned above, if the software signal generator is used, the FE unit has been simulated to create IF signal sequences. Consequently, the digital sequence from the IF signal simulator can be recognized by modules of the software receiver directly, without any requirement for pre-processing of the data. As the hardware simulator transmits the RF signal in analog form, the hardware FE is necessary to downconvert, filter, and digitize the received waveform.

The discrete samples are then fed into the signal processing units of a GPS receiver. These time series include the information for all the visible satellites. The acquisition

component in the receiver roughly estimates the code delay and Doppler shift of each satellite through a global or local search. The resulting information is used by a bank of signal tracking components to track the signal variations for each satellite simultaneously. Each of these tracking blocks is composed of two or three tracking loops: the DLL that tracks the spreading code delay; the PLL that synchronizes the carrier phase, and/or the frequency-locked loop (FLL) that tracks the signal Doppler. The carrier phase is a measure of the accumulated Doppler.

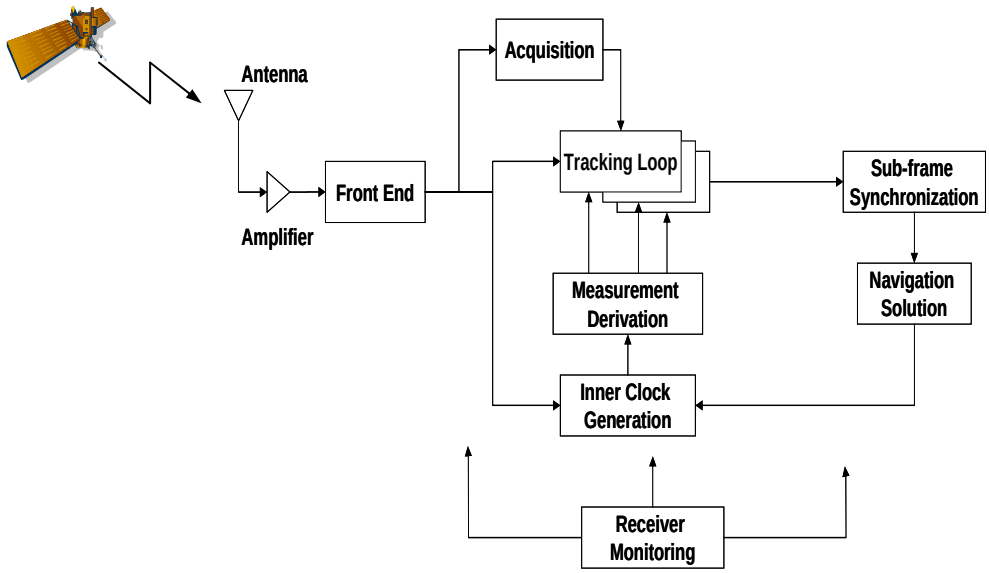


Figure 2-7: Generic diagram of a GPS receiver

Carrier and code synchronization is necessary for a GPS receiver to operate properly. Since the errors of carrier phase measurements due to multipath and receivers' noise are at least one order less than those for code measurements, the phase tracking is essential for high-accuracy applications. The measurements determined from the tracking loops are provided to the navigation unit where the final position solution is estimated by using

both the navigation data message and the satellite-receiver range measurements. Least-squares or Kalman filtering (Liu 2003) are two major approaches to compute the navigation solution. It is critical to understand that the measurements are made with respect to the GPS reference time. Nevertheless, the measurements from the tracking loops are produced with respect to the local OSC's timing standard. Since this timing misalignment is common to all tracking channels, it is usually modeled as an unknown, in addition to the user's three coordinates, in the position solution algorithm.

In order not to interfere with existing communication systems, the received GPS signal power is set very low. The minimum specified received power, using a 3 dBiC antenna with right hand circular polarization (RHCP), is -158.5 dBW for satellites located near the zenith or horizon (Raquet 2006, Lachapelle 2005). The maximum power, -153 dBW, is attained for an elevation of 40 degrees (Raquet 2006). In addition to this characteristically low signal power, the high chipping rate PRN code spreads the signal power over a wide bandwidth, thus resulting in a signal PSD below the usual ambient noise PSD level, which can be approximated at about -205 dBW/Hz under normal conditions (Van Dierendonck 1996). Figure 2-8 clearly illustrates this relationship.

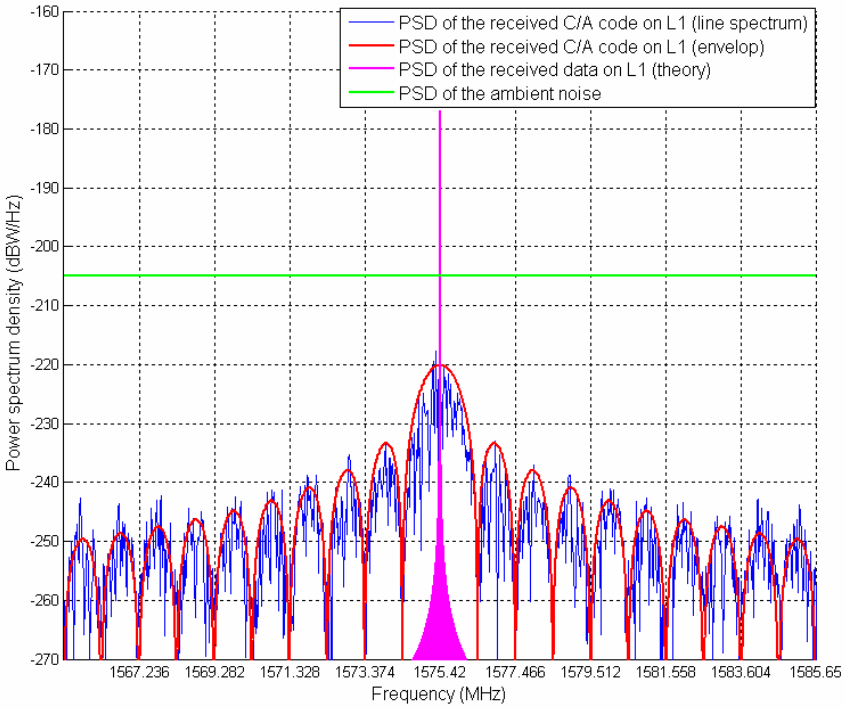


Figure 2-8: PSD of the L1 C/A code signal (actual and theoretical) vs. PSD of thermal noise at normal condition

Eq. (2.4) is the theoretical representation of the PSD envelope for the GPS C/A signal, where $f_c$ is the PRN code chipping rate (1.023 MHz for the C/A code) and $T_c$ (the reciprocal of $f_c$) is chip duration. The periodic PRN code creates discrete line serials in the spectrum domain, like the blue line in Figure 2-8, whose envelope satisfies the pattern of PSD of one chip (red line in Figure 2-8). Each line spectrum is separated by an increment equal to the ratio of the chip rate to the code length, or 1 kHz in the case of the GPS C/A signal. However, the envelope of the PSD is more often used for the analysis herein.

$$S_{C/A}(f) = P_{C/A} T_c \left( \frac{\sin\left(\pi f / f_c\right)}{\pi f / f_c} \right)^2 \tag{2.4}$$

Since the PSD of GPS C/A signals is overwhelmed by that of the noise, the GPS signal cannot be detected directly in L1 band, e.g. using classical tools such as an oscilloscope. This PSD level does not interfere with the terrestrial wireless communication and broadcast services.

In order to detect and track the GPS signal, the spread spectrum technique is used to redistribute signal power over the frequency spectrum. Assuming that the PRN code is perfectly estimated and removed from the received signal, the resultant PSD (magenta line in Figure 2-8) demonstrates that this recovery process concentrates signal power over a very narrow bandwidth, within which the signal power is much higher than that of noise power. This method allows detection and tracking of the GPS signal deeply suppressed by the noise. Based on this method, Figure 2-9 gives the functional diagram for the signal processing unit of a GPS receiver, where a numerically controlled OSC (NCO) is used to drive the digital loops. The DLL and carrier tracking loop are coupled with each other to make the receiver operate effectively. The received IF signal $r(t)$ (eq. (2.1)) can be simplified without accounting for the multipath interference as

$$r_{IF}(t) = \sqrt{2P_{C/A}}\, d(t-\tau_{C/A})\, c(t-\tau_{C/A}) \times \cos\left[\theta(t)\right] + n(t) \tag{2.5}$$

with a time-varying phase of

$$\theta(t) = \omega_{IF} t + \omega_d t + \delta\theta^{Osc}(t) + \delta\theta^{Scint}(t) \tag{2.6}$$

where

$\tau_{C/A}$ is the total signal propagation delay caused by all the errors mentioned previously,

$\omega_{IF}$ is the angular IF frequency, equal to $2\pi f_{IF}$ in eq. (2.1), and

$\omega_d$ is the angular Doppler frequency resulting from the LOS motion and propagation delay,

$\delta\theta^{Osc}(t)$ represents the receiver's OSC phase jitter, and

$\delta\theta^{Scint}(t)$ denotes the rapid phase variation in the occurrence of ionospheric scintillation, and finally

$n(t)$ is the band-limited ambient/thermal noise, with an expression of (Viterbi 1966)

$$n(t) = n_c(t)\cos\omega_{IF}t + n_s(t)\sin\omega_{IF}t \tag{2.7}$$

where $n_c(t)$ and $n_s(t)$ are white noise processes inside the bandwidth of $f_{IF}$ Hz.

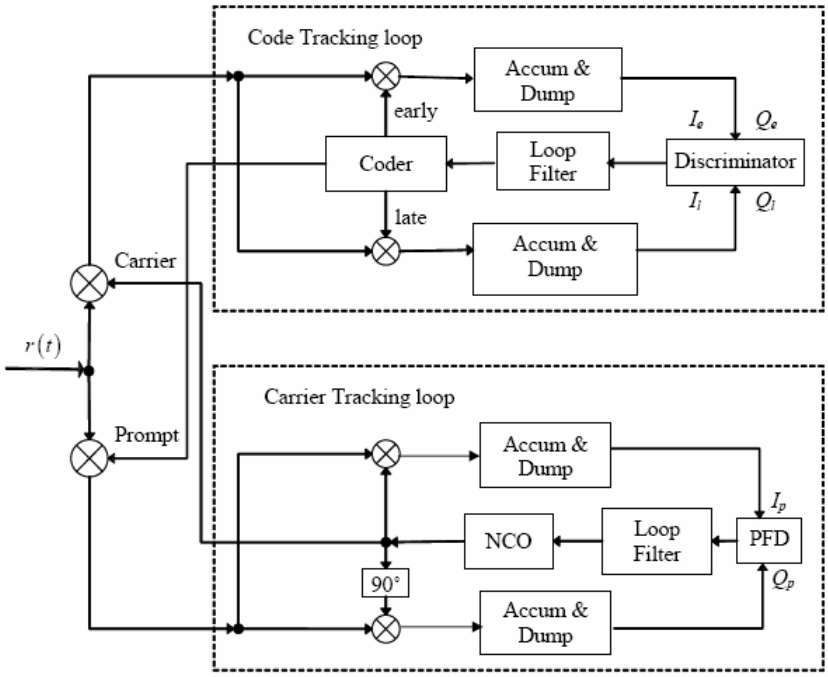


Figure 2-9: Functional diagram for signal processing unit of a GPS receiver

The received signal described by eq. (2.5) is split into two branches. One branch is multiplied by the in-phase local carrier, and the other one is multiplied by a quadrature-phase local carrier (shifted by 90°, as compared to the in-phase carrier replica). This processing wipes off the signal carrier and downconverts the signal to baseband. The power of the baseband signal is distributed over a rather wide one-sided bandwidth of 1.023 MHz for C/A code. Then it is correlated with the local code replica, and passed through the accumulation and dump (Accum & Dump) filter to achieve the COH units. This correlation, accumulation, and dump process is functionally identical to a digital matched filter (DMF) in communication terminology.

$$I_{v,k} = \sum_{j=j_k}^{j_k+N_k^{COH}-1} r_j \hat{c}_{v,j} \cos\hat{\theta}_j \tag{2.8}$$

$$Q_{v,k} = \sum_{j=j_k}^{j_k+N_k^{COH}-1} r_j \hat{c}_{v,j} \sin\hat{\theta}_j \tag{2.9}$$

Eqs. (2.8) and (2.9) describe processing by a DMF, where

$v$ could be early (*e*), prompt (*p*), and late (*l*) version of the locally-generated PRN samples,

$I$ is the COH unit at in-phase arm, and

$Q$ is the COH unit at quadrature-phase arm,

$r_j$ is the incoming signal sampled at $t_j$ w.r.t receiver's OSC,

$\hat{c}_{v,j}$ is the local code replica in $v$ version sampled at $t_j$, and

$\hat{\theta}_j$ is locally estimated carrier phase sampled at $t_j$,

$j_k$ is the start sample index for the *kth* COH accumulation, equal to $t_j / T_s$ where $T_s = 1/f_s$ is the sampling period,

$N_k^{COH}$ is number of samples per COH accumulation segment, equal to $T_{COH}/T_s$ where $T_{COH}$ represents the COH accumulation interval.

This pair of equations takes the analytical form of (after Parkinson & Spilker 1996)

$$I_{v,k} = \frac{N_k^{COH}\bar{A}_k d_{m,k}}{2} \frac{\sin\left(\pi\delta\bar{f}_k \cdot T_{COH}\right)}{\pi\delta\bar{f}_k \cdot T_{COH}} \tilde{R}_v\left(\tau_{e,k}\right)\cos\bar{\varphi}_k + n_{v,I,k} \tag{2.10}$$

$$Q_{v,k} = \frac{N_k^{COH}\bar{A}_k d_{m,k}}{2} \frac{\sin\left(\pi\delta\bar{f}_k \cdot T_{COH}\right)}{\pi\delta\bar{f}_k \cdot T_{COH}} \tilde{R}_v\left(\tau_{e,k}\right)\sin\bar{\varphi}_k + n_{v,Q,k} \tag{2.11}$$

where

$\bar{A}_k$ is the average signal amplitude over the correlation interval,

$d_{m,k}$ is the data bit, $\pm 1$, over the $kth$ correlation interval. $m = \lfloor t_j / T_b \rfloor$ indicates the index of the data bit, where $T_b$ is the data bit period of 20 ms, $\lfloor x \rfloor$ is the maximum integer number no greater than $x$ and $k = \lfloor t_j / T_{COH} \rfloor$ is the index of the COH accumulation interval,

$\delta \bar{f}_k$ denotes the average frequency misalignment between the incoming samples and the local carrier replica over the $kth$ correlation interval,

$\tilde{R}_v(\cdot)$ is the filtered normalized autocorrelation for the $v$ correlator, depicted by the solid lines in Figure 2-2,

$\tau_{e,k}$ is the average timing error over the correlation interval,

$\bar{\varphi}_k$ is the average phase misalignment over the $kth$ correlation interval,

$n_{v,I,k}$ denotes the additive noise at in-phase arm for the $v$ correlator, obeying the $N\left(0, \frac{N_k^{COH}\sigma_s^2}{2}\right)$ distribution, where $N(\circ, *)$ represents Gaussian distribution with expectation of $\circ$ and variance of $*$, $\sigma_s^2$ is the variance of the noise released from ADC, and

$n_{v,Q,k}$ is additive noise at quadrature-phase arm for the $v$ correlator, which shares the same distribution as $n_{v,I,k}$, and independent from $n_{v,I,k}$

This pair of equations is frequently used in this thesis to evaluate the sensitivity improvement obtained by using the new acquisition and carrier tracking algorithms.

$\tilde{R}_v\left(\tau_{e,k}\right)$ and $\dfrac{sin\left(\pi\delta\bar{f}_k \cdot T_{COH}\right)}{\pi\delta\bar{f}_k \cdot T_{COH}}$ (or $\sin c\left(\delta\bar{f}_k \cdot T_{COH}\right)$) each have a maximum amplitude of 1 when $\tau_{e,k}$ and $\delta\bar{f}_k$ take on the value of zero. If those values are non-zero, the result is a degradation in amplitude of the correlations. Code phase misalignment power degradation is calculated as $-20\log_{10}\tilde{R}_v\left(\tau_{e,k}\right)$. Given that the pull-in range of a code tracking loop is 0.5 chips, the code search step is set to one half chip, yielding a maximum code mismatch of 0.25 chips. The autocorrelation amplitude with 0.25 chips misalignment is approximately 0.75, resulting in a maximum 2.5 dB loss. Loss due to frequency mismatch is similarly calculated as $-20\log_{10}\left(\dfrac{sin\left(\pi\delta\bar{f}_k \cdot T_{COH}\right)}{\pi\delta\bar{f}_k \cdot T_{COH}}\right)$. If the frequency search bin size is selected as $1/2T_{COH}$, the maximum frequency offset of $\left(1/4T_{COH}\right)$ produces a 1 dB loss. The consolidated power degradation due to time-frequency uncertainty is 3.5 dB in the worst case given the above search space definitions.

### 2.2.1 Signal Acquisition

Using eqs. (2.10) and (2.11) and the acquisition fundamentals described in the literature, this section reviews the common acquisition approach and evaluates the decision variable (DV) using statistical consideration; the SNR of the DV determines the performance of signal acquisition.

The general architecture of acquisition units for GPS signals can be categorized as either software based, where time domain code phase ambiguity is tested in parallel on a DSP via a single Fast Fourier Transform (FFT), or hardware based, where multiple correlators are simultaneously dedicated to the hypothesis test in several dwells. The FFT method is described by Kaplan (1996), Lachapelle (2005), Psiaki (2001a), Ray (2005), and Raquet (2006); the reader can refer to these references for details. The multi-correlator strategy always utilizes all the correlation values (early, prompt, and late for a low-cost standard receiver) to speed up the code ambiguity search. For both types, an acquisition search progresses until a DV in one code/frequency bin is greater than a predefined threshold. This predefined detection threshold—a function of the noise floor and required detection statistics—in part determines the receiver's acquisition performance.

Extending the COH accumulation time is ideal for improving sensitivity, as it fully utilizes the potential of CDMA despreading gain $\left( T_{COH} \middle/ T_c \right)$. Such methods, however, are restricted by factors including data message ambiguity, increased power loss due to frequency errors, and a rapid increase in signal acquisition times. A 50 Hz navigation data message is modulated on the GPS coarse/acquisition (C/A) code via binary phase shift keying (BPSK). If COH integration periods include a data bit boundary, the possible phase reversal may negate the positive effects of extended integration. Even in the absence of data transitions, the extension of COH integration time proportionally reduces the tolerable frequency error due to the sinc pattern in eqs. (2.10) and (2.11), requiring

more accurate local frequencies to receive the signal with significant power. As a consequence, a denser grid of frequencies must be examined during acquisition, which increases total acquisition time by a factor of $N^2$, where $N$ is the ratio of extended integration time.

During the acquisition stage, the local carrier phase replica does not synchronize with that of the received samples, i.e. $\bar{\varphi}_k$ in eqs. (2.10) and (2.11) is indefinite; therefore, the signal power is unevenly distributed over the in-phase and quandrature-phase branches. To use either I correlation or Q correlation carries a risk of losing a significant portion of the signal energy. As a result, the I and Q functions are considered together in forming the DV, which is insensitive to the phase mismatch, for signal detection.

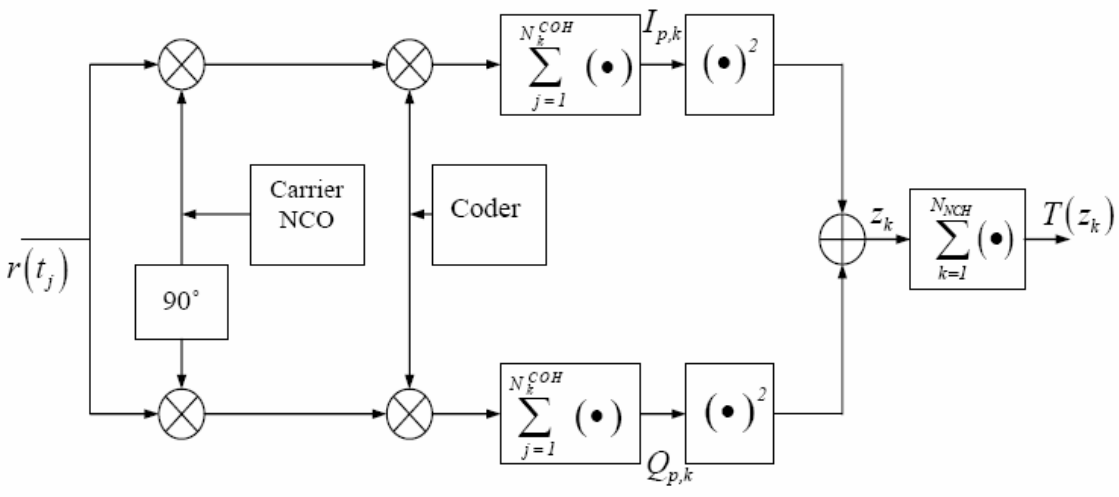


Figure 2-10: Functional diagram of the NCH power detector

Figure 2-10 displays the functional unit that is widely used in a GPS receiver to acquire the signal. The square of the resulting COH estimates are combined to form the unit DV

$$
\begin{aligned}
z_k &= I_{p,k}^2 + Q_{p,k}^2 \\
&= \left[ N_k^{COH} \tilde{A}_k \right]^2 + \\
&\quad \left\{ 2 N_k^{COH} \tilde{A}_k d_{m,k} \left( n_{p,I,k} \sin \bar{\varphi}_k + n_{p,Q,k} \cos \bar{\varphi}_k \right) + n_{p,I,k}^2 + n_{p,Q,k}^2 \right\}
\end{aligned} \tag{2.12}
$$

where

$\tilde{A}_k$ denotes the average amplitude over the correlation interval where the degradation due to the code and frequency misalignment has been accommodated, equal to $\frac{\bar{A}_k}{2} \frac{\sin\left(\pi \delta \bar{f}_k \cdot T_{COH}\right)}{\pi \delta \bar{f}_k \cdot T_{COH}} \tilde{R}_v \left(\tau_{e,k}\right)$.

The signal portion $[\cdot]$ is independent from the phase misalignment, i.e. the total signal power has been fully utilized for the detection, at the expense of amplifying the noise power. This power increase is evaluated by examining the statistics of the noise term $\{\cdot\}$ in eq. (2.12) which is denoted by $n_{z_k}$.

$$
E\left[ n_{z_k} \right] = N_k^{COH} \sigma_s^2 \tag{2.13}
$$

$$
Var\left[ n_{z_k} \right] = \left( N_k^{COH} \sigma_s^2 \right)^2 \left[ 1 + \frac{\left( N_k^{COH} \tilde{A}_k \right)^2}{2 N_k^{COH} \sigma_s^2} \right] \tag{2.14}
$$

Obviously, the squaring operation alters the noise statistics. The noise floor (expectation of the noise) expressed by eq. (2.13) increases compared with the zero-mean noise term in eqs. (2.10) and (2.11). Meanwhile, variance of the noise is increased as per eq. (2.14). The statistics of the DV are directly associated with SNR, a key index to determine capability of the acquisition algorithm; therefore, the investigation of this parameter provides insight into the influence of squaring operations on the detection performance. Since the SNR naturally results from the deflection coefficient, a terminology in signal detection

theory, the exact mathematical analysis of SNR degradation is given in Chapter 3. The basic conclusion is that the nonlinear operation, e.g. the squaring in eq. (2.12), uses the signal power at both I and Q branches effectively while reducing the SNR at the same time.

### 2.2.2 Signal Tracking

Acquisition produces a coarse estimate of the carrier Doppler and the code offset for each visible satellite. Due to the LOS motion between satellites and the receiver and phase jitter of the receiver's on-board OSC, among others, the carrier Doppler and the code delay vary over time. To maintain the timing and carrier synchronization, the signal tracking unit estimates variations in the carrier Doppler and code offset. After successfully obtaining the bit and subframe synchronization, precise pseudorange and carrier phase measurements can be derived from the tracking loops. At the same time, good tracking ensures correct demodulation of ephemeris which provides the satellites' trajectory information. Proper tracking requires the carrier freqeuency and code offset be matched by their local versions. Thus, the lock status of both the carrier tracking loop (FLL or PLL) and DLL are required to indicate the tracking status; they are coupled together as shown in Figure 2-9. The loss of one loop leads to the malfunction of the other loop. Compared with the DLL, the carrier tracking loop is the weaker link in the operation of a GPS receiver and thus more vulnerable to loss of lock. This behaviour of carrier tracking results from a wider bandwidth because (1) the same LOS motion leads to a larger carrier Doppler variation as opposed to the code timing thus requiring larger bandwidth to respond the dynamics, and (2) the DLL is usually aided by LOS motion estimate from the carrier tracking loop, and thus a relatively narrower bandwidth can guarantee that the DLL re-

sponds to the dynamic difference between the code and carrier (Raquet 2006).

Whatever carrier tracking or code tracking method is used, the loop is required to correctly measure the misalignment of code/carrier phase; the resultant correction is used to update the local replica. The discriminator, shown in Figure 2-9, is a key component in measuring the misalignments for both code and carrier tracking loops. This unit is also termed phase frequency detector (PFD) for the PLL and FLL (Stephens 2002). COH units are used by the discriminator to measure the local estimation mismatches. To improve the accuracy of the error estimates, the raw measurements output by the discriminator are fed into a low pass filter. This low pass filter is dedicated to extracting the actual misalignment while to maximum extent reducing the noise perturbations. Because behaviour and performance of the PLL will be comprehensively evaluated in Chapter 4, this section concentrates on the description of the FLL and DLL.

The frequency error is estimated by calculating the ratio of phase error variation to the time interval. To produce the frequency misalignment, the prompt correlations for current and previous epochs are used in following approaches (Kaplan 1996) that are listed in Table 2-1., in which $\overline{I}_{p,k}^{Sig}$ and $\overline{Q}_{p,k}^{Sig}$ are prompt correlations normalized according to the signal component in eqs. (2.10) and (2.11), i.e.

$$\overline{I}_{v,k}^{Sig} = cos\,\overline{\varphi}_k + \overline{n}_{v,I,k}^{Sig} \tag{2.15}$$

$$\overline{Q}_{v,k}^{Sig} = sin\,\overline{\varphi}_k + \overline{n}_{v,Q,k}^{Sig} \tag{2.16}$$

with

$$\bar{n}_{v,Ch,k}^{Sig}\Big|_{Ch=I/Q} = \frac{n_{v,Ch,k}}{\frac{N_k^{COH}\bar{A}_k d_{m,k}}{2}\frac{\sin\left(\pi\delta\bar{f}_k\cdot T_{COH}\right)}{\pi\delta\bar{f}_k\cdot T_{COH}}\tilde{R}_v\left(\tau_{e,k}\right)} \tag{2.17}$$

where the amplitude degradation due to errors in timing and frequency estimation can be disregarded by assuming a tight lock. This assumption results in

$$\bar{n}_{v,Ch,k}^{Sig}\Big|_{Ch=I/Q} \sim N\left(0,\frac{N_0}{2CT_{COH}}\right) \tag{2.18}$$

(Yu et al. 2006c), where $C/N_0$ is termed carrier to noise density ratio. Eqs. (2.15) and (2.16) illustrate the nonlinearity between the phase estimate error and the observations from the correlators. This nonlinear relationship demonstrates that the on-threshold behaviour of the FLL is far from the linear predictions. The multiplication in forming the *dot* and *cross* products amplifies the variance of the noise (Yu et al. 2006c); therefore the tracking result of the FLL is much noisier than that of the PLL.

Table 2-1: Discriminator algorithms for FLL

| FLL Discriminator | Frequency error | Commnents |
|---|---|---|
| $\frac{sign(dot)\cdot cross}{t_{j_k+N_k-1}-t_{j_k}}$<br>where<br>$dot=\bar{I}_{p,k}^{Sig}\cdot\bar{I}_{p,k-1}^{Sig}+\bar{Q}_{p,k}^{Sig}\cdot\bar{Q}_{p,k-1}^{Sig}$<br>$cross=\bar{I}_{p,k}^{Sig}\cdot\bar{Q}_{p,k-1}^{Sig}-\bar{Q}_{p,k}^{Sig}\cdot\bar{I}_{p,k-1}^{Sig}$ | $\frac{\sin\left(\bar{\varphi}_k-\bar{\varphi}_{k-1}\right)}{t_{j_k+N_k-1}-t_{j_k}}$ | Near optimal in tightly tracking. The $\sin(\cdot)$ characteristic produces the bias if the frequency error is large |
| $\frac{cross}{t_{j_k+N_k-1}-t_{j_k}}$ | $\frac{\left(d_{m,k}d_{m,k-1}\right)\sin\left(\bar{\varphi}_k-\bar{\varphi}_{k-1}\right)}{t_{j_k+N_k-1}-t_{j_k}}$ | Near optimal when the two accumulations are within a data bit period |

| | | |
|---|---|---|
| $\frac{ATAN2(cross, dot)}{t_{j_k+N_k-1} - t_{j_k}}$ | $\frac{\bar{\varphi}_k - \bar{\varphi}_{k-1}}{t_{j_k+N_k-1} - t_{j_k}}$ | Maximum likelihood estimator |

The code estimate error is derived from the early and late COH correlations. Under perfect code timing without noise disturbance, the early correlation is an image of the late one relative to the prompt correlation. Therefore, the difference between the early and late correlation reflects both magnitude and "direction" of the code phase mismatch, which is illustrated by Figure 2-11. In this case, we assume the code phase mismatch is 0.2 chips and that the correlator spacing is 1 chip. Obviously, the early and late correlations are not balanced once the code phase asynchronization occurs. A positive early minus late correlation drives the coder to advance the phase of the local code, while the negative difference controls the coder to lag the phase. The early minus late correlation analytically forms the function of the discriminator. The shape of the discriminator's response depends on the type of discriminators, the bandwidth of pre-correlation filter, and the SNR after coherent accumulation. Three types of discriminators are recommended for a GPS receiver (Kaplan 1996, Raquet 2005, Ray 2005): E-L envelope, E-L power, and dot product. The single-sided bandwidth considered here assumes baseband sampling.

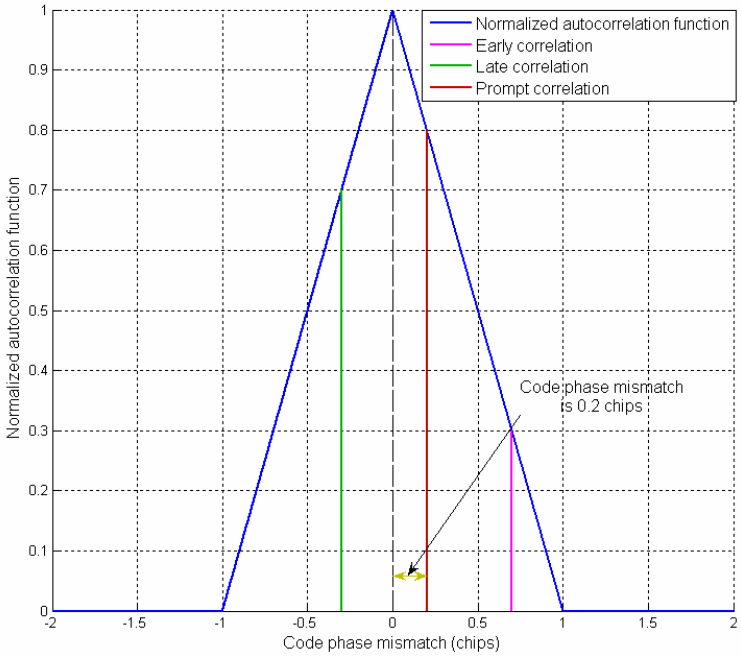


Figure 2-11: Code mismatch vs. early, prompt, and late correlations

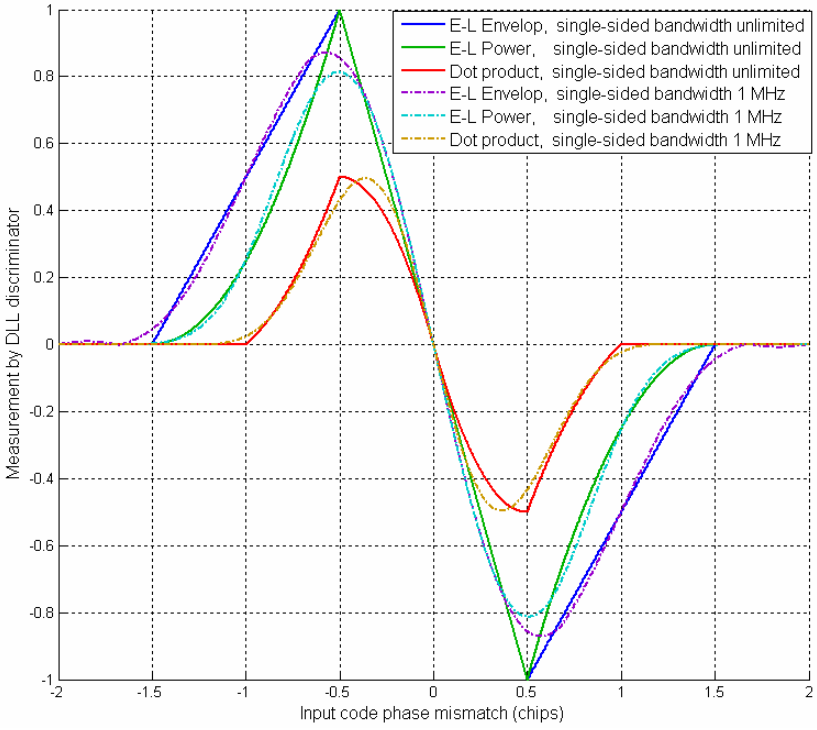


Figure 2-12: Response of three types of DLL's discriminators

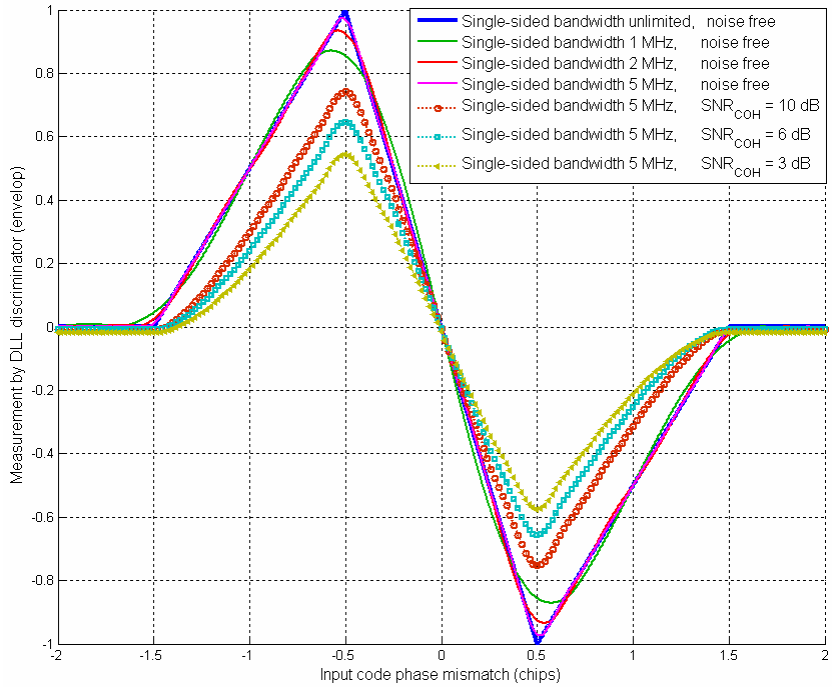


Figure 2-13: E-L envelope discriminator's response in the presence of noise and restricted pre-correlation filtering bandwidth (standard correlator spacing $d = 1$)

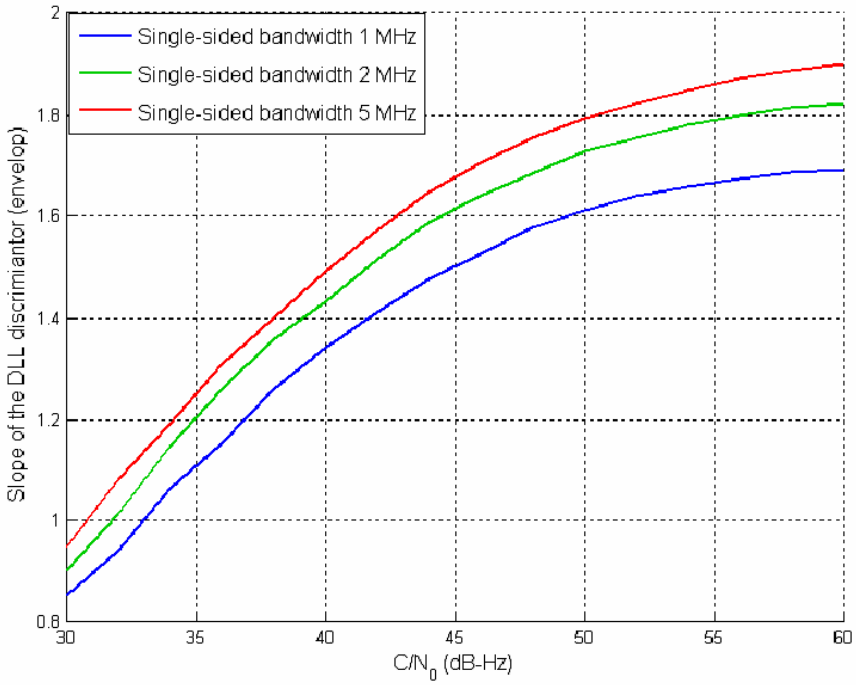


Figure 2-14: Slope of E-L envelope discriminator vs. $C/N_0$

Figure 2-12 presents the impact of pre-correlation filtering bandwidth on the response of the three types of discriminators. Results reveal that the linear operation region of E-L envelope discriminator is wider than other types of discriminators. The restricted bandwidth of the pre-correlation filter smoothes the sharp roll-off pattern coming into shape without consideration of the bandwidth effect.

Figure 2-13 evaluates the E-L discriminator's response from statistical consideration under different SNR and pre-correlation filtering conditions. The slope of the linear operation region diverges away from the noise-free reference with the deterioration of SNR conditions. As the function to estimate the code phase mismatch is derived from the noise-free profile, the real SNR situation implies a measurement bias that lowers the accuracy of code tracking. The relationship between slope of the E-L envelope discriminator and the SNR condition is derived from Monte Carlo simulations.

Figure 2-14 shows this result, where the COH inverval is 1 ms and three pre-correlation bandwidths are considered. The deviation is inversely proportional to the bandwidth and post-COH SNR. The noise-free reference yields a slope of 2 that cannot be attained even in the very strong post-COH SNR scenario. In the weak SNR (0 dB) situation, the relative error in slope exceeds 55%. The code misalignment estimate error resulting from the SNR can be estimated by

$$\delta\tau_{e,k} = \left|E - L\right| \cdot \left| \frac{1}{slope_{SNR}} - 0.5 \right| \tag{2.19}$$

where

$\delta\tau_{e,k}$ is error for code misalignment,

$|E-L|$ is the output from the E-L envelope discriminator, and

$slope_{SNR}$ represents the slope of discriminator's response at a certain post-COH SNR.

The narrow correlator exhibits excellent capability in mitigating the multipath error (Ray 2005). In addition, the noise samples at early and late correlators are dependent on each other as a function of correlator spacing as (Parkinson & Spilker 1996)

$$E\left(\overline{n}_{e,Ch1,k}\overline{n}_{l,Ch2,k}\right)\Big|_{Ch1,Ch2=I/Q} = \frac{N_0}{CT_{COH}}\left[1-\frac{d_{Correlator}}{T_c}\right]\delta_{Ch1,Ch2} \tag{2.20}$$

where

$d_{Correlator}$ is the correlator spacing, and

$\delta_{i,j}$ is the Kronecker product, indicating the noise term at the in-phase arm is independent from that at quadra-phase arm.

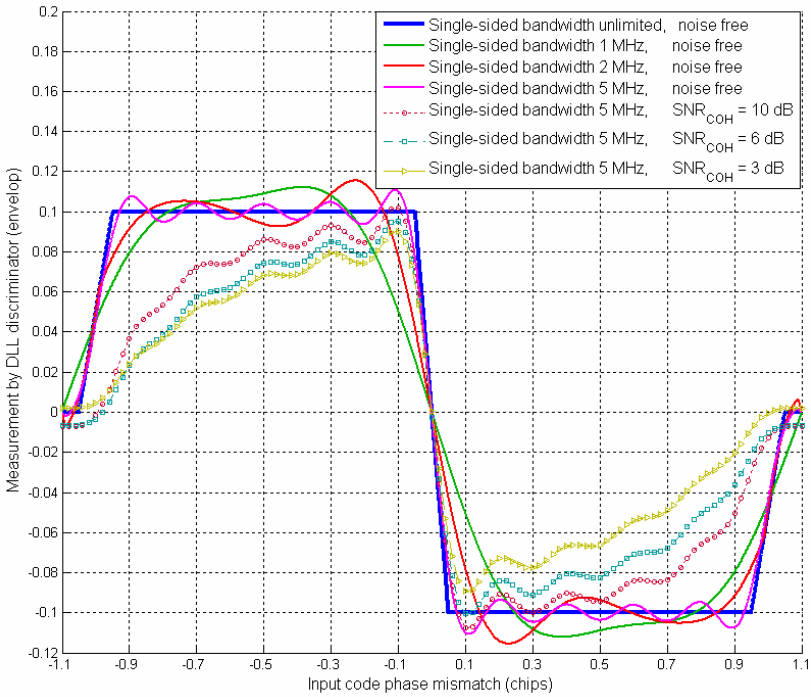


Figure 2-15: E-L envelope discriminator's response in the presence of noise and restricted pre-correlation filtering bandwidth (narrow correlator spacing $d_{correlator} = 0.1$)

A narrower spacing results in a stronger correlation between noise terms, meaning that the noise disturbance can be largely cancelled by early minus late operation. However, the response of the narrow correlator is severely distorted in the band limited case, as the red curve compared with the blue reference in Figure 2-15. Such characteristics require a wide pre-correlation filtering bandwidth and high sampling rate for the use of this technique. This figure also shows the narrow correlator's response in the presence of the noise derived through Monte Carlo simulation. Compared with the results in Figure 2-13, the response for high SNR is not significantly different from that for low SNR; this advantage comes from the correlation in eq. (2.20). When the timing error increases, signal

component of E-L decreases quickly due to the correlation degradation; therefore, E-L in large part reveals the statistics of correlated noise.

The wide bandwidth after the COH accumulation makes the measurements from the DLL's discriminator too noisy to be used directly; therefore, a low pass filter is applied immediately to reduce the noise disturbance.

## 2.3 Measures of Oscillator in Terms of Frequency Stability

The Allan variance (AVAR) is commonly used to evaluate the frequency stability of an OSC. The approach to derive AVAR from a set of collected random samples is described in this section. The method is then used to validate the Kalman filter-based OSC model described in section 2.4.

### 2.3.1 Basic Definition

OSC timing error originates from the oscillator deviation from clock's nominal frequency. Allan (1987) and Gierkink (1999) describe the OSCs' behavior in detail. The OSC's frequency fluctuation is classified into systematic (deterministic) and random variations. Systematic variation of the OSC's periodicity is associated with the fluctuations external to the OSC circuit and can be minimized by applying appropriate circuit techniques. The random variations result from the noise, produced in active and passive components of the OSC circuit, that modulates the frequency of oscillation. The random fluctuations of the receiver's clock present in the received IF signal are explicitly expressed by $\delta\theta^{Osc}(t)$ in eq. (2.6). According to Gierkink (1999), the instantaneous fractional frequency fluctuation is associated with the OSC PHN by

$$\delta f_r^{Osc}(t) = \frac{\left( \frac{d\left[\delta\theta^{Osc}(t)\right]}{dt} \right)}{2\pi f_0^{Osc}} = \frac{\delta f^{Osc}(t)}{f_0^{Osc}} \tag{2.21}$$

where

$f_0^{Osc}$ is the OSC's reference operating frequency, and

$\delta f_r^{Osc}(t)$ is the random instantaneous frequency fluctuation.

### 2.3.2 Power-law Spectral Density Model

The random frequency or phase fluctuations are composed of several stochastic random processes, named white frequency modulation (WFM), flicker frequency modulation (FFM), and random walk frequency modulation (RWFM) (Gierkink 1999, Allan 1987). The manufacturer usually releases reference parameters for each type of OSC. These parameters specify the strength of each stochastic process as in Table 2-2, where $h_0$, $h_{-1}$, and $h_{-2}$ respectively specify the intensity of WFM, FFM, and RWFM. These values are included in the power-law PSD for fractional frequency fluctuation (Gierkink 1999):

$$S_{\delta f_r^{Osc}}(f) = \sum_{i=-2}^{0} h_i f^i \tag{2.22}$$

Table 2-2: Parameters for a set of OSCs

| | OSC Parameters | | |
|---|---|---|---|
| | $h_0$ (WFM) | $h_{-1}$ (FFM) | $h_{-2}$ (RWFM) |
| XO | $2\times10^{-19}$ | $7\times10^{-21}$ | $2\times10^{-20}$ |
| TCXO | $1\times10^{-21}$ | $1\times10^{-20}$ | $2\times10^{-20}$ |
| OCXO | $8\times10^{-20}$ | $2\times10^{-20}$ | $4\times10^{-23}$ |
| Rubidium | $2\times10^{-20}$ | $7\times10^{-24}$ | $1\times10^{-29}$ |
| Cesium | $1\times10^{-19}$ | $1\times10^{-25}$ | $2\times10^{-23}$ |

OSCs listed in Table 2-2 can be classified into Quartz crystal and atomic standard. Crystal OSCs (OX) exhibit commercial merits such as low power consumption and cost, the small size and light weight, and the high mean time between failure (MTBF). However this type of low-cost unit compromises the measurement accuracy due to (1) higher long-term instability indicated by intensity of RWFM in Table 2-2, and (2) sensitivity to the temperature variation (Raquet 2006). To mitigate the oscillating deviation originating from the fluctuation of temperature, one can either compensate for the temperature variation or mount the OSC in a temperature-stable environment; the former technique is the basis for the temperature controlled crystal OSC (TCXO) and the latter method is used in an oven controlled crystal OSC (OCXO). Compared with crystal OSCs, the atomic OSCs reveal improvement in accuracy by about 2 to 3 orders, and in aging by about 1 to 2 orders (Vig 1992). This frequency standard is uniformly used in the satellites and determines their life. The sound oscillating stability is achieved at the expenses of other weaknesses such as long warm-up time, worse MTBF, large size and prohibitive cost for wide use.

### 2.3.3 Allan Variance

The AVAR is a measure of frequency stability in the time domain. As is well known, the classical variance measures the variation of a random process over an observation interval. It is related to the PSD of the random process, specifically for $\delta f_r^{Osc}(t)$, as

$$\sigma^2_{NormalVar}(\tau_{VAR}) = \int_0^{+\infty} S_{\delta f_r^{Osc}}(f)\left[\frac{2\sin(\pi f \tau_{VAR})}{\pi f \tau_{VAR}}\right]^2 df \qquad (2.23)$$

(Gierkink 1999). This integration in eq. (2.23) cannot be evaluated because PSD of the frequency variation is immeasurable at the zero frequency. Therefore, in lieu of directly measuring the variation of the random process, AVAR is used to measure the variation of the derivative of the random process (Gierkink 1999). Eq. (2.24) describes the relationship between the AVAR and the PSD of a random process.

$$\sigma^2_{Allan}\left(\tau_{AVAR}\right) = \int_0^{+\infty} S_{\delta f_r^{Osc}}\left(f\right) \frac{2\sin^4\left(\pi f \tau_{AVAR}\right)}{\left(\pi f \tau_{AVAR}\right)^2} df \tag{2.24}$$

The resultant AVAR, derived by substituting the specific PSD in eq. (2.22) into eq. (2.24), becomes (Parkinson & Spilker 1996, Irsigler & Eissfeller 2002)

$$\sigma^2_{Allan}\left(\tau_{AVAR}\right) = \frac{h_0}{2\tau_{AVAR}} + 2\ln(2) h_{-1} + \frac{2\pi^2}{3}\tau_{AVAR} h_{-2} \tag{2.25}$$

Gierkink (1999) describes the procedure to measure the AVAR over different intervals based on a random serial sampled every $T_s$ second. This method will be adopted to validate the OSC PHN model described in Section 2.4.

Given a OSC's PHN serial $\left\{\delta\theta_i^{Osc}\right\}$, the following equation quantifies the expected AVAR:

$$\sigma^2_{Allan}\left(\tau_{AVAR}\right) = \frac{1}{2}\frac{1}{N-2n}\sum_{k=1}^{N-2n}\left(\frac{\Delta^2\left(\delta\theta_i^{Osc}\right)}{2\pi f_0^{Osc}\tau_{AVAR}}\right) \tag{2.26}$$

where

$N$ is the total number of samples in the serial, and

$n$ is the number samples within the interval over which AVAR is concerned, i.e. $n = \tau_{AVAR}/T_s$,

$\Delta^2(\cdot)$ is the second derivative of the serial, defined as $\Delta^2(x_i) = x_i - 2x_{i-1} + x_{i-2}$.

## 2.4 Receiver Oscillator PHN Modeling

### 2.4.1 A Precise Oscillator Model based on Diffusion Coefficient

The OSC timing jitter, also named OSC PHN, is of particular importance for satellite navigation systems, such as GPS (Chaffee 1987, Zucca & Tavella 2005) and the new Galileo, for evaluating and assessing the accuracy, availability, and capability the system can achieve. The oscillator's instability can be suitably modeled by the random processes satisfying stochastic differential equation (SDE) (Davis et al. 2005, Zucca & Tavella 2005); this model is of particular importance to evaluate the impact of clock noise on the receiver's tracking performance, to predict and characterize clock behavior, and to replicate clock data using filtering techniques (e.g. the KF). The KF is able to characterize the random aspects of a physical system as a dynamic model using a priori information derived from the previous estimation and the statistics of the super-imposed noises. Existing KF-based algorithms model the PHN as a linear combination of white frequency modulation (WFM), random walk frequency modulation (RWFM) and flicker frequency modulation (FFM) (Davis et al. 2005, Zucca & Tavella 2005). WFM is a broadband phase noise usually produced in amplification stages; RWFM results from the oscillator´s physical environment; FFM characterizes the resonances of active oscillators, whose spectrum density takes the form of $1/f$ (Zucca & Tavella 2005). Besides these three

random modulations, the random run frequency modulation describes the time variation of the frequency drift, leading to a non-stationary Allan variance (Zucca & Tavella 2005); therefore, this process is not usually specified by the manufacturer and is not discussed here. To be included in a KF, the pure FFM process could be approximated by the Barnes–Jarvis and Mandelbrot approximations (Davis et al. 2005). Both methods generate a stationary process that represents the non-stationary noise over a limited time interval, which can easily be made longer than the application. Due to the simplicity and computation optimality, the Mandelbrot approach is employed here, which approximates the FFM by a sum of independent stationary Gauss-Markov (GM) processes running in parallel (Davis et al. 2005). The continuous model given by Davis et al. (2005) is first reviewed, based on which the digitized approach to implement it is derived. Finally, the digital implementation results are validated using the measure of AVAR described in the previous section. Hereby, four GM processes are used to simulate the FFM, and the time constants of these GM processes are of a group of geometric progression.

Each GM frequency process and associated phase offset satisfy the differential equation of

$$\begin{aligned} \frac{d\left(\delta\theta_{GM}^{Osc}(t)\right)}{dt} &= \delta f_{GM}^{Osc}(t), \\ \frac{d\left(\delta f_{GM}^{Osc}(t)\right)}{dt} &= -R_{GM}\cdot\delta f_{GM}^{Osc}(t)+n(t) \end{aligned} \tag{2.27}$$

(Davis et al. 2005), where

$\delta\theta_{GM}^{Osc}(t)$ is the phase noise resulting from a GM process, and

$\delta f_{GM}^{Osc}(t)$ is the frequency perturbation derived from a GM process,

$R_{GM}$ is the reciprocal of the time constant, and

$n(t)$ is the white noise process with a variance of $\sigma_{GM}^2$.

This GM process can be simulated in discrete time and used in a Kalman filter by solving it over a time interval of $T_s$. The differential equation takes the form of (Davis et al. 2005)

$$\begin{bmatrix} \delta\theta_{GM}^{Osc}(t) \\ \delta f_{GM}^{Osc}(t) \end{bmatrix} = \begin{bmatrix} 1 & \frac{1-e^{-R_{GM}T_s}}{R_{GM}} \\ 0 & e^{-R_{GM}T_s} \end{bmatrix} \begin{bmatrix} \delta\theta_{GM}^{Osc}(t-T_s) \\ \delta f_{GM}^{Osc}(t-T_s) \end{bmatrix} + \begin{bmatrix} n_{\delta\theta_{GM}^{Osc}}(t) \\ n_{\delta f_{GM}^{Osc}}(t) \end{bmatrix} \tag{2.28}$$

where the random noise vector $\underline{n}(t) = \begin{bmatrix} n_{\delta\theta_{GM}^{Osc}}(t) & n_{\delta f_{GM}^{Osc}}(t) \end{bmatrix}^T$ has a covariance matrix of

$$\sigma_{GM}^2 \begin{bmatrix} T_s^3 a_{11}(R_{GM}T_s) & T_s^2 a_{12}(R_{GM}T_s) \\ T_s^2 a_{12}(R_{GM}T_s) & T_s\, a_{22}(R_{GM}T_s) \end{bmatrix} \tag{2.29}$$

and

$$a_{11}(x) = \frac{-3/2 + x + 2e^{-x} - e^{-2x}/2}{x^3} \tag{2.30}$$

$$a_{12}(x) = \frac{1/2 - e^{-x} + e^{-2x}/2}{x^2} \tag{2.31}$$

$$a_{22}(x) = \frac{1-e^{-2x}}{2x} \tag{2.32}$$

By investigating the autocorrelation function for GM processes, $\delta f_{GM}^{Osc}(t)$, the PSD of this process is achieved through the Fourier transform of this autocorrelation function. Using this PSD in eq. (2.24), the corresponding AVAR resulting from this GM process takes the form of

$$\sigma_{Allan}^2\left(\tau_{AVAR}\right)=\frac{\sigma_{GM}^2}{2R_{GM}}\frac{-3+4e^{-R_{GM}\tau_{AVAR}}-e^{-2R_{GM}\tau_{AVAR}}+2R_{GM}\tau_{AVAR}}{R_{GM}^2\tau_{AVAR}^2} \tag{2.33}$$

Based on the model for each GM process, a six-state KF is used to accommodate all the random processes including WFM and RWFM, and four GM processes to approximate the FFM. The transition matrix and the noise samples are two critical components to propagate the model in time. Analytically,

$$\underline{x}_k^{Osc}=\Phi^{Osc}\underline{x}_{k-1}^{Osc}+\underline{n}_k \tag{2.34}$$

where

$\underline{x}_k^{Osc}=\left[\delta\theta^{Osc}\quad \delta f^{Osc}\quad \delta f_{GM,1}^{Osc}\quad ...\quad \delta f_{GM,4}^{Osc}\right]_k^T$, $\delta\theta^{Osc}$ represents the OSC-induced phase variation, $\delta f^{Osc}$ describes the OSC frequency variation, and $\delta f_{GM,i}^{Osc}$ is the state for the *ith* GM process.

$$\Phi^{Osc}=\begin{bmatrix} 1 & T_s & \frac{1-e^{-R_{GM,1}T_s}}{R_{GM,1}} & ... & \frac{1-e^{-R_{GM,4}T_s}}{R_{GM,4}} \\ 0 & 1 & 0 & ... & 0 \\ 0 & 0 & e^{-R_{GM,1}T_s} & ... & 0 \\ ... & ... & ... & ... & ... \\ 0 & 0 & 0 & ... & e^{-R_{GM,4}T_s} \end{bmatrix}, \text{ and}$$

$\underline{n}_k=\left[n_1\quad n_2\quad n_3\quad n_4\quad n_5\quad n_6\right]_k^T$.

$R_{i+1}=R_i/8$ quantifies the time constants between two adjacent GM processes.

The transition matrix is given by Davis et al. (2005), which, however, doesn't describe the noise terms driving the propagation of this discrete model. Based on the covariance matrix of the noise vector $\underline{n}_k$

$$Q_{\underline{n}} = \begin{bmatrix} Q_{\underline{n},11} & \frac{\sigma_{RWFM}^2 T_s^2}{2} & \sigma_{GM,1}^2 T_s^2 a_{12}\left(R_{GM,1} T_s\right) & \ldots & \sigma_{GM,4}^2 T_s^2 a_{12}\left(R_{GM,4} T_s\right) \\ \frac{\sigma_{RWFM}^2 T_s^2}{2} & \sigma_{RWFM}^2 T_s & 0 & \ldots & 0 \\ \sigma_{GM,1}^2 T_s^2 a_{12}\left(R_{GM,1} T_s\right) & 0 & \sigma_{GM,1}^2 T_s\, a_{22}\left(R_{GM,1} T_s\right) & \ldots & 0 \\ \ldots & \ldots & \ldots & \ldots & \ldots \\ \sigma_{GM,4}^2 T_s^2 a_{12}\left(R_{GM,4} T_s\right) & 0 & 0 & \ldots & \sigma_{GM,4}^2 T_s\, a_{22}\left(R_{GM,4} T_s\right) \end{bmatrix} \quad (2.35)$$

with

$$Q_{\underline{n},11} = \sigma_{WFM}^2 T_s + \frac{\sigma_{RWFM}^2 T_s^3}{3} + \sum_{i=1}^{4} \sigma_{GM,i}^2 T_s^3 a_{11}\left(R_{GM,i} T_s\right) \quad (2.36)$$

where

$\sigma_{WFM}$ is intensity of the WFM process, and

$\sigma_{RWFM}$ is intensity of the RWFM process.

Both values, respectively, are related to the intensity of the power spectra of an OSC by

$$\begin{aligned} \sigma_{WFM} &= \sqrt{\frac{h_0}{2}} \\ \sigma_{RWFM} &= \sqrt{2\pi^2 h_{-2}} \end{aligned} \quad (2.37)$$

The characteristic of the second order statistics for the process noise, eq. (2.35), is inherited in constructing the noise vector $\underline{n}_k$, which can be realized by a combination of ten i.i.d white Gaussian random serials as

$$n_1 = \sigma_{WFM}\sqrt{T_s}\, w_1 + \sigma_{RWFM} T_s \sqrt{\frac{T_s}{3}} w_2 + \sum_{i=3}^{6} \left(b_{i,1} w_{i,1} + b_{i,2} w_{i,2}\right) \quad (2.38)$$

$$n_2 = \sigma_{RWFM}\sqrt{T_s}\, w_2 \quad (2.39)$$

$$n_i = b_{i,3} w_{i,2} \left(i = 3 \sim 6\right) \quad (2.40)$$

where

$\left(w_1, w_2, w_{i,1}, w_{i,2}\right)\Big|_{i=3\sim 6}$ are independent identical distribution (i.i.d) Gaussian random variables with unit variance. $T_s$ is the interval between the two adjacent samples. The coefficients for eq. (2.38) are

$$b_{i,1} = \sigma_{GM,i-2}\sqrt{\frac{\left(-2 + R_{GM,i-2}T_s\right) + \left(2 + R_{GM,i-2}T_s\right)e^{-R_{GM,i-2}T_s}}{R_{GM,i-2}^3\left[1 + e^{-R_{GM,i-2}T_s}\right]}} \tag{2.41}$$

$$b_{i,2} = \sigma_{GM,i-2}\sqrt{\frac{\left[1 - e^{-R_{GM,i-2}T_s}\right]^3}{2R_{GM,i-2}^3\left[1 + e^{-R_{GM,i-2}T_s}\right]}} \tag{2.42}$$

$$b_{i,3} = \sigma_{GM,i-2}\sqrt{\frac{1 - e^{-2R_{GM,i-2}T_s}}{2R_{GM,i-2}}} \tag{2.43}$$

$\sigma_{GM,i-2}$ is the intensity for each GM process, which is related to intensity of the FFM by

$$U = \frac{\sigma_{FFM}^2}{2R_{GM,1}}\ ,\ \sigma_{GM,i-2} = \sqrt{2R_{GM,i-2}U}\ \ \left(i=3\sim 6\right) \tag{2.44}$$

Because $R_{GM,i-2} > R_{GM,i-1}$, the intensities of the four GM processes decay.

The term

$$\sigma_{FFM} = \sqrt{2\ln 2 \cdot h_{-1}} \tag{2.45}$$

reflects the relationship between the intensity of FFM and its specification in the frequency domain.

Based on the specification given by Table 2-2, Figure 2-16 illustrates the phase and frequency deviations of a TCXO over a 10 second interval. The frequency and phase devia-

tions presented in this figure are assumed to be modulated on the L1 carrier (1575.42 MHz). The curves in both subplots respectively represent the six states modeled in eq. (2.34)

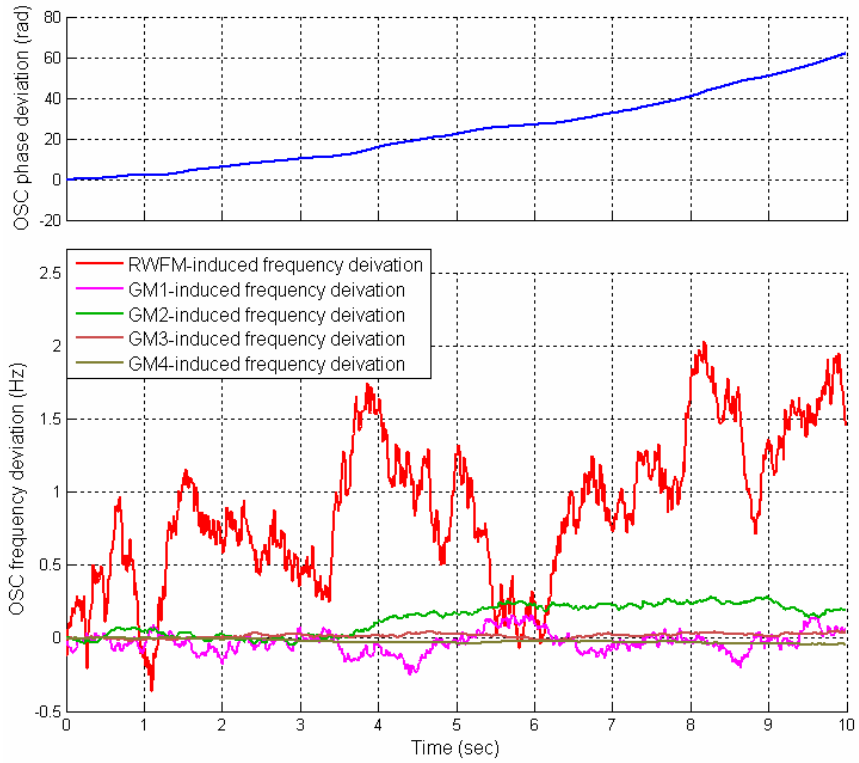


Figure 2-16: The phase and frequency noise samples induced by TCXO

Figure 2-17 shows the approximation of FFM by a combination of four GM processes as given in eq. (2.34). The reference time constant for the first GM process is selected as $R_{GM,1} = 1.89$ (Davis et al. 2005). All lines except the red curve are individual Allan deviations of each GM process over the time interval $\tau_{AVAR}$, derived from eq. (2.33). The symbols are numerical results for the Allan deviation using the created random samples and eq. (2.26).. From eq. (2.25), which quantifies the contribution to AVAR by each possible random modulation, the stability of an OSC can be evaluated over short-, medium-, and long-term intervals. These values are respectively determined as a function of

the intensity of the WFM, FFM, and RWFM. Therefore, the GM approximation is acceptable if this approach maintains a constant AVAR over a medium interval of an individual OSC.

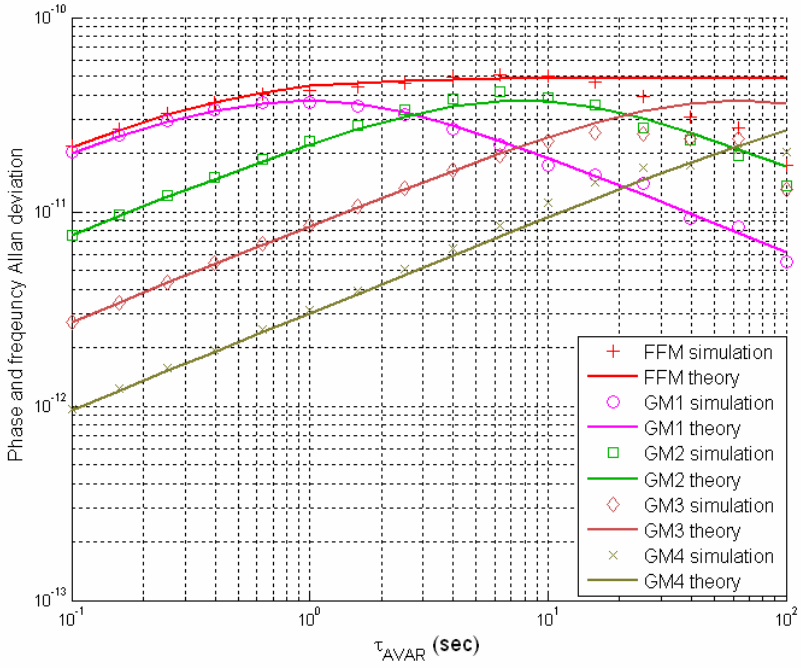


Figure 2-17: FFM approximation by four GM processes (TCXO)

Figure 2-18 is used to validate the OSC model by eq. (2.34) and the GM approximation. The dash lines are Allan deviations for four types of OSCs based on the specifications in Table 2-2. The symbols are numerical results derived from the random samples based on the KF-based model in eq. (2.34). A high quality atomic frequency standard is assumed for all satellites to drive the signal generation (Kaplan 1996). The satellites also broadcast predicted corrections for the on-board OSCs; therefore, the receiver's OSC, compared with the satellite's OSC, has a larger impact in determining the tracking capability and accuracy. The carrier tracking update rate for a GPS receiver is always less than 20 ms; as a result, the tracking jitter by PHN is associated with the short-term stability of the oper-

ating oscillator. This stability is determined by the intensity of the WFM process.

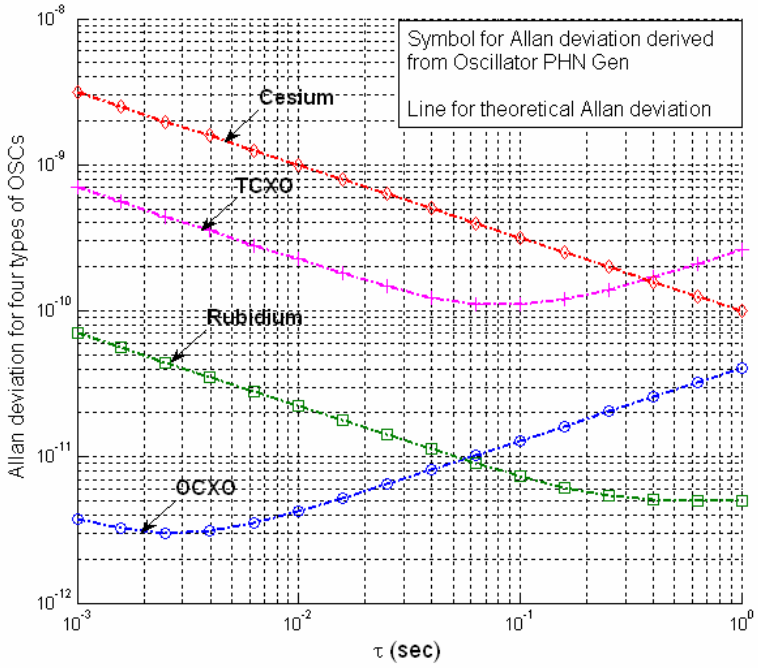


Figure 2-18: Allan deviation derived for OSC models

## 2.5 Ionospheric Scintillation Modeling

### 2.5.1 Amplitude and Phase Variations

During past decades, numerous researchers have investigated the characteristics of ionospheric variation by using GPS signals (Hegarty et al. 2001, Conker et al. 2003, Skone et al. 2005). A large GPS network, consisting of an array of GPS receivers, can be used to examine the spatial irregularity, velocity, and height of the electron density structures in the presence of ionospheric scintillation. To investigate the nature of the ionospheric irregularity, the receivers are specially required to provide accurate carrier phase and amplitude data, and to maintain tracking lock during the deep power fades and vigorous phase dynamics associated with scintillations (Pullen et al. 1998, Skone et al. 2005).

The ionospheric scintillation can lead to amplitude fades up to 25 dB (Skone et.al 2005); under such situations the carrier tracking reliability rapidly degrades due to the lower $C/N_0$ . Due to the nonlinearity between the observations and the phase misalignment, the operation of discriminators largely decreases $C/N_0$ . Experiments show, as demonstrated herein, that even an Ionospheric Scintillation Monitor (ISM) (Humphreys et al.. 2005) which employs wide-bandwidth loop filters (e.g. 15 Hz) will lose lock during strong equatorial scintillations.

The MITRE Centre for Advanced Aviation System Development has developed a scintillation signal model and also a GPS/Wide Area Augmentation System (WAAS) receiver model (Hegarty et al. 2001), to investigate the impact of scintillation on GPS/WAAS operations. By accounting for the amplitude variation caused by the ionospheric scintillation and disregarding the ambient noise, the received signal model of eq. (2.5) becomes

$$r(t) = \left[ A_0 \delta A^{Scint}(t) \right] d(t - \tau_{C/A}) c(t - \tau_{C/A}) cos\theta(t) \tag{2.46}$$

where

$A_0$ is the nominal signal carrier amplitude,

$\delta A^{Scint}(t)$ represents the amplitude variation induced by the ionospheric scintillation, and

$\delta\theta^{Scint}(t)$ is the scintillation-triggered phase variation, included in $\theta(t)$ as expressed by eq. (2.6).

The intensity variation,

$$\delta I^{Scint} = \left(\delta A^{Scint}\right)^2 \tag{2.47}$$

is the square of the amplitude variation and obeys a Nakagami-m distribution (Hegarty et al. 2001) as

$$f\left(\delta I^{Scint}\right) = \frac{m^m \left(\delta I^{Scint}\right)^{m-1}}{\Gamma(m)\Omega^m} e^{-m\delta I^{Scint}/\Omega} \tag{2.48}$$

where

$\Omega = E\left(\delta I^{Scint}\right)$ is the expectation of the intensity variation, and

$\Gamma(\cdot)$ is a Gamma function defined as $\Gamma(x) = \int_0^1 \left[ln\left(\frac{1}{t}\right)\right]^{x-1} dt$

The amplitude scintillation index is given as

$$\frac{1}{m} = \frac{\left(E\left(\delta I^{Scint} - \Omega\right)\right)^2}{\Omega^2} = S_4^2 \tag{2.49}$$

which measures the power variation induced by the scintillation. A larger $S_4$ is directly associated with deep power fades. This attenuation significantly jeopardizes the receiver's tracking performance, and may lead to the loss of navigation capabilities.

The phase variation in eq. (2.6) obeys

$$\delta\theta^{Scint} \sim N\left(0, \sigma^2_{\delta\theta^{Scint}}\right) \tag{2.50}$$

which is a zero-mean Gaussian distribution.

The magnitudes of the amplitude and phase scintillation can be classified respectively as a function of the commonly used scintillation parameters $S_4$ and $\sigma_{\delta\theta^{Scint}}$, as shown in

Table 2-3 (Hegarty et al. 2001, Skone et al. 2005).

Table 2-3: Scintillation intensity classification

| Case | $S_4$ | $\sigma_{\delta\theta^{Scint}}\left(rad\right)$ |
|---|---|---|
| Strong | 0.9 | 0.6 |
| Moderate | 0.6 | 0.3 |
| Weak | 0.4 | 0.2 |
| Very weak | 0.1 | 0.05 |

An experiment in (Pullen et al. 1998, Hegarty et al. 2001) shows that the amplitude and phase variation are negatively correlated by $\rho_{\delta I^{Scint},\delta\theta^{Scint}} = -0.6$.

Fourier analysis of experimental data illustrates the temporal correlation between the scintillation measurements (Pullen et al. 1998, Hegarty et al. 2001), i.e. the PSD of scintillation measurements is band-limited; therefore, PSD of scintillation variations is adapted for realistic simulations using spectrum shaping filters.

Shaping filters to create realistic PSD of intensity variation take the form of

$$\left|H\left(jf\right)\right|^2 = K\left\lfloor \frac{f^{2m_h}}{f^{2m_h}+c^{2m_h}} \right\rfloor_{Filter} \left\lceil \frac{d^{2m_l}}{f^{2m_l}+d^{2m_l}} \right\rceil_{Filter} \left[ \prod_{i=1}^{n} \frac{f^2+a_i^2}{f^2+b_i^2} \right]_{Filter} \tag{2.51}$$

(Pullen et al. 1998), where

$\lfloor\cdot\rfloor_{Filter}$ is $m_h$-order Butterworth high pass filter,

$\lceil\cdot\rceil_{Filter}$ is $m_l$-order Butterworth low pass filter, and

$[\cdot]_{Filter}$ represents n cascaded band pass filters that are used to form a flat response in the pass-band.

K is adjusted to satisfy

$$\int_0^{+\infty} \left| H(jf) \right|^2 df = 1 \tag{2.52}$$

Table 2-4 (Pullen et al. 1998) lists the shaping filter configuration for strong amplitude scintillation ($S_4$ > 0.8)

Table 2-4: Shaping filter configuration for strong amplitude scintillation

| | |
|---|---|
| $m_h = 2$ | $m_l = 2$ |
| $c = 0.1(Hz)$ | $d = 0.7(Hz)$ |
| $a_1 = 1.75(Hz)$ | $b_1 = 1.25(Hz)$ |
| $a_2 = 2.75(Hz)$ | $b_2 = 2.25(Hz)$ |

The shaping filter configuration leads to a high-frequency roll-off slope parameter of -5.5. For the medium and weak intensity scintillation, slopes of -3.0 and -2.5 are used respectively.

Table 2-5 Shaping filter configuration for phase scintillation

| | |
|---|---|
| $m_h = 5$ | $m_l = 1$ |
| $c = 0.1(Hz)$ | $d = 0.1(Hz)$ |
| $a_1 = 2.5(Hz)$ | $b_1 = 1.5(Hz)$ |
| $a_2 = 15(Hz)$ | $b_2 = 10(Hz)$ |

The PSD for the phase scintillation is known to take the form $S_{\delta\theta^{Scint}}(f) = Tf^{-p}$, where *T*,

in $\left(rad^2 / Hz\right)$, indicates the strength at *f=1 Hz*, and *p* is a unitless slope that is typically 2.0-3.0 (Hegarty et al.. 2001). The parameters of shaping filter for phase scintillation are listed in Table 2-5 (Pullen et al. 1998).

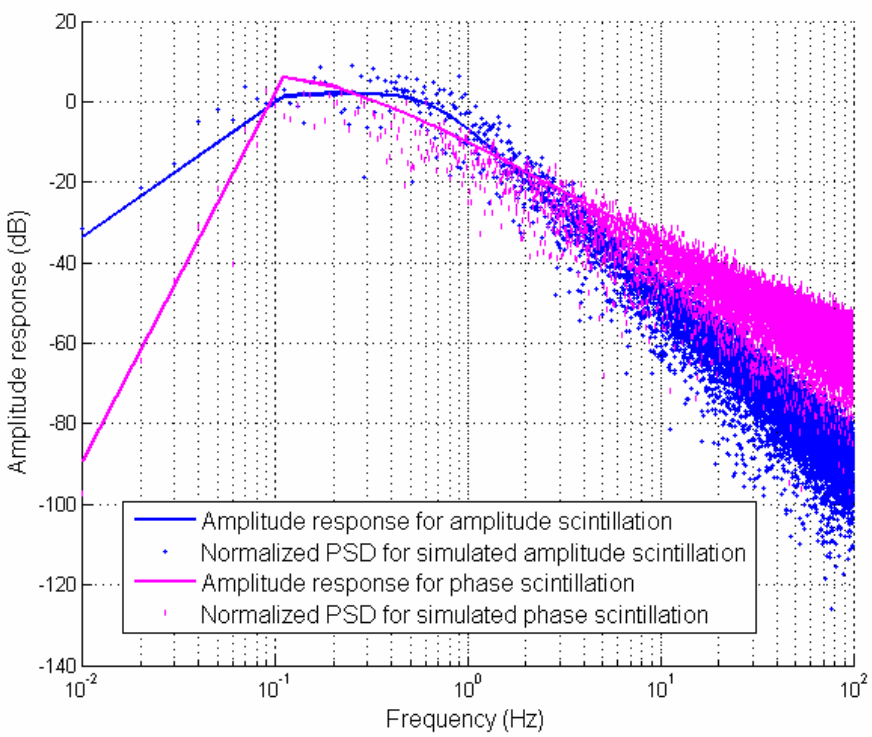


Figure 2-19: Amplitude response of shaping filters for amplitude and phase variation

The solid lines in Figure 2-19 represent the amplitude responses of the Butterworth approximations modeled by eq. (2.51), respectively, for scintillation-induced amplitude and phase variations. The shaping filters are respectively parameterized by Table 2-4 and Table 2-5. Pullen et al. (1998) demonstrates that patterns of the shaping filters in Figure 2-19 agree well with the experimental results.

### 2.5.2 Wideband Model (WBMOD) For Ionospheric Scintillation

The transformation matrix

$$\begin{bmatrix} 1 & 0 \\ \rho_{\delta\theta^{Scint},\delta I^{Scint}} \dfrac{\sigma_{\delta\theta^{Scint}}}{S_4} & \sigma_{\delta\theta^{Scint}}\sqrt{1-\rho^2_{\delta\theta^{Scint},\delta I^{Scint}}} \end{bmatrix} \tag{2.53}$$

is used to realize the negative correlation between amplitude and phase variations. After shaping the PSD of intensity scintillation samples, the PDF of this random series does not satisfy the Nakagami-m or Gamma distribution, as in the model in Pullen et al. (1998); therefore, in Figure 2-20, each variable at stage A is mapped into a variable at stage B, where both variables possess the identical cumulative probability. Because the PDF at stage B is Nakagami-m distribution, the process between A and B can make it a desired distribution.

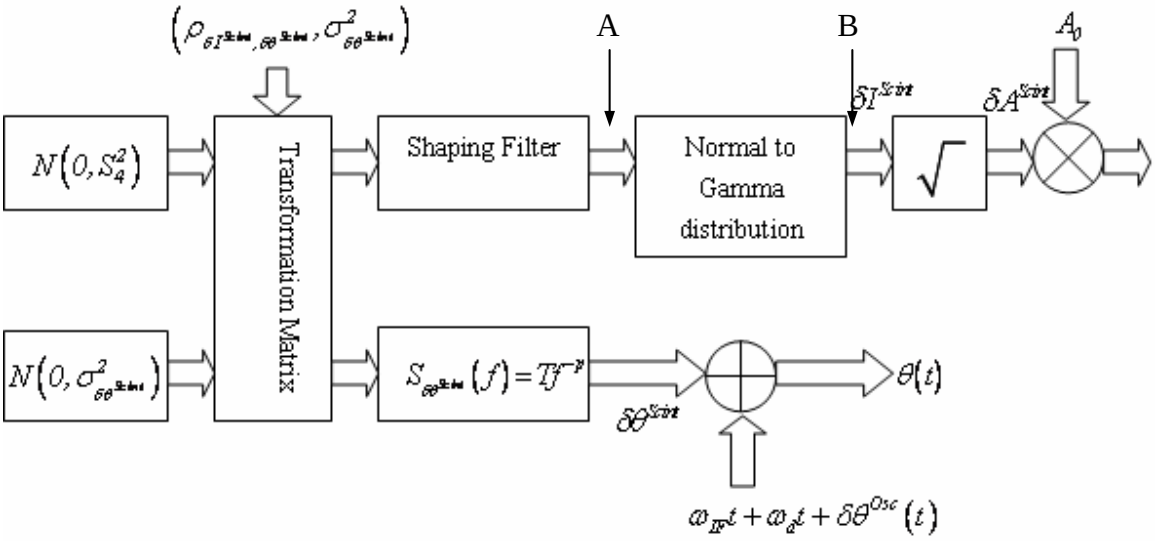


Figure 2-20: Discrete ionospheric scintillation model

To verify the PSD of amplitude and phase fluctuations, we use FFT techniques to analyze the PSD of 50-second samples created by the process in Figure 2-20 (e.g. the markers displayed in Figure 2-19). Combined with the experimental results in Pullen et al. (1998),

this verification validates that the simulated variations can describe the fluctuation caused by the ionospheric scintillation.

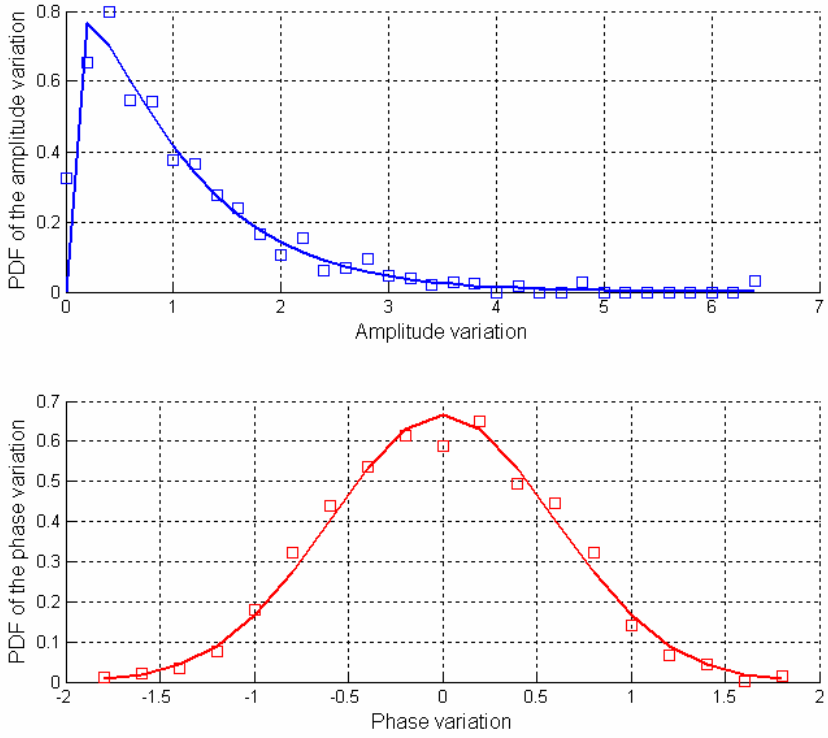


Figure 2-21: PDF of the scintillation-induced amplitude and phase variation

Figure 2-21 illustrates PDFs of the resultant intensity and phase variation, where $S_4 = 0.9$ and $\sigma_{\delta\theta^{Scint}} = 0.6\ rad$ are assumed. The solid line is the ideal Nakagami-m distribution (for intensity) and normal distribution (for phase) based on the standard deviation assumed for each random process. The symbols represent the PDFs resulting from the resultant random samples.

Figure 2-22 presents time series of the amplitude variation $\left(\delta A^{Scint}\right)$ and phase variation $\left(\delta\theta^{Scint}\right)$ simulated over a 20-second interval. The assumed scintillation level is identical

to the case shown in Figure 2-21. The increasing amplitude occurs with a decrease in phase variation, showing that the two variations are negatively correlated. The duration where $\delta A^{Scint} < 1$ represents the occurrence of power fades, which can be quantified in dB by $-20\log_{10}\left(\delta A^{Scint}\right)$.

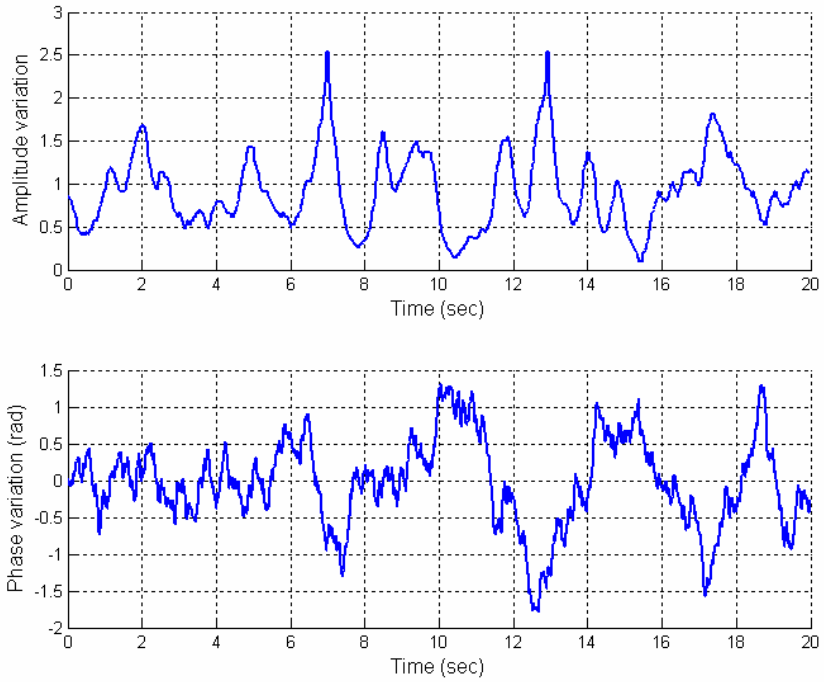


Figure 2-22: Scintillation-induced amplitude and phase variation

Figure 2-21 and Figure 2-22 demonstrate that the scintillation simulation model shown in Figure 2-20 can realize the model assumed in Pullen et al. (1998).

# Chapter 3 Acquisition Enhancement

This section demonstrates that the DFC approach allows a 2.5 dB improvement in processing loss as compared with NCH methods under weak signal conditions. The lesser loss results in a sensitivity improvement ranging from 1.2 dB to 1.6 dB for a detector based on the DFC strategy.

## 3.1 Differential Combining Acquisition

The GPS signal acquisition is equivalent to a binary hypothesis testing problem, where the signal model is constructed under two competing hypotheses. $H_0$ is referred to as the null hypothesis, corresponding to the case that the given satellite's signal is absent. Complementarily, $H_1$ refers to the alternative hypothesis, indicating the satellite to be acquired is present. By examining the statistic of the unit DV of $z_k$, we can quantify the nonlinear processing loss, specifically the squaring loss for the NCH detector (Figure 2-10). The performance of a detector can be evaluated through analyzing the test statistic as $T(z_k)$ in Figure 2-10 under both presumptions.

Differentially coherent correlation (Zarrabizadeh & Sousa 1997) was first introduced to improve the capacity of a commercial direct-sequence spread spectrum (DS-SS) CDMA system. It operates well in the presence of relatively high noise or interference by suppressing random and pseudo-random noise. Based on that scheme, a modified integration method (Choi et al. 2002) has also been proposed to acquire weak GPS signals; this

method can improve on the conventional NCH accumulation by introducing a constant processing loss. However, since a data bit sign reversal can negate the amplitude of accumulation, the modified integration is only suitable for AGPS receivers. In addition, the modified integration only uses coherent output from the in-phase channel, implying a perfect carrier phase alignment with all signal power concentrated in the in-phase channel; such carrier alignment is almost impossible during acquisition. In this paper, the acquisition approach of Choi et al. (2002) is modified and termed "DFC." The DFC approach is described and its statistical nature is explored. The results prove that DFC exceeds NCH in reducing the processing loss by about 3 dB in low post-COH SNR cases, resulting in an overall detection sensitivity improvement ranging from 1.2 and 1.6 dB.

### 3.1.1 Squaring Loss vs. Differential Processing Loss

The signals from all the visible satellites are available simultaneously at the receiver front end. Thus the outputs of Accum & Dump filter, by eqs. (2.10) and (2.11), actually consist of three types of terms: an autocorrelation term, if the desired satellite's signal is present; multiple cross-correlation terms from all other visible satellites, which are not explicitly included in eqs. (2.10) and (2.11); and bandlimited Gaussian noise. Cross-correlation interference or multiple access interference (MAI) in GPS processing is associated with the Doppler difference between two channels (Norman & Cahn 2005) and is characterized as wide-band noise (Holtzman 1994). This interference raises the noise level and degrades the detectors' performance. Even worse, the autocorrelation peak of a weak signal

can be lower than the cross-correlation peaks of stronger signals, resulting in failure to acquire on the weak channel. Fortunately, various types of interference cancellation have been extensively investigated to suppress the MAI, for example, successive interference cancellation method in Holtzman (1994). These methods are typically applied during the initial coherent accumulation of acquisition. Thus, the remnants of the MAI influence the DFC and NCH detectors equally. Therefore, in general, we can compare the detectors' performance by assuming that MAI has been suppressed sufficiently to be considered negligible in the remainder of this chapter.

With cross-correlation assumed negligible, and making the assumption that the satellite is in view, the COH units of eqs. (2.10) and (2.11) have the following general forms under the alternative hypothesis $H_1$. The reference for normalization does not alter the natural SNR which determines the capability and accuracy of acquisition and tracking. To simplify the following statistical analysis and sustain consistency of the results, the COH units have been normalized by the noise variance, taking the forms of

$$\bar{I}_{v,k}^{Noise} = d_{m,k}\sqrt{\frac{\left(N_k^{COH}\tilde{A}_k\right)^2}{2N_k^{COH}\sigma_s^2}}\cos\bar{\varphi}_k + \bar{n}_{v,I,k}^{Noise}, \text{ and} \tag{3.1}$$

$$\bar{Q}_{v,k}^{Noise} = d_{m,k}\sqrt{\frac{\left(N_k^{COH}\tilde{A}_k\right)^2}{2N_k^{COH}\sigma_s^2}}\sin\bar{\varphi}_k + \bar{n}_{v,Q,k}^{Noise} \tag{3.2}$$

where

$\sqrt{\frac{\left(N_k^{COH}\tilde{A}_k\right)^2}{2N_k^{COH}\sigma_s^2}}$ is the instantaneous SNR after COH unit, denoted by $\breve{A}_k^2$, and

$\bar{n}_{v,Ch,k}^{Noise}\Big|_{Ch=I/Q}$ is the normalized noise, equal to $\left.\dfrac{n_{v,Ch,k}^{Noise}}{\sigma_s\sqrt{N_k^{COH}/2}}\right|_{Ch=I/Q}$, and satisfying the distribution of $N(0,1)$.

If the detected signal is not present in the received samples, COH units consist of only white Gaussian noise (WGN) and the sum of the MAI residuals; as mentioned above, the latter is assumed to be negligible. This assumption yields COH unit normalized by noise variance, which takes the following forms under the null hypothesis, $H_0$:

$$\bar{I}_{v,k}^{Noise} = \bar{n}_{v,I,k}^{Noise}, \text{ and} \tag{3.3}$$

$$\bar{Q}_{v,k}^{Noise} = \bar{n}_{v,Q,k}^{Noise} \tag{3.4}$$

Acquisition is conducted to roughly estimate the code phase and Doppler offset. The location of the maximum prompt correlation inherits the correct information. Therefore, only the prompt correlation is used to form the test statistic at acquisition stage. The squaring loss results from the evaluation of a unit DV of

$$z_k^{NCH} = \sqrt{\bar{I}_{p,k}^{Noise^2} + \bar{Q}_{p,k}^{Noise^2}} \tag{3.5}$$

. This unit DV satisfies Rician distribution,

$$p\left(z_k^{NCH}\middle|H_1\right) = \breve{A}_k \, exp\left(-\frac{z_k^{NCH^2} + \breve{A}_k^2}{2}\right) I_0\left(z_k^{NCH}\breve{A}_k\right) \tag{3.6}$$

where

$I_0(\cdot)$ is the zero-order modified Bessel function of the first kind, formed by an

infinite summation of polynomials. $I_0(x) = \sum_{m=0}^{+\infty} \frac{\left(\frac{1}{4}x^2\right)^m}{(m+1)(m!)^2}$ is an even function, i.e. $I_0(x) = I_0(-x)$,

under $H_1$ hypothesis (Kay 1998), and Rayleigh distribution

$$p\left(z_k^{NCH} \middle| H_0\right) = z_k^{NCH}\, exp\left(-\frac{z_k^{NCH^2}}{2}\right) \tag{3.7}$$

under $H_0$ (Kay 1998). Kay (1998) also generally defines

$$SNR_{z_k^{NCH}} = \frac{\left(E\left(z_k^{NCH} \middle| H_1\right) - E\left(z_k^{NCH} \middle| H_0\right)\right)^2}{Var\left(z_k^{NCH} \middle| H_0\right)} \tag{3.8}$$

as the SNR for a DV used to decide the presence or absence of the desired signal. Particularly for the unit DV in eq. (3.5), the resultant SNR after NCH combination becomes

$$SNR_{post-NCH} = \sqrt{\frac{\pi}{4-\pi}}\left\{e^{-\breve{A}_k^2/8}\left[\left(1+\frac{\breve{A}_k^2}{4}\right)I_0\left(\frac{\breve{A}_k^2}{8}\right)+\frac{\breve{A}_k^2}{4}I_1\left(\frac{\breve{A}_k^2}{8}\right)\right]-1\right\} \tag{3.9}$$

where $I_1(\cdot)$ is the first-order modified Bessel function of the first kind (Lowe 1999). The squaring loss caused by the NCH combination is

$$L_{NCH}(dB) = 10\log_{10}\left(\breve{A}_k^2\right) - 10\log_{10}\left(SNR_{post-NCH}\right) \tag{3.10}$$

where $\breve{A}_k^2$ is the instantaneous post-COH SNR defined for eqs. (3.1) and (3.2). The squaring loss greatly challenges acquisition of the weak signal (Lachapelle 2005, Ray 2005). The upper curves in Figure 3-2 demonstrate that the squaring loss increases rapidly with the attenuation of post-COH SNR in dB. If the $C/N_0$ is 13 dB-Hz, 30 dB

lower than the nominal reference, the squaring loss reaches 10 dB using a strategy of 20 ms COH accumulation. To reduce this nonlinear processing loss, the DFC based detector is introduced and examined. Figure 3-1 illustrates the functional diagram of this detector, where the processing to achieve the COH units is identical to the NCH detector shown in Figure 2-10. Unlike the NCH detector, in lieu of using the prompt correlations at epoch $k$, the correlations at previous epochs are also used to form the unit DV as (Yu et al., 2006b)

$$z_k^{DFC} = \sqrt[4]{\left(\bar{I}_{p,k}^{Noise}\bar{I}_{p,k-1}^{Noise} + \bar{Q}_{p,k}^{Noise}\bar{Q}_{p,k-1}^{Noise}\right)^2 + \left(\bar{Q}_{p,k}^{Noise}\bar{I}_{p,k-1}^{Noise} - \bar{I}_{p,k}^{Noise}\bar{Q}_{p,k-1}^{Noise}\right)^2} \qquad (3.11)$$

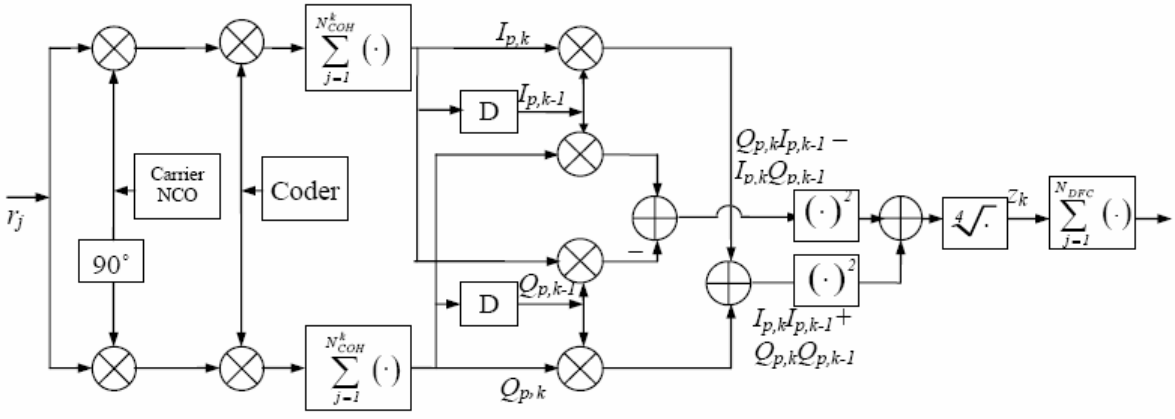


Figure 3-1: Diagram of the DFC-based detector

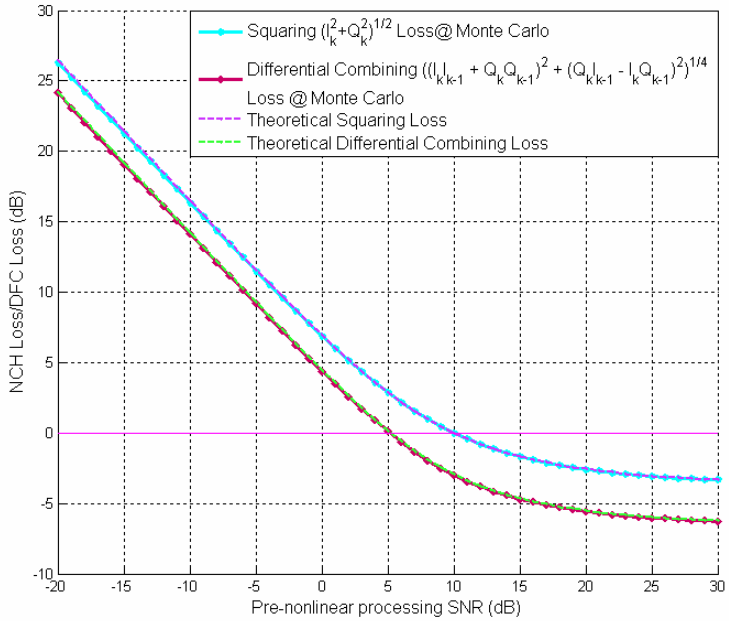


Figure 3-2: Nonlinear processing loss

Eq. (3.8) highlights that the conditional probability density function (PDF) is very necessary to assess the post-nonlinear SNR, a key value for the evaluation of nonlinear processing loss. The unit DV for DFC-based detector is analyzed on a general assumption mentioned in section 2.1.3: the sampling frequency just satisfies the Nyquist criteria, resulting in noise samples that are uncorrelated in time, i.e. noise components $\overline{n}_{p,I,k}^{Noise}$, $\overline{n}_{p,Q,k}^{Noise}$, $\overline{n}_{p,I,k-1}^{Noise}$, and $\overline{n}_{p,Q,k-1}^{Noise}$ are unit i.i.d. WGN with the well-known probability density function of

$$p(x) = \frac{1}{\sqrt{2\pi}} e^{-\frac{x^2}{2}} \tag{3.12}$$

where

$$x = \overline{n}_{p,I,k}^{Noise}, \overline{n}_{p,Q,k}^{Noise}, \overline{n}_{p,I,k-1}^{Noise}, \overline{n}_{p,Q,k-1}^{Noise}.$$

It can be seen in eqs. (3.1)-(3.4) that the COH units are the sum of a deterministic component and a noise term under hypothesis $H_1$, while equivalent to noise terms under hypothesis $H_0$. Therefore, the joint PDF of $\bar{I}_{p,k}^{Noise}, \bar{I}_{p,k-1}^{Noise}, \bar{Q}_{p,k}^{Noise}, \bar{Q}_{p,k-1}^{Noise}$ can be expressed as

$$p\left(\bar{I}_{p,k}^{Noise}, \bar{I}_{p,k-1}^{Noise}, \bar{Q}_{p,k}^{Noise}, \bar{Q}_{p,k-1}^{Noise}\right) = \prod_{j=k-1,k} p\left(\bar{n}_{p,I,j}^{Noise}\right) p\left(\bar{n}_{p,Q,j}^{Noise}\right) \tag{3.13}$$

where the noise terms are in fact a function of the corresponding COH unit, either $\bar{I}_p^{Noise}$ or $\bar{Q}_p^{Noise}$, and have either a zero mean or some non-zero mean. Utilizing eqs. (3.1)-(3.4) to replace $\bar{n}_{p,I,j}^{Noise}$ and $\bar{n}_{p,Q,j}^{Noise}$ with $\bar{I}_{p,j}^{Noise}$ or $\bar{Q}_{p,j}^{Noise}$ ( $j = k-1/k$ ) under two possible hypotheses, it is straightforward to obtain a conditional joint PDF as a function of COH units. Under hypothesis $H_0$, the joint PDF is

$$p\left(\bar{I}_{p,k}^{Noise}, \bar{I}_{p,k-1}^{Noise}, \bar{Q}_{p,k}^{Noise}, \bar{Q}_{p,k-1}^{Noise} \middle| H_0\right) = \left(\frac{1}{2\pi}\right)^2 e^{-\frac{1}{2}\sum_{j=k-1}^{k}\left[\bar{I}_{p,j}^{Noise^2} + \bar{Q}_{p,j}^{Noise^2}\right]} \tag{3.14}$$

Under hypothesis $H_1$, the joint PDF is similar, but the bias introduced by the non-zero mean terms is evident in the joint PDF as sinusoidal factors:

$$p\left(\bar{I}_{p,k}^{Noise}, \bar{I}_{p,k-1}^{Noise}, \bar{Q}_{p,k}^{Noise}, \bar{Q}_{p,k-1}^{Noise} \middle| H_1\right) = \left(\frac{1}{2\pi}\right)^2 e^{-\frac{1}{2}\sum_{j=k-1}^{k}\left[\left(\bar{I}_{p,j}^{Noise} - \breve{A}_j \cos\bar{\varphi}_j\right)^2 + \left(\bar{Q}_{p,j}^{Noise} - \breve{A}_j \sin\bar{\varphi}_j\right)^2\right]} \tag{3.15}$$

The following relations are used to map eqs. (3.14) and (3.15) from Cartesian coordinates to a polar system:

$$\bar{I}_{p,j}^{Noise} = r_j \cos\gamma_j \Big|_{j=k-1,k} \tag{3.16}$$

$$\bar{Q}_{p,j}^{Noise} = r_j \sin\gamma_j \Big|_{j=k-1,k} \tag{3.17}$$

and the resulting conditional joint PDFs for the DFC approach become

$$p\left(r_k,\, r_{k-1},\, \gamma_k,\, \gamma_{k-1} \middle| H_0\right) = \left(\frac{1}{2\pi}\right)^2 e^{-\frac{1}{2}\sum_{j=k-1}^{k} r_j^2} r_k r_{k-1} \tag{3.18}$$

$$p\left(r_k,\, r_{k-1},\, \gamma_k,\, \gamma_{k-1} \middle| H_1\right) = \left(\frac{1}{2\pi}\right)^2 e^{-\frac{1}{2}\sum_{j=k-1}^{k}\left[r_j^2+\breve{A}_j^2-2\breve{A}_j r_j \cos\left(\gamma_j-\bar{\varphi}_j\right)\right]} r_k r_{k-1} \tag{3.19}$$

By applying eqs. (3.16) and (3.17) to eq. (3.10), the DFC unit DV $z_k^{DFC}$ in polar co-ordinates is $\sqrt{r_k r_{k-1}}$. The conditional joint PDFs expressed by eqs. (3.18)-(3.19) are used to calculate the components in eq. (3.8) – the conditional expectation under hypothesis $H_0$ and $H_1$, and the variance under hypothesis $H_0$. These statistics are necessary to achieve post-DFC SNR. First, the conditional expectation under $H_1$ is calculated:

$$\begin{aligned} E\left(z_k^{DFC} \middle| H_1\right) &= \left(\frac{1}{2\pi}\right)^2 \int_0^{+\infty}\int_0^{+\infty} \sqrt{\left(r_k r_{k-1}\right)^3} e^{-\frac{1}{2}\left(\sum_{j=k-1}^{k}\left(r_j^2+\breve{A}_j^2\right)\right)} \left(\int_0^{2\pi}\int_0^{2\pi} e^{\sum_{j=k-1}^{k}\breve{A}_j r_j \cos\left(\gamma_j-\bar{\varphi}_j\right)} d\gamma_k d\gamma_{k-1}\right) dr_k dr_{k-1} \\ &= \prod_{j=k-1}^{k}\left[ e^{-\left(\frac{\breve{A}_j^2}{2}\right)} \int_0^{+\infty} \sqrt{r_j^3} e^{-\left(\frac{r_j^2}{2}\right)} I_0\left(\breve{A}_j r_j\right) dr_j \right] \\ &= \frac{2\pi}{\Gamma^2\left(3/4\right)} \prod_{j=k-1}^{k} L_{3/4}^{1}\left(\breve{A}_j{}^2/2\right) h\left(\breve{A}_j\right) \end{aligned} \tag{3.20}$$

where

$\Gamma(x)$ is the gamma function, defined as $\Gamma(x) \equiv \int_0^{+\infty} t^{x-1} e^{-t} dt$ , or $\Gamma(x) \equiv \int_0^1 \left[\ln\left(\frac{1}{t}\right)\right]^{x-1} dt$ ,

$L_n^{\lambda}(z)$ is a Laguerre polynomial, which is a solution of Laguerre's differential equation formulated as $xy'' + (1-x)y' + ny = 0$, where n is a real number,

$h\left(\breve{A}_j\right)$ equals to $\frac{1-\sqrt[4]{2}}{3}\breve{A}_j^4+\frac{\sqrt[4]{2}\cdot 10-4}{12}\breve{A}_j^2+\frac{\sqrt[4]{2}}{4}$.

The conditional expectation and variance under $H_0$ are calculated:

$$E\left(z_k^{DFC}\middle|H_0\right)=\left(\frac{1}{2\pi}\right)^2\int_0^{+\infty}\int_0^{+\infty}\sqrt{\left(r_k r_{k-1}\right)^3}e^{-\frac{1}{2}\sum_{j=k-1}^{k}r_j^2}\left(\int_0^{2\pi}\int_0^{2\pi}d\gamma_k d\gamma_{k-1}\right)dr_k dr_{k-1}$$
$$=\left[\int_0^{+\infty}\sqrt{r_k^3}e^{-\left(\frac{r_k^2}{2}\right)}dr_k\right]^2=\left[\frac{\sqrt[4]{8}\pi}{4\Gamma\left(3/4\right)}\right]^2 \tag{3.21}$$

$$E\left(z_k^{DFC^2}\middle|H_0\right)=\left(\frac{1}{2\pi}\right)^2\int_0^{+\infty}\int_0^{+\infty}\left(r_k r_{k-1}\right)^2 e^{-\frac{1}{2}\sum_{j=k-1}^{k}r_j^2}\left[\int_0^{2\pi}\int_0^{2\pi}d\gamma_k d\gamma_{k-1}\right]dr_k dr_{k-1}$$
$$=\left[\int_0^{+\infty}r_k e^{-\left(\frac{r_k^2}{2}\right)}dr_k\right]^2=\frac{\pi}{2} \tag{3.22}$$

$$Var\left(z_k^{DFC}\middle|H_0\right)=E\left(z_k^{DFC^2}\middle|H_0\right)-\left[E\left(z_k^{DFC}\middle|H_0\right)\right]^2 \tag{3.23}$$

Eq. (3.8) is a general form to compute SNR by replacing $z_k^{NCH}$ with $z_k^{DFC}$. Therefore, applying eqs. (3.20)-(3.23) to eq. (3.8) achieves the SNR after the DFC operation. This SNR is used to replace $SNR_{post-NCH}$ in eq. (3.10) to quantify the nonlinear processing loss by DFC, which is illustrated through the red and green curves in Figure 3-2. Through this figure, we can compare the SNR losses due to DFC and NCH processing for a set of post-COH SNR, varying from -20 dB to 30 dB and the $C/N_0$ correspondingly ranging from 13 dB-Hz to 63 dB-Hz with 1 ms COH accumulation. Clearly, unlike *post-NCH* SNR, the *post-DFC* SNR depends not only on $\breve{A}_k$ but on $\breve{A}_{k-1}$. During the acquisition stage, the amplitude degradation, mainly due to the line-of-sight (LOS) motion and the instability of the receiver's OSC, deteriorates over the processing interval. The LOS mo-

tion greatly impedes acquisition of the weak signal because the incoming Doppler varies rapidly. The weak signal acquisition, however, is always discussed in the frame of quasi-static status. Under this assumption, the two adjacent amplitudes can be assumed almost identical. Furthermore, the OSC's stability is assumed to be sufficient such that no additional rapid frequency variations occur between two adjacent COH accumulations. The degraded amplitude lowers the *post-NCH* and *post-DFC* SNRs simultaneously; therefore, making the assumption $\breve{A}_k = \breve{A}_{k-1}$ does not alter the comparison between the two methods. To simulate the squaring loss/DFC-processing loss, four random sequences of $\bar{I}_{p,k}^{Noise} / \bar{I}_{p,k-1}^{Noise}$ and $\bar{Q}_{p,k}^{Noise} / \bar{Q}_{p,k-1}^{Noise}$ are created based on eqs. (3.1) and (3.2) for the $H_1$ hypothesis, and on eqs. (3.3)-(3.4) for the $H_0$ hypothesis. The sequences are then combined using eq. (3.8) to obtain the statistics necessary to quantify the two nonlinear processing losses. The results validate the previous theoretical analysis, and demonstrate that DFC suffers from approximately 3 dB less processing loss as compared with NCH in the case of low *post-COH* SNR.

Figure 3-2 directly demonstrates that the DFC operation produces a smaller SNR loss than standard NCH integration. The following analyzes the origin of that benefit of DFC by examining the characteristics of noise. Substituting eqs. (3.3)-(3.4) to eq. (3.11), the random variable of noise for the DFC process is given as

$$n_{z_k,DFC} = \sqrt[4]{\prod_{j=k-1}^{k} \left( \bar{n}_{p,I,j}^{Noise^2} + \bar{n}_{p,Q,j}^{Noise^2} \right)} \tag{3.24}$$

Similarly, the random variable of noise for NCH integration is given as

$$n_{z_k,NCH} = \sqrt[4]{\left(\overline{n}_{p,I,k}^{Noise^2} + \overline{n}_{p,Q,k}^{Noise^2}\right)^2} \tag{3.25}$$

The Cauchy-Schwartz inequality, $\left[\int f(x)g(x)dx\right]^2 \le \int f^2(x)dx \int g^2(x)dx$ (Abramowitz & Stegun 1965) may be used to compare the noise variables:

$$\begin{aligned} E\left(n_{z_k,DFC}^4\right) &= E\left(\prod_{j=k-1}^{k}\left(\overline{n}_{p,I,j}^{Noise^2} + \overline{n}_{p,Q,j}^{Noise^2}\right)\right) \le \sqrt{\prod_{j=k-1}^{k} E\left(\left(\overline{n}_{p,I,j}^{Noise^2} + \overline{n}_{p,Q,j}^{Noise^2}\right)^2\right)} \\ &= E\left(\left(\overline{n}_{p,I,k}^{Noise^2} + \overline{n}_{p,Q,k}^{Noise^2}\right)^2\right) = E\left(n_{z_k,NCH}^4\right) \end{aligned} \tag{3.26}$$

The equality is achieved only if $\overline{n}_{p,I,k}^{Noise^2} + \overline{n}_{p,Q,k}^{Noise^2} = \overline{n}_{p,I,k-1}^{Noise^2} + \overline{n}_{p,Q,k-1}^{Noise^2}$, which is almost impossible for independent random variables; therefore the noise intensity of DFC is always less than that of the NCH approach. The benefit stems from the differential combination prior to the squaring operation.

The noise characteristics of DFC, however, are outperformed by standard COH accumulation. Since noise is squared after DFC, when several DFC unit DVs are accumulated, noise accumulates to a non-zero mean unlike the case of COH integration. DFC is therefore an intermediate performer between NCH and COH, but since extension of COH integration is often restricted by factors mentioned in the introduction, the DFC is preferable to NCH accumulation for weak signal acquisition.

### 3.1.2 Performance Evaluation on Differential Combining Approach

A binary detection problem suffers from two types of errors — false alarm and missed detection — which have some non-zero probability of occurrence (Kay 1998). The errors

are complementary, and can therefore be balanced against each other to optimize detection according to certain criteria. This relationship is clearly reflected in Figure 3-3 by shifting the critical threshold $T_{Acq}^{TH}$. The Neyman-Pearson (NP) criterion, which fixes the probability of false alarm and subsequently minimizes missed detection, is commonly adopted. The decision region is critical in determining the confidence of detection and the penalty of miss.

$$P_{FA} = \int_{T_{Acq} \geq T_{Acq}^{TH}} p\left(T_{Acq} \middle| H_0\right) dT_{Acq} = \alpha \tag{3.27}$$

where $T_{Acq}$ is the test statistic; in statistics, $\alpha$ is termed the significance level or size of the test (Kay 1998) which is illustrated by the cyan patch in Figure 3-3.

$$P_D = \int_{T_{Acq} \geq T_{Acq}^{TH}} p\left(T_{Acq} \middle| H_1\right) dT_{Acq} = 1 - \beta \tag{3.28}$$

In statistics, $P_D$ is termed the power of detection and $\beta$ quantifies probability of miss (Kay 1998) (shown as the yellow patch in Figure 3-3), where $T_{Acq}^{TH}$ is used to judge the presence or absence of signal based on the test statistic.

To correctly detect weak GPS signals, several unit DVs are essentially added together to form the test statistic $T_{Acq}$, or termed composite DV for making a judgment, because such accumulation can further increase SNR beyond COH gain and then improve the accuracy and reliability of detection.

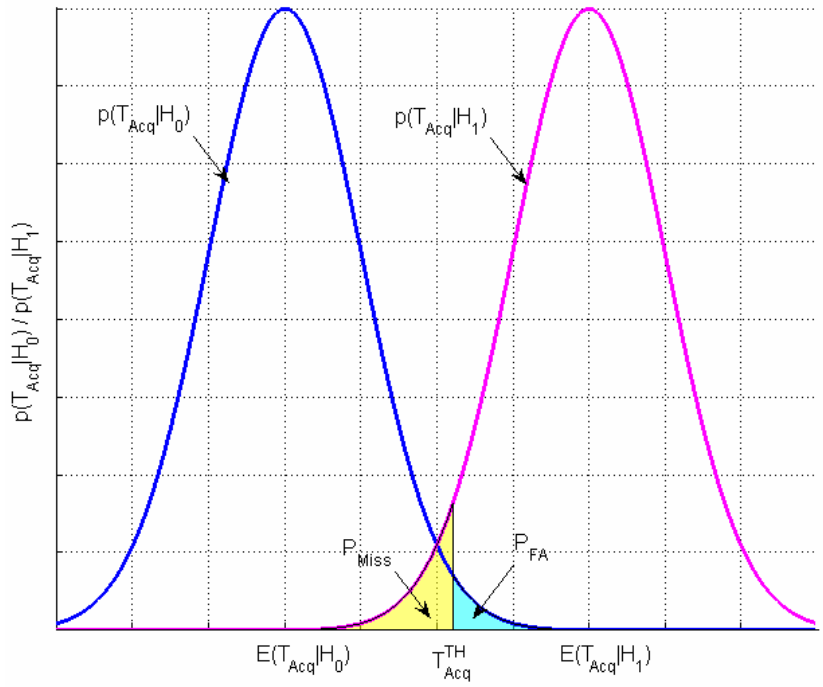


Figure 3-3 Binary detection problem in statistical sense

From (3.27) and (3.28), the conditional PDFs $p\left(T_{Acq}\middle|H_0\right)$ and $p\left(T_{Acq}\middle|H_1\right)$ are necessary to evaluate the detector performance and set a detection threshold, determined by the noise floor and required SNR for decision. Evaluation of the power composite DV $\sum_{k=1}^{N_{NCH}}\left(\bar{I}_{p,k}^{Noise^2}+\bar{Q}_{p,k}^{Noise^2}\right) / \sum_{k=2}^{N_{DFC}} r_k^2 r_{k-1}^2$ as opposed to the amplitude composite DV $\sum_{k=1}^{N_{NCH}}\sqrt{\bar{I}_{p,k}^{Noise^2}+\bar{Q}_{p,k}^{Noise^2}} / \sum_{k=2}^{N_{DFC}}\sqrt{r_k r_{k-1}}$ (where $N_{NCH}$ and $N_{DFC}$ individually are number of noncoherent integration and DFC accumulations) makes no difference in capability of detection because the power/root operation affects the signal and noise simultaneously by the same level in dB, and thus does not change SNR. To facilitate statistical analysis, the following composite DV is used to analyze the performance of the DFC-based detector:

$$T_{Acq}^{DFC}=\sum_{k=2}^{N_{DFC}} z_k^{DFC}=\sum_{k=2}^{N_{DFC}} r_k^2 r_{k-1}^2 \tag{3.29}$$

where $N_{DFC}$ is the number of DFC operations. These performance analysis results are equivalent to those obtained using the composite DV expressed as $\sum_{k=2}^{N_{DFC}} \sqrt{r_k r_{k-1}}$.

By removing the 4th root operation shown in Figure 3-1, a DFC-based power detector is realized. Conditional PDFs for each unit DV $z_k^{DFC}$ in eq. (3.29) are computed by a double integration followed by a limit and partial derivative operations, given as

$$\begin{aligned} p\left(z_k^{DFC}\middle|H_m\right)_{m=0,1} &= \frac{\partial P\left(z_k^{DFC} \le Z_k^{DFC}\middle|H_m\right)_{m=0,1}}{\partial Z_k^{DFC}} \\ &= \frac{\partial}{\partial Z_k^{DFC}} \lim_{\varepsilon->0} \int_{\varepsilon}^{+\infty} p\left(r_k\middle|H_m\right)_{m=0,1} \int_{0}^{Z_k^{DFC}/r_k} p\left(r_{k-1}\middle|H_m\right)_{m=0,1} dr_{k-1} dr_k \end{aligned} \tag{3.30}$$

where the composite PDFs of $r_j$ ( $j = k-1/k$ ) are

$$p\left(r_j\middle|H_1\right)_{j=k-1,k} = e^{-\left(\frac{\breve{A}_j^2}{2}\right)} e^{-\left(\frac{r_j^2}{2}\right)} I_0\left(\breve{A}_j r_j\right) r_j \Big|_{j=k-1,k} \tag{3.31}$$

$$p\left(r_j\middle|H_0\right)_{j=k-1,k} = r_j e^{-\left(\frac{r_j^2}{2}\right)} \Big|_{j=k-1,k} \tag{3.32}$$

Analysis demonstrates that conditional PDFs for unit DV $\left(z_k^{DFC}\right)$ cannot be analytically formed because (1) the upper limit of the inner integration is not infinity; (2) the integration of zero-order modified Bessel function with that of the first kind cannot be expressed in closed form. Even if the pair of conditional PDFs of the unit DV can be expressed in closed-form, the convolution, to compute the conditional PDFs of the composite DV, re-

sult in an $[N_{DFC}-1]$-fold integration. $N_{DFC}$ for weak signal acquisition is several tens, which greatly challenges the feasibility of numerical solution for the multiple integrations.

Due to the above-mentioned complexity, curve fitting is used to approximate the distribution of the DFC composite DV produced by Monte Carlo simulation. Implementation and evaluation of the approximation is divided into two steps: first, from a statistical sense, the expectation and variance of the conditional PDFs for composite DV described in eq. (3.29) are derived; second, the quality of approximation is verified. Then based on the expectation and variance, four distributions are tested — the normal, chi-squared, Rayleigh, and Rician distribution. Results show that the overlap ratio, the percentage of overlapped area between simulated PDF and the ideal PDF, is beyond 90% for the normal approximation, while it is only 78% for the second best-performing option, the Rician distribution. This agrees with the central limit theorem which states that if a sufficient number of summed RVs have a finite variance then the sum will be approximately normally distributed.

Applying eqs. (3.1)-(3.4) to a single unit DV in eq. (3.29), as well as assuming there is no power/amplitude degradation due to code and carrier misalignment, the units within composite DV of eq. (3.29) under conditions $H_0$ and $H_1$ respectively are

$$z_k^{DFC} = \prod_{j=k-1}^{k} \left( \overline{n}_{p,I,j}^{Noise^2} + \overline{n}_{p,Q,j}^{Noise^2} \right) \tag{3.33}$$

$$z_k^{DFC}\left|H_1 = \prod_{j=k-1}^{k}\left[\breve{A}_j^2 + 2\breve{A}_j\left(\bar{n}_{p,I,j}^{Noise}\ cos\,\bar{\varphi}_j + \bar{n}_{p,Q,j}^{Noise}\ sin\,\bar{\varphi}_j\right) + \left(\bar{n}_{p,I,j}^{Noise^2} + \bar{n}_{p,Q,j}^{Noise^2}\right)\right]\right. \quad (3.34)$$

The noise terms $\bar{n}_{p,I,j}^{Noise}$ and $\bar{n}_{p,Q,j}^{Noise}$ ( $j = k-1/k$ ) in eqs. (3.33) and (3.34) are assumed to be i.i.d WGN with unit variance as described in eqs. (3.1) and (3.2). Based on computations, the conditional expectation and variance of RVs given in eqs. (3.33) and (3.34) are

$$E\left(z_k^{DFC}\left|H_0\right.\right) = 4 \quad (3.35)$$

$$Var\left(z_k^{DFC}\left|H_0\right.\right) = 48 \quad (3.36)$$

$$E\left(z_k^{DFC}\left|H_1\right.\right) = \prod_{j=k-1}^{k}\breve{A}_j^2 + 2\sum_{j=k-1}^{k}\breve{A}_j^2 + 4 \quad (3.37)$$

$$\begin{aligned} Var\left(z_k^{DFC}\left|H_1\right.\right) = {} & 4\breve{A}_k^4\left(\breve{A}_{k-1}^2 + 1\right) + 4\breve{A}_k^2\left(\breve{A}_{k-1}^2 + 4\right)^2 + \\ & 4\left(\breve{A}_{k-1}^4 + 16\breve{A}_{k-1}^2 + 12\right) \end{aligned} \quad (3.38)$$

Therefore, the variance and expectation of the composite DV $T_{Acq}^{DFC}$ under conditions $H_0$ and $H_1$ are easily derived as

$$E\left(T_{Acq}^{DFC}\left|H_m\right.\right)\Big|_{m=0,1} = \sum_{k=2}^{N_{DFC}} E\left(z_k^{DFC}\left|H_m\right.\right)\Big|_{m=0,1} \quad (3.39)$$

$$Var\left(T_{Acq}^{DFC}\left|H_m\right.\right)\Big|_{m=0,1} = \sum_{k=2}^{N_{DFC}} Var\left(z_k^{DFC}\left|H_m\right.\right)\Big|_{m=0,1} \quad (3.40)$$

Again, as in the previous description for eqs. (2.10) and (2.11), the amplitude fading due to time and carrier offset misalignment degrades the detection performance because the signal power decays over the processing interval. However both NCH and DFC approaches are influenced simultaneously by almost identical levels of this degradation. Therefore, the performance comparison between the two methods is still valid based on

the assumption $\breve{A}_k = \breve{A}_{k-1} = A$. First- and second-order statistical solutions, given by eqs. (3.39) and (3.40), can determine a specific normal distribution. Eqs. (3.1)-(3.4) in section 3.1.1 can be used to create $\bar{I}_{p,k}^{Noise} / \bar{I}_{p,k-1}^{Noise}$ and $\bar{Q}_{p,k}^{Noise} / \bar{Q}_{p,k-1}^{Noise}$ under null and alternative hypotheses. A set of the sequences are used to evaluate the random characteristics of the unit DV $z_k^{DFC}$. Iteratively accumulating the unit DVs several times, the random characteristics of the composite DV can be quantified. The simulated conditional PDFs are used to examine the quality of normal approximation under three typical post-COH SNR situations: low (-6 dB), moderate (0 dB), and high (10 dB). The best-fit results of the three cases are respectively shown by Figures 3, 4, and 5 in Yu et al. (2006b), with values ranging from 96.39% to 96.74% under null hypothesis and from 94.99% to 96.44% under alternative hypothesis. Figure 3-4 compares the quality of curve fitting for a varying $N_{DFC}$ ranging from 20 to 80. It shows that the overlap area between a normal approximation and simulated distribution varies from 92% to 98%, thus validating the effectiveness of normal fitting to offer a satisfactory reference, even though it is not rigorously accurate.

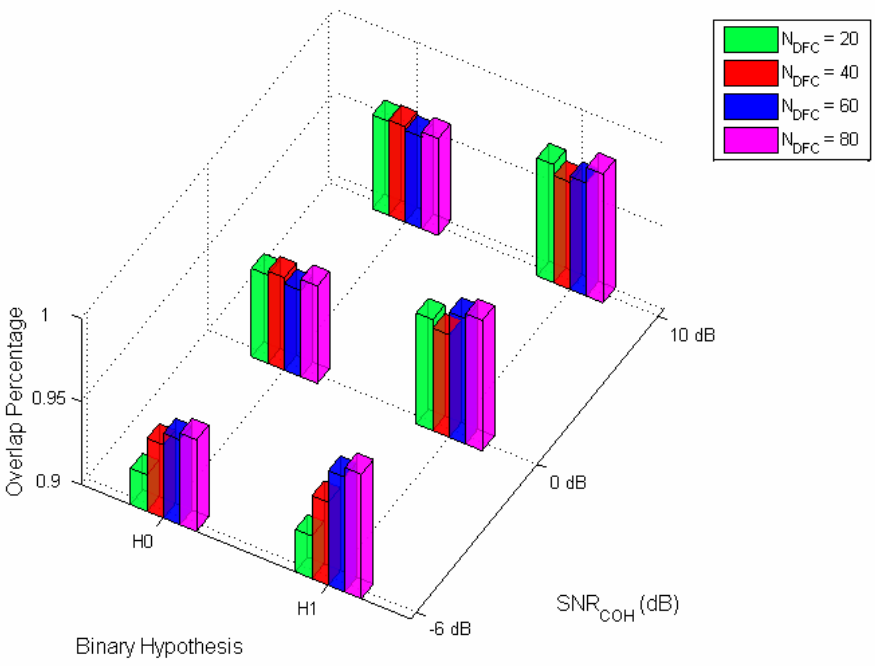


Figure 3-4: Overlap percentage between normal fitting and Monte Carlo based distribution with DFC iterations varying from $N_{DFC} = 20$ to $N_{DFC} = 80$

Figure 2-10 showed the structure of NCH power detector, where $N_{COH}$ and $N_{NCH}$ individually are number of COH integration NCH operations. The composite DVs for this model under hypotheses $H_0$ and $H_1$ are

$$T_{Acq}^{NCH}\left|H_m\right|_{m=0,1} = \sum_{k=1}^{N_{NCH}} z_k^{NCH}\left|H_m\right|_{m=0,1} = \sum_{k=1}^{N_{NCH}} \left(\bar{I}_{p,k}^{Noise^2} + \bar{Q}_{p,k}^{Noise^2}\right)\left|H_m\right|_{m=0,1} \tag{3.41}$$

Again substituting eqs. (3.1)-(3.4) for the corresponding components of composite DV defined by eq. (3.41), and neglecting degradation associated with code and carrier mismatch, the conditional PDFs for NCH conditional DV are derived by Bastide et al. (2006) as

$$T_{Acq}^{NCH}\left|H_0 \sim \chi^2_{2N_{NCH}}\left(\lambda = 0\right)\right., \text{ and} \tag{3.42}$$

$$T_{Acq}^{NCH} \,|\, H_1 \sim \chi^2_{2N_{NCH}} \left( \lambda = \sum_{k=1}^{N_{NCH}} \breve{A}_k^2 \right) \tag{3.43}$$

where $\chi^2_{2N_{NCH}}(\lambda = 0)$ and $\chi^2_{2N_{NCH}}\left(\lambda = \sum_{k=1}^{N_{NCH}} \breve{A}_k^2\right)$ respectively are termed as central and non-central chi-square distributions with $2N_{NCH}$ degrees of freedom.

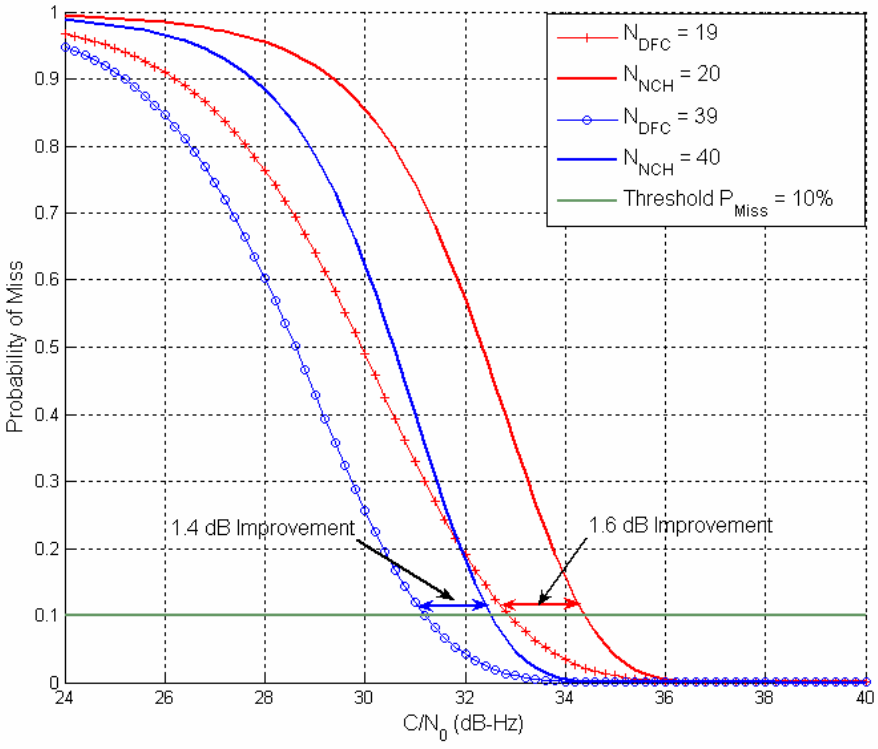


Figure 3-5: Probability of miss (DFC vs. NCH) with $T_{COH} = 1$ ms and $P_{FA} = 0.1\%$, where $N_{NCH} = 20 / 40$

Again due to the reasons presented in the paragraph immediately following eq. (3.40), a perfect timing and carrier alignment is assumed here to simplify the performance evaluation of two detection strategies. The probability of false alarm for all the cases in this thesis is constrained to 0.1%. Solid lines and symbols in Figure 3-5 individually represent

probability of miss of a NCH detector and that of a DFC-based detector, respectively. Given a processing segment, the number of DFC is inherently one less than the number of NCH integrations. To evaluate the performance of a detector, we are mostly concerned about a critical threshold of $C/N_0$. Beyond this threshold, the detector can maintain a sound power of detection, for instance the probability of miss being no greater than 10%. The red double arrow indicator in Figure 3-5 denotes the sensitivity improvement by using the DFC approach. Setting the threshold of the probability of miss to 10%, the DFC method can acquire the signal that is 1.6 dB lower while maintaining identical performance compared to the NCH detector.

When increasing the number of NCH integrations from 20/40 to 60/80, as shown in Figure 3-6, the improvement in terms of sensitivity decreases by 0.4 dB, compared with 20 NCH accumulations, to 1.2 dB. The gain on detection power results from the smaller processing loss of DFC shown in Figure 3-2. The achievable sensitivity of both DFC-based and NCH detectors is tabulated to clarify, in conditions of different COH period and various number of DFC/NCH accumulations, (1) the critical threshold of $C/N_0$ beyond which the specific approach can sustain a desired detection performance, and (2) the sensitivity improvement achieved by adopting the DFC strategy. Table 3-1 is also used to suggest an acquisition strategy for a given $C/N_0$.

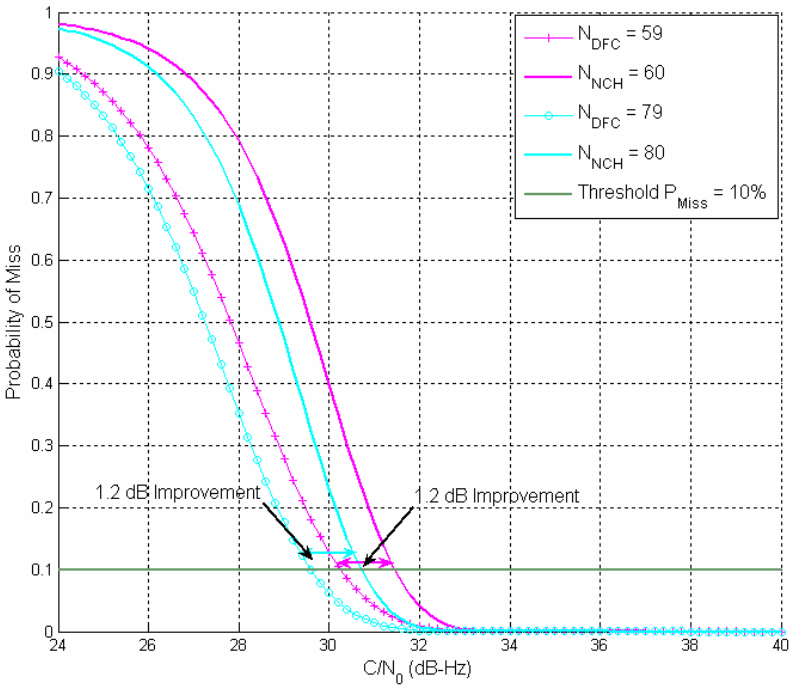


Figure 3-6: Probability of miss (DFC vs. NCH) with $T_{COH} = 1$ ms and $P_{FA} = 0.1\%$, where $N_{NCH} = 60 / 80$

Table 3-1: Acquisition sensitivity comparison between DFC and NCH method with $P_D = 90\%$

| | Coherent Integration Segment | | | | | | | | | | | | | | | |
|---|---|---|---|---|---|---|---|---|---|---|---|---|---|---|---|---|
| | 1 ms | | | | 2 ms | | | | 5 ms | | | | 10 ms | | | |
| Number of NCH/DFC | 20/19 | 40/39 | 60/59 | 80/79 | 20/19 | 40/39 | 60/59 | 80/79 | 20/19 | 40/39 | 60/59 | 80/79 | 20/19 | 40/39 | 60/59 | 80/79 |
| DFC sensitivity | 32.8 | 31.2 | 30.2 | 29.6 | 29.8 | 28.2 | 27.2 | 26.6 | 25.8 | 24.2 | 23.2 | 22.6 | 22.8 | 21.2 | 20.2 | 19.6 |
| NCH sensitivity (dB-Hz) | 34.4 | 32.6 | 31.4 | 30.8 | 31.2 | 29.6 | 28.4 | 27.8 | 27.2 | 25.6 | 24.4 | 23.8 | 24.2 | 22.6 | 21.4 | 20.8 |
| Sensitivity Improvement (dB) | 1.6 | 1.4 | 1.2 | 1.2 | 1.4 | 1.4 | 1.2 | 1.2 | 1.4 | 1.4 | 1.2 | 1.2 | 1.4 | 1.4 | 1.2 | 1.2 |

As shown in Figure 3-7 to Figure 3-9, the use of DFC method, for each scenario (defined by a specific pair of COH duration and number of DFC/NCH accumulations), consistently reduces the probability of miss by about 3 to 4 times around the threshold $C/N_0$ region. As per the acquisition strategies defined by the COH interval and number of nonlinear operations , Table 3-1 lists the lowest signal levels that the detectors can acquire with a success rate of 90%.

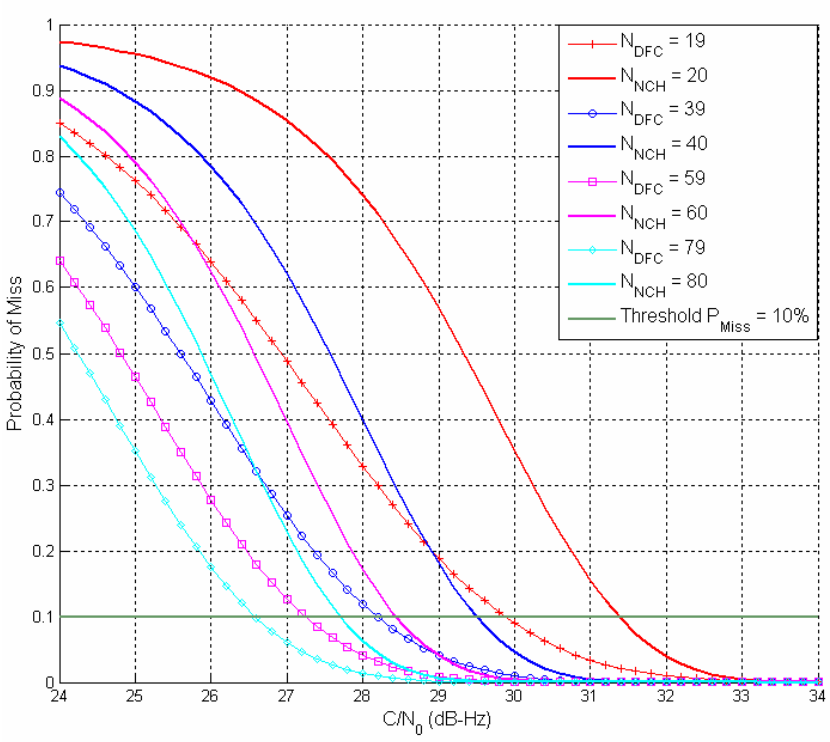


Figure 3-7: Probability of miss (DFC vs. NCH) with $T_{COH} = 2$ ms and $P_{FA} = 0.1\%$, where $N_{NCH} = 20 / 40 / 60 / 80$

By examining Table 3-1, several conclusions can be drawn: (1) by doubling the noncoherent accumulations, the sensitivity can be improved by approximately 1.6 dB for both methods, (2) extension of the coherent integrations is effective to improve the sensitivity, and (3) the sensitivity improvement using the DFC slightly degrades by increasing the number of NCH/DFC operations.

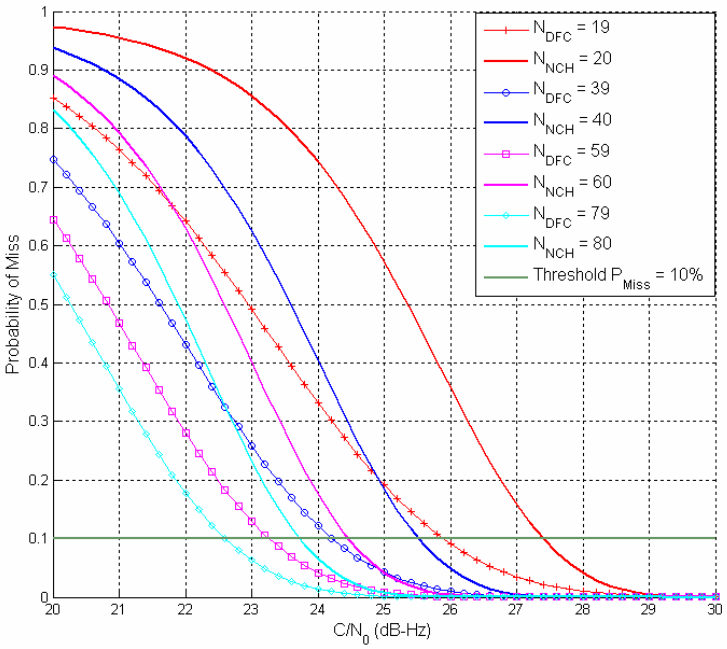


Figure 3-8: Probability of miss (DFC vs. NCH) with $T_{COH} = 5$ ms and $P_{FA} = 0.1\%$, where $N_{NCH} = 20 / 40 / 60 / 80$

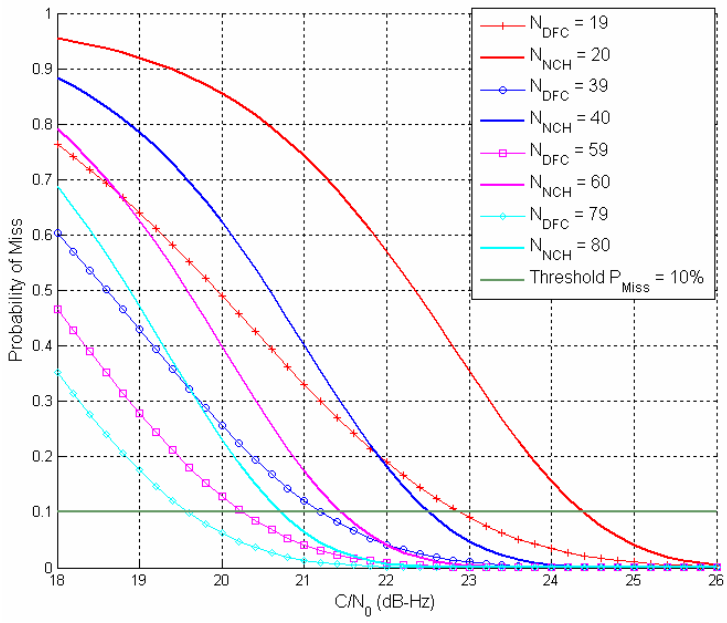


Figure 3-9: Probability of miss (DFC vs. NCH) with $T_{COH} = 10$ ms and $P_{FA} = 0.1\%$, where $N_{NCH} = 20 / 40 / 60 / 80$

The above statistical benchmark is essential for optimizing the detection threshold and thus ensuring satisfactory performance of a receiver.

## 3.2 Numerical Evaluation for Weak Signal Acquisition

To evaluate the sensitivity improvement resulting from the DFC approach compared with the conventional NCH method, the hardware system is set up as shown in Figure 3-10. A Spirent GSS6560 Multi-Channel GPS/SBAS Simulator System is used to generate L1 RF signals for one satellite at L-band. With the simulator, the signal transmission power can be predefined accurately once the simulator is calibrated. The transmitted signal is received by a NovAtel EURO3M receiver via a RF cable. An ALTERA MAXII FPGA transforms the serial digital sequence from the A/D unit of NovAtel EURO3M into parallel format. The parallel binary codes are collected by an NI card inside the computer.

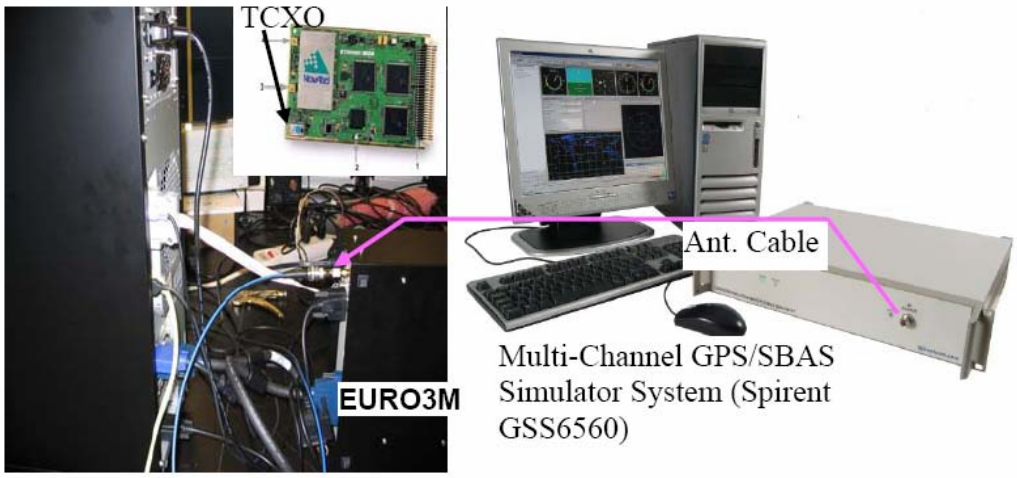


Figure 3-10: System setup to evaluate the DFC acquisition approach

The IF digital samples are then fed into a software receiver to acquire the satellite signal. To avoid possible bit transition occurring in a COH interval, the COH accumulation pe-

riod is no longer than 10 ms in the absence of prior knowledge of bit boundaries. COH accumulation is desired to be as long as possible in weak signal acquisition. At least one of the 10 ms segments immediate adjacent to each other is absent from the data bit transition. As shown by Figure 3-11, the data segment is divided into an odd set and an even set. Obviously, the possible bit transition only happens in one set and thus no transition occurs in the other. In this case, the segments $2k-1$ and $2k+1$ are adjacent, as are segments $2k-2$ and $2k$.

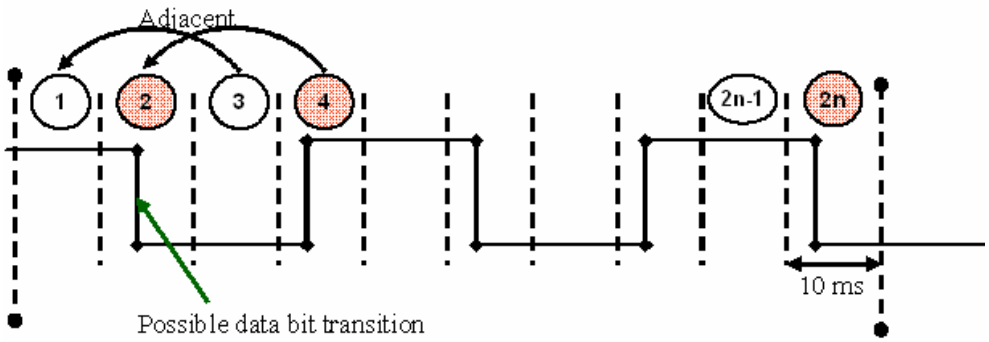


Figure 3-11: Half period (10 ms) COH accumulation scheme

The $C/N_0$ of the input signal is set to 24 dB-Hz, 19 dB lower than nominal open-sky signal strength. For a 10 ms COH interval, a 1.2 second data set consists of two 60 COH segments and one of them does not contain data bit transition. Figure 3-12 demonstrates that the DFC provides a 1.2 dB SNR improvement compared with the conventional NCH approach. The Z axis represents the resultant $T_{Acq}^{NCH}/T_{Acq}^{DFC}$. This result is consistent with theoretical predictions shown in Table 3-1. However, in most real cases, the improvement cannot meet the ideal prediction because the cross-correlation interference is not negligible. The cross-correlation is neglected in conducting the previous theoretical quantifica-

tion. The cross-correlation peak, unlike the additive noise, reveals a deterministic characteristic at a certain code and carrier phase offsets. Therefore, besides the increase in SNR, the cross-correlation interference is strengthened by DFC operation simultaneously, thus degrading the improvement achieved by DFC.

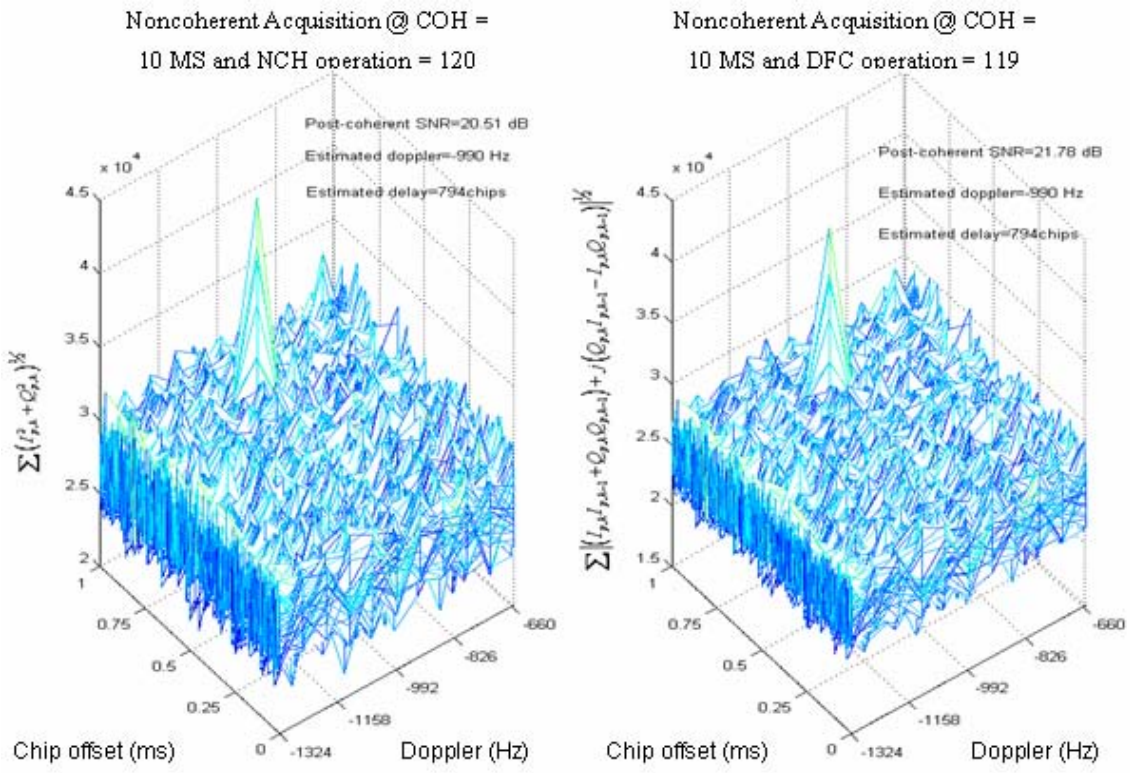


Figure 3-12: Sensitivity improvement using DFC approach

# Chapter 4 Carrier Tracking Enhancement

The signal simulator described in Chapter 2 is used to create signal samples. The errors resulting from the satellite clock, ephemeris, receiver noise are taken into account. The implementation loss induced by front-end filtering and quantization are also considered. Besides those errors, Dong's simulator (2003) is enhanced by accommodating the receiver OSC's PHN and ionospheric scintillation. The models for the two errors are respectively described in section 2.4 and section 2.5.

In this chapter, the perturbed signal samples are fed into the software receiver in which both the CBPLLs and KF -based PLLs are realized. The RMS carrier tracking error and probability of cycle slips are used to evaluate tracking performance. Section 4.1 examines the performance of a CBPLL with different configurations, including four types of discriminators and three types of loop filter designs. To further enhance the tracking capability under low SNR conditions, Section 4.2 derive the implementation of the KF-based PLLs and investigate the tracking performance under identical scenarios as those for the CBPLLs. The results demonstrate that (1) KF-based PLLs improve the sensitivity by 7 dB and 4 dB, respectively, in the presence of strong and weak ionospheric scintillation. The decision-directed loop, compared with other types of CBPLLs, reveal a 2 dB sensitivity improvement. The loop filter parameters of Stephens & Thormas (1995) for CBPLLs shows a 1-2 dB sensitivity improvement as the popluar settings by Kaplan (1996) or Parkinson (1996).

## 4.1 Optimization of a Constant Bandwidth PLL

In Weinberg & Liu (1974), the phase tracking error is analyzed for digital PLL versus $C/N_0$ . This quantification is realized by investigating the steady-state phase error probability density (Weinberg & Liu 1974), which satisfies the Chapman-Kolmogorov (C-K) equations. The C-K approach is generally adopted to evaluate the first- and second-order digital PLL; however it is harder to evaluate the third-order PLL due to the complexity in solving three partial differential equations (PDEs). The history of the digital PLL and all the substantial results are well presented by Lindsey & Chie (1981). This thesis examines the measurement bias resulting from the discriminator's on-threshold behaviour and consolidates all the errors into linear system analysis.

The effects of ionospheric scintillation and OSC-induced PHN result in both code and carrier tracking errors. This chapter concentrates on the carrier tracking performance, which is determined by both the intensity of the disturbances and the structure of the carrier tracking estimator. In this section, the Costas loop is first linearized by modeling the signal in this loop. The carrier tracking error is then examined in the scope of linear system theory. Finally, the theoretical results are justified by numerical experiment.

### 4.1.1 Behavior of a Constant Bandwidth PLL based on Linear Approximation

Figure 4-1 (Humphreys et al. 2005, Skone et al. 2005) shows the functional diagram of a GPS receiver's PLL. The received signal modeled by eq. (2.46) is filtered by the front-end filter, whose effects are mentioned in section 2.1.3. The carrier of the digitized

samples are wiped off, where the code correlation unit is not shown Figure 4-1. The baseband samples pass through the Accum & Dump filter to achieve the COH correlations expressed by eqs. (2.10) and (2.11), in which only the results from the prompt correlators are used for carrier tracking purposes. Due to the presence of various kinds of perturbations, the average phase misalignment over an accumulation interval $\bar{\varphi}_k$ accommodates the phase fluctuations led by the oscillator's imperfection and the ionosphere scintillation activity. In addition, the additive thermal noises $n_{p,I,k}$ and $n_{p,Q,k}$ degrade accuracy in measuring $\bar{\varphi}_k$ based on the prompt COH correlations. The noises are assumed to be i.i.d WGN whose statistical property is quantified in the description for eqs. (2.10) and (2.11).

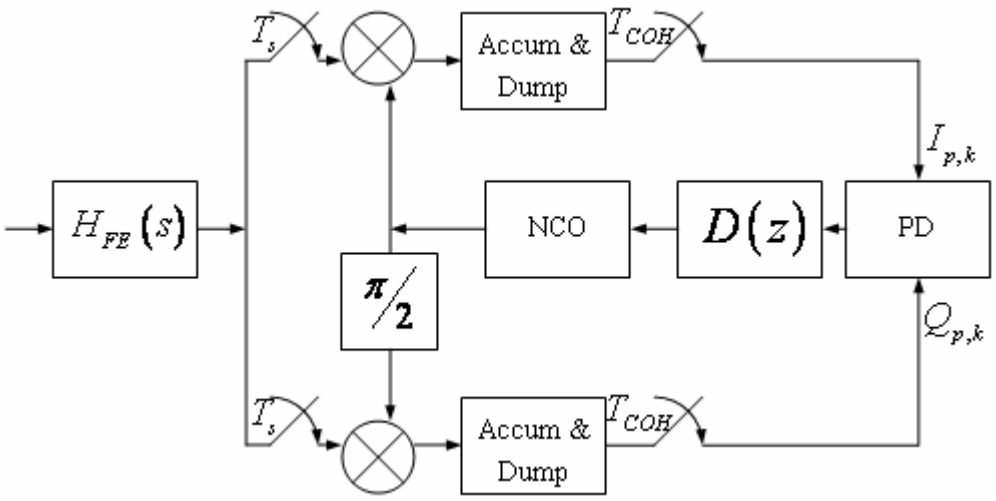


Figure 4-1: Functional diagram of a Costas loop

The COH correlations from the I and Q correlators are then used by the discriminator (PD) to measure the phase misalignment. Four types of discriminators appropriate for the Costas loop are discussed in this thesis: conventional Costas (CC), decision-directed (DD), ATAN, and DD-ATAN2. To use the CC and DD discriminators, the COH correla-

tions at I and Q branches should be normalized based on the estimated signal amplitude. The resultant normalized correlations based on the signal amplitude are modeled by eqs. (2.15) and (2.16). The ATAN and DD-ATAN2 discriminators, which include the normalization automatically, are easier to implement in a software receiver.

The discriminator can be regarded a function of $\left(\bar{I}_{p,k}^{Sig}, \bar{Q}_{p,k}^{Sig}\right)$, which measures the phase mismatch $\bar{\varphi}_k$. Due to the sine characteristic of $\bar{\varphi}_k$, measurements from the CC and DD discriminators well reflect actual phase conditioning for tight phase tracking, i.e. $\left|\bar{\varphi}_k\right| << 1$. The ATAN discriminator forms the maximum likelihood estimator (MLE) of $\bar{\varphi}_k$ which, in the noise-free case, perfectly measures the phase. DD-ATAN2 is a mix of DD and ATAN; therefore, it inherits the properties of both discriminators. The ATAN/DD-ATAN2 can directly use $I_{p,k}$ and $Q_{p,k}$ because automatic normalization is implied in both operators.

Table 4-1 establishes the relationship between phase misalignment and the measurement by the discriminators. From eqs. (2.10) and (2.15), the sign of $I_{p,k} / \bar{I}_{p,k}^{Sig}$, in phase lock and absent from the noise, perfectly reflects the data bit. The noise, however, is definitely present in I and Q, thus leading to (1) $sign\left(\tilde{I}_{p,k}\right) \neq d_m$, termed BER in a statistical sense, and (2) the measure by the discriminator is severely biased from the actual phase. This deviation greatly exacerbates the on-threshold behaviour of a PLL, causing a larger phase tracking error or higher probability to diverge than predictions based on the linear system analysis. Compared with the discriminators listed in Kaplan (1996), two adjustments are employed here:

(1) $\tilde{I}_{p,k}$, the accumulated in-phase COH correlation, replaces the $I_{p,k}$ to lower BER, thus making the measurement more accurate; where

$$\tilde{I}_{p,k} = \begin{cases} I_{p,k} & \text{if } I_{p,k} \text{ is the start of a data bit} \\ \tilde{I}_{p,k-1} + I_{p,k} & \text{if } I_{p,k} \text{isn't the start of a data bit} \end{cases} \tag{4.1}$$

(2) DD-ATAN2, unlike ATAN2 (Kaplan 1996), is suitable for a Costas loop as it is insensitive to the $\pi$ reversal resulting from the BPSK modulation.

Table 4-1: The characteristics of the discriminators

| Type | $g\left(\bar{I}_{p,k}^{Sig}, \bar{Q}_{p,k}^{Sig}\right)$ | $f\left(\bar{\varphi}_k\right)$ without noise |
|---|---|---|
| CC | $\bar{I}_{p,k}^{Sig} \cdot \bar{Q}_{p,k}^{Sig}$ | $\frac{1}{2} sin\left(2\bar{\varphi}_k\right)$ |
| DD | $sign\left(\tilde{I}_{p,k}\right) \cdot \bar{Q}_{p,k}^{Sig}$ | $\begin{cases} -sin\bar{\varphi}_k & \left\|\bar{\varphi}_k\right\| \in [\pi/2, \pi] \\ sin\bar{\varphi}_k & \left\|\bar{\varphi}_k\right\| \in [0, \pi/2] \end{cases}$ |
| ATAN | $a\tan\left(\bar{Q}_{p,k}^{Sig} / \bar{I}_{p,k}^{Sig}\right)$ | $\begin{cases} \pi + \bar{\varphi}_k & \bar{\varphi}_k \in [-\pi, -\pi/2] \\ \bar{\varphi}_k & \bar{\varphi}_k \in [-\pi/2, \pi/2] \\ -\pi + \bar{\varphi}_k & \bar{\varphi}_k \in [\pi/2 \ , \ \pi] \end{cases}$ |
| DD-ATAN2 | $a\tan 2\left(sign\left(\tilde{I}_{p,k}\right) \cdot \bar{Q}_{p,k}^{Sig}, sign\left(\tilde{I}_{p,k}\right) \cdot \bar{I}_{p,k}^{Sig}\right)$ | The same as ATAN |

The improvement in lowering the mean BER and the response of the discriminators are thoroughly examined in the following analysis.

Since the response of the DD and DD-ATAN2 depends on the BER, the BER improvement achieved by using $\tilde{I}_{p,k}$ is analyzed from a statistical sense.

Taking the noise property modeled in the description of eq. (2.18), and denoting

$$L_{COH} = T_b / T_{COH} \tag{4.2}$$

where $T_b$ is the period of the data bit equal to 20 ms, the BER up to the $lth$ COH segment within one data bit becomes

$$P\left(sign\left(\tilde{I}_{p,k}\right) \neq d_{m,k} \middle| \bar{\varphi}_k\right) = Q\left(\cos\bar{\varphi}_k \sqrt{2SNR_{COH} l}\ \right) \tag{4.3}$$

where

$SNR_{COH}$ is SNR after COH accumulation (post-COH SNR), equal to $\frac{CT_{COH}}{N_0}$,

$Q(\cdot)$ is Q function, which represents the right tail of the zero-mean Gaussian PDF with a unit variance.

This equation infers that the BER decreases over the accumulation within one data bit. Here, every post-COH SNR within one-bit accumulation is assumed to be a constant $SNR_{COH}$; however, such an assumption does not lose generality because $SNR_{COH} l$ can be replaced by $\sum_{k=1}^{l} SNR_{COH,k}$, where $SNR_{COH,k}$ is post-COH SNR for each COH accumulation within a data bit. Obviously, the increased SNR lowers the BER when the accumulation propagates within a data bit. To measure the BER improvement after the adjustment, mean BER (MBER) is quantified by

$$MBER = \frac{1}{L_{COH}} \sum_{l=1}^{L_{COH}} Q\left(\cos\bar{\varphi}_k \sqrt{2SNR_{COH} l}\ \right) \tag{4.4}$$

Figure 4-2 illustrates the MBER improvement using $\tilde{I}_{p,k}$, as opposed to $\bar{I}_{p,k}^{Sig} / I_{p,k}$ in Kaplan (1996), to estimate the sign of data bit. $T_{COH}$ is always chosen to be a factor of $T_b$. The MBER, in the $C/N_0$ region 17 to 25 dB lower than the nominal level, has deceased by 5 to 10 times for a 1 ms COH strategy. The improvement decays with the extension of the COH segment and attenuates to zero when $T_{COH} = T_b$.

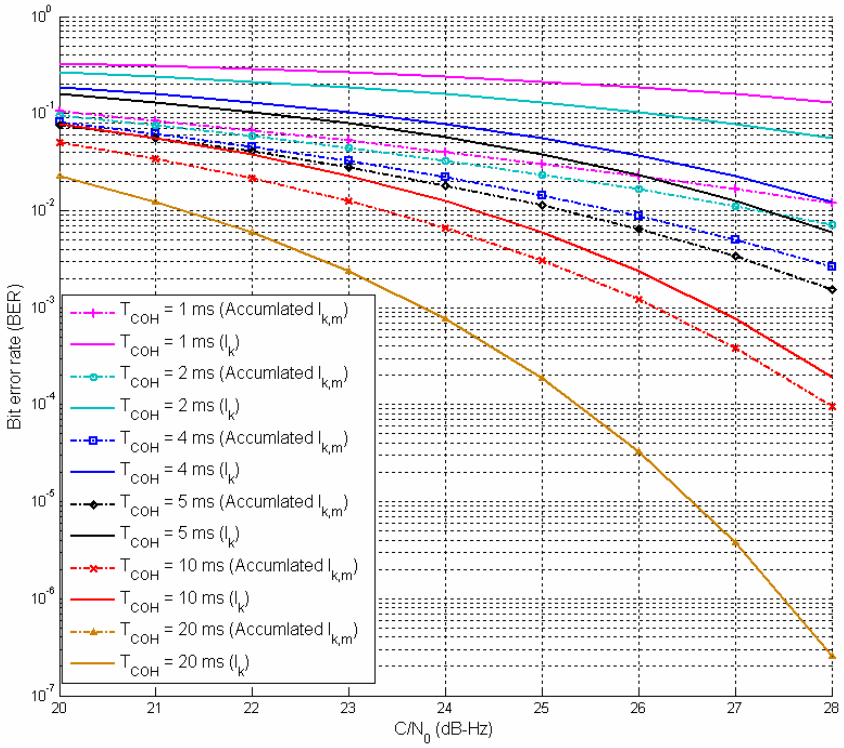


Figure 4-2: MBER improvement by using $\tilde{I}_{p,k}$

Due to the random quality of $\bar{I}_{p,k}^{Sig}$ and $\bar{Q}_{p,k}^{Sig}$, the output $g\left(\bar{I}_{p,k}^{Sig}, \bar{Q}_{p,k}^{Sig}\right)$ by the discriminator is in nature a random variable; consequently, the response of the discriminator is defined from a statistical perspective as

$$E\left[ g\left(\bar{I}_{p,k}^{Sig}, \bar{Q}_{p,k}^{Sig}\right)\right] = E\left[ f\left(\bar{\varphi}_k\right) \middle| \bar{\varphi}_k \right] \tag{4.5}$$

which is associated with the conditional PDF (CPDF) of

$$p\left[ f\left(\bar{\varphi}_k\right) \middle| \bar{\varphi}_k \right] \tag{4.6}$$

To facilitate the analysis of discriminators' response, the geometric representation for eqs. (2.15) and (2.16), shown by Figure 4-3, is introduced. In this figure, it is assumed that the normalized accumulations consist of a noise component whose statistics are described by eq. (2.18).

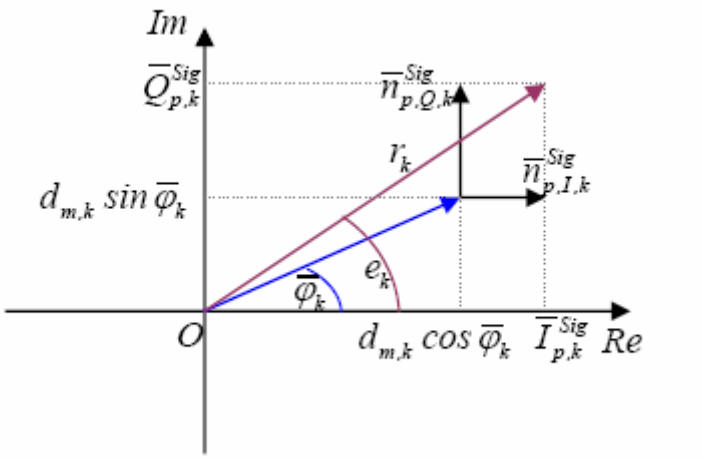


Figure 4-3: Geometric signal representation

Fortunately, the response of CC and DD PDs is relatively easier to derive without the necessity to compute the conditional PDF in eq. (4.6). As a result, the response of CC and DD discriminators is examined first.

$$\begin{aligned} E\left[ f_{CC}\left(\bar{\varphi}_k\right)\right] &= E\left(\bar{I}_{p,k}^{Sig}\cdot\bar{Q}_{p,k}^{Sig}\right) \\ &= E\left(\frac{1}{2}\sin\left(2\bar{\varphi}_k\right)\right) + E\left(d_{m,k}\cos\bar{\varphi}_k\,\bar{n}_{p,Q,k}^{Sig} + d_{m,k}\sin\bar{\varphi}_k\,\bar{n}_{p,I,k}^{Sig} + \bar{n}_{p,I,k}^{Sig}\bar{n}_{p,Q,k}^{Sig}\right) \\ &= \frac{1}{2}\sin\left(2\bar{\varphi}_k\right) \end{aligned} \tag{4.7}$$

$$
\begin{aligned}
E\left[ f_{DD}\left(\bar{\varphi}_k\right)\right] &= E\left(sign\left(\tilde{I}_{p,k}\right)\cdot \bar{Q}_{p,k}^{Sig}\right) \\
&= sign\left(\tilde{I}_{p,k}\right) E\left(d_{m,k}\, sin\,\bar{\varphi}_k + \bar{n}_{p,Q,k}^{Sig}\right) \\
&= \left[ MBCR\middle|\bar{\varphi}_k\right]\cdot sin\,\bar{\varphi}_k + \left(1-\left[ MBCR\middle|\bar{\varphi}_k\right]\right)\left[-sin\,\bar{\varphi}_k\right] \\
&= \left(2\left[ MBCR\middle|\bar{\varphi}_k\right]-1\right)\cdot sin\,\bar{\varphi}_k
\end{aligned}
\tag{4.8}
$$

where MBCR is the abbreviation of mean bit correction rate, related to the MBER by

$$MBCR=1-MBER \tag{4.9}$$

To determine response of ATAN and DD-ATAN2 phase detectors, the complexity of the conditional PDF is included. Figure 4-3 demonstrates that the measurement by ATAN phase detector is $e_k = f\left(\bar{\varphi}_k\right)$, which is not equal to $\bar{\varphi}_k$; this bias originates from the noise perturbations at I and Q. The conditional PDF can be achieved by the following steps:

(1) $\bar{I}_{p,k}^{Sig}$ and $\bar{Q}_{p,k}^{Sig}$ forms a joint Gaussian distribution in the Cartesian coordinates.

$$
\begin{aligned}
&p\left(\bar{I}_{p,k}^{Sig}\,,\,\bar{Q}_{p,k}^{Sig}\middle|\bar{\varphi}_k\right) \\
&\quad = \frac{1}{2\pi\sigma_{\bar{n}}^2}\cdot exp\left[-\frac{1}{2\sigma_{\bar{n}}^2}\left(\left(\bar{I}_{p,k}^{Sig}-d_{m,k}\,cos\,\bar{\varphi}_k\right)^2+\left(\bar{Q}_{p,k}^{Sig}-d_{m,k}\,sin\,\bar{\varphi}_k\right)^2\right)\right]
\end{aligned}
\tag{4.10}
$$

where

$\sigma_{\bar{n}}^2 = \dfrac{N_0}{2CT_{COH}} = \dfrac{1}{2SNR_{COH}}$ is normalized noise power as in eq. (2.18).

(2) Transform the joint PDF into pole coordinates as $p\left(r_k\,,\,e_k\middle|\bar{\varphi}_k\right)$ by

$$
\begin{aligned}
\bar{I}_{p,k}^{Sig} &= d_{m,k} r_k\, cos\, e_k \\
\bar{Q}_{p,k}^{Sig} &= d_{m,k} r_k\, sin\, e_k
\end{aligned}
\tag{4.11}
$$

(3) Then integrate $r_k$ over $\left[0,+\infty\right)$, to achieve

$$p\left(e_k\middle|\bar{\varphi}_k\right)=\int_0^{+\infty} p\left(r_k\ ,e_k\middle|\bar{\varphi}_k\right)r_k dr_k \tag{4.12}$$

which is the conditional PDF necessary to evaluate the response of ATAN and DD-ATAN2 discriminators. The resultant conditional PDF is given by

$$\begin{aligned} p\left(e_k\middle|\bar{\varphi}_k\right) &= \frac{1}{2\pi}exp\left(-SNR_{COH}\right)+\sqrt{\frac{SNR_{COH}}{\pi}}\cos\left(e_k-\bar{\varphi}_k\right) \\ &\cdot exp\left(-SNR_{COH}\ sin^2\left(e_k-\bar{\varphi}_k\right)\right)\cdot Q\left(-\sqrt{2SNR_{COH}}\cos\left(e_k-\bar{\varphi}_k\right)\right) \end{aligned} \tag{4.13}$$

The detailed derivation of eq. (4.13) can be found in Yu et al. (2006b).

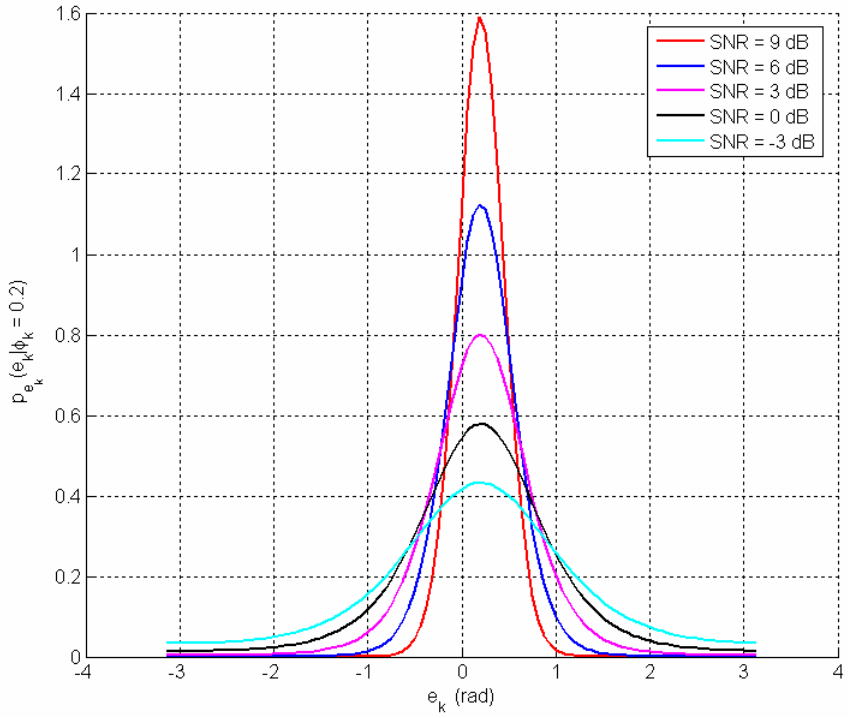


Figure 4-4: Conditional PDF of $p\left(e_k\middle|\bar{\varphi}_k\right)$ for ATAN discriminator

Figure 4-4: depicts the conditional PDF in form of eq. (4.13). This conditional PDF repeats itself with a period of $2\pi$; therefore the expectation is measured within the principal interval, i.e. $e_k\in\left[-\pi,\pi\right]$. The peak probability is located where $e_k=\bar{\varphi}_k$. The pattern of this conditional PDF flattens out with the decrease of post-COH SNR, denoted by

$SNR_{COH}$. Using this conditional PDF, we can quantify the response of the ATAN and DD-ATAN2.

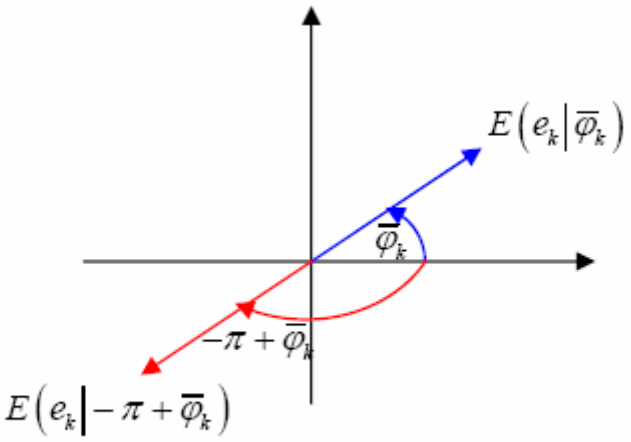


Figure 4-5: Vector analysis of response for DD-ATAN2 discriminator in the presence of noise

Since DD-ATAN2 inherits the characteristics of both DD and ATAN discriminators, the response is associated with MBCR and conditional PDF by eq. (4.13). Assume the phase to be measured is $\bar{\varphi}_k$, the blue vector in Figure 4-5. On one hand, $E\left(e_k\middle|\bar{\varphi}_k\right)$ is the ATAN's measurement on $\bar{\varphi}_k$ in the presence of noise, provided that the bit sign is correctly decided; alternatively, if the bit sign is determined incorrectly, a resultant $\pi$ reversal on phase $-\pi+\bar{\varphi}_k$ causes the red vector to overlap with the blue one in Figure 4-5, indicating $E\left(e_k\middle|-\pi+\bar{\varphi}_k\right)$ is also a measurement of ATAN discriminator on $\bar{\varphi}_k$. The above analysis is mathematically reflected by eq. (4.14), the response of the DD-ATAN2 discriminator:

$$E\left(f_{DD-ATAN2}\left(\bar{\varphi}_k\right)\right) = \begin{cases} \left[MBCR\middle|\bar{\varphi}_k\right]\cdot E\left(e_k\middle|\bar{\varphi}_k\right)+\left[MBER\middle|-\pi+\bar{\varphi}_k\right]\cdot E\left(e_k\middle|-\pi+\bar{\varphi}_k\right) & \left(\bar{\varphi}_k \geq 0\right) \\ \left[MBCR\middle|\bar{\varphi}_k\right]\cdot E\left(e_k\middle|\bar{\varphi}_k\right)+\left[MBER\middle|\pi-\bar{\varphi}_k\right]\cdot E\left(e_k\middle|\pi-\bar{\varphi}_k\right) & \left(\bar{\varphi}_k < 0\right) \end{cases} \quad (4.14)$$

where $e_k \in [-\pi,\pi]$ is used to calculate all the expectations in this equation.

The ATAN discriminator is only associated with the conditional PDF expressed by eq. (4.13), and takes the form of

$$E\left(f_{ATAN}\left(\bar{\varphi}_k\right)\right) = \int_{-\pi/2}^{\pi/2} e_k\, p\left(e_k\middle|\bar{\varphi}_k\right) de_k + \int_{-\pi}^{-\pi/2} \left(e_k+\pi\right) p\left(e_k\middle|\bar{\varphi}_k\right) de_k + \int_{\pi/2}^{\pi} \left(e_k-\pi\right) p\left(e_k\middle|\bar{\varphi}_k\right) de_k \quad (4.15)$$

The measurement from the ATAN discriminator is within $[-\pi/2,\pi/2]$; therefore, the last two integrations on the right side of eq. (4.15) account for the $\pi$ phase reversal caused by the ATAN operation.

Eqs. (4.7), (4.8), (4.14), and (4.15) are derived to analytically evaluate the discriminators' performance in the presence of noise. The performance is defined as the capability of a discriminator to correctly measure the actual phase. Eq (4.7) explicitly shows that performance of the CC discriminator is affected by the sine characteristic, which causes a large bias if $\left|2\bar{\varphi}_k\right| << 1$ is violated. The quality of DD, ATAN, and DD-ATAN2 discriminators is either associated with post-COH SNR, or a periodic conditional PDF, or both.

Figure 4-6 illustrates the response of the DD discriminator in various post-COH SNR conditions. In this plot, the simulation results match well with the theoretical predictions using eq. (4.8).

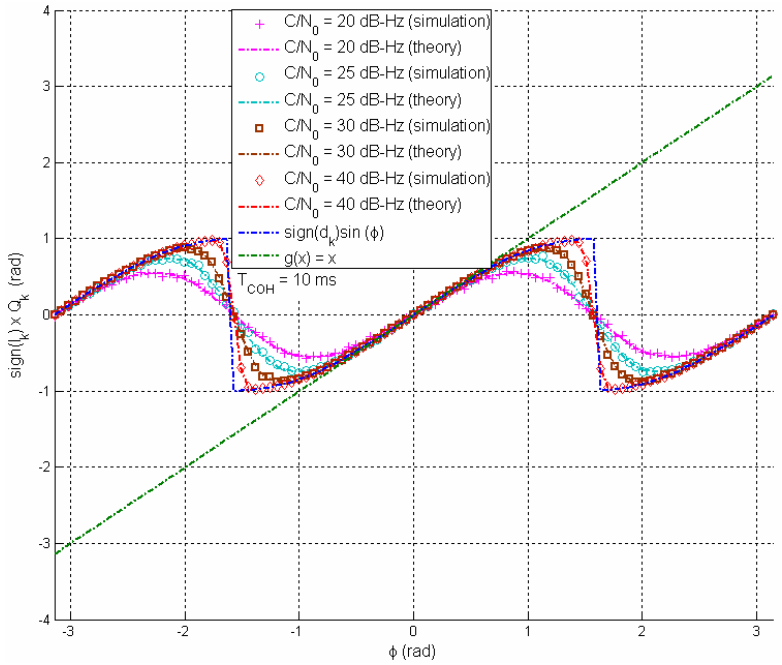


Figure 4-6: Response of the DD discriminator in different SNR conditions

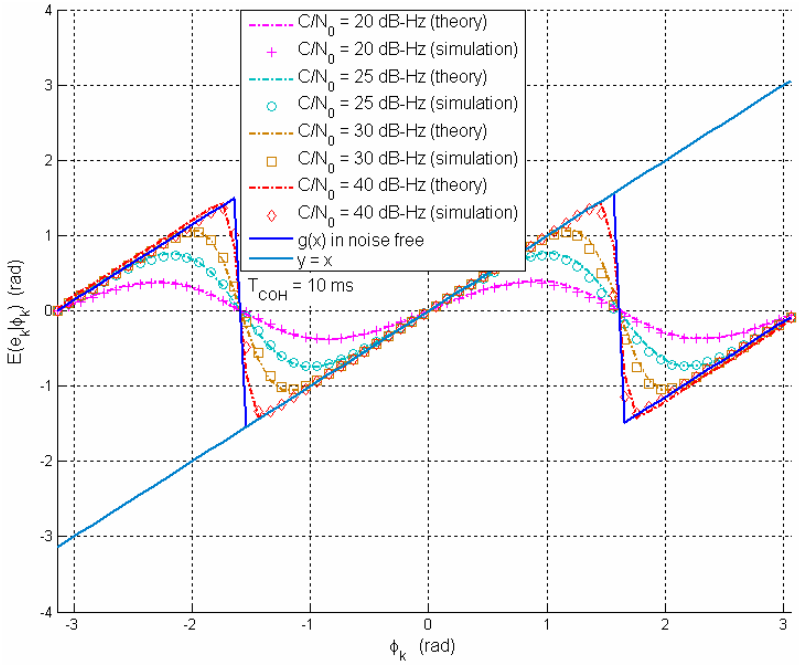


Figure 4-7: Response of the ATAN discriminator in different SNR conditions

The bit sign leads to a $\pi$ phase shift, as opposed to a sine curve, for the DD discriminator in the region of $|\overline{\varphi}_k| > \pi/2$. Additionally, the expectation, $E(e_k|\overline{\varphi}_k)$, exhibits discon-

tinuities at $\bar{\varphi}_k = \pm \pi/2$ when free from the noise disturbance, because the bit sign is ambiguous for $\left(\tilde{I}_{p,k} = 0 \middle| \bar{\varphi}_k = \pm \pi/2\right)$. In the presence of noise, the MBER is the same as the MBCR at $\bar{\varphi}_k = \pm \pi/2$, leading to a zero expectation value. The amplitude of the sine curve decays with decreasing SNR, such that the overlap segment with $y = x$ shortens.

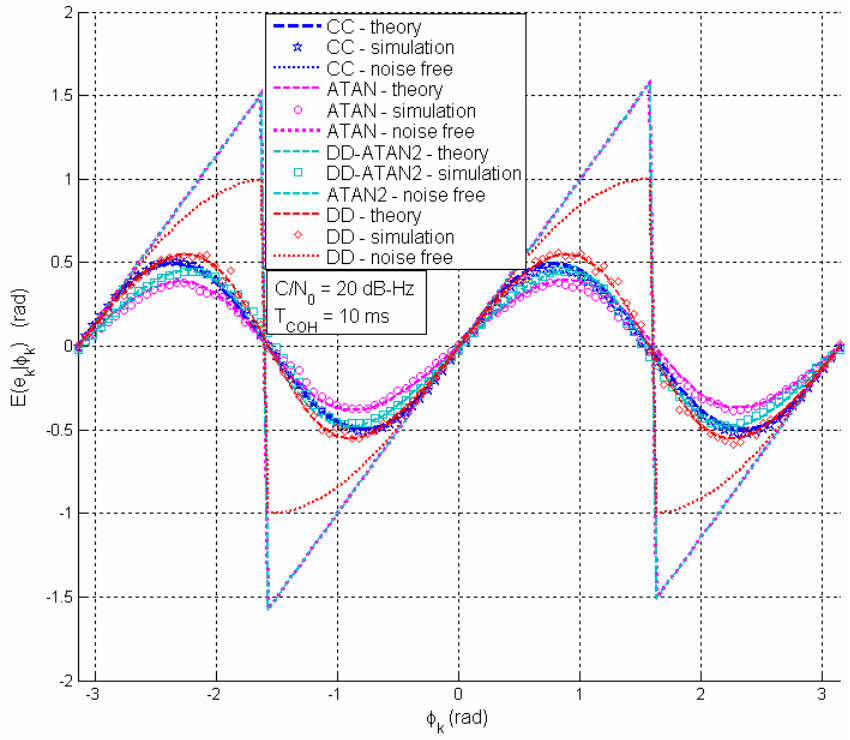


Figure 4-8: On-threshold behavior of the discriminators

The responses of the ATAN and DD-ATAN2 discriminators are almost identical, except that the latter results demonstrate slight improvement in low SNR situations (Figure 4-8); therefore, Figure 4-7 is considered to represent the performance of the ATAN family of discriminators versus $C/N_0$. This figure indicates that the ATAN discriminator largely underestimates the Doppler misalignment at low SNR condition, e.g. $SNR_{COH} < 10\ dB$.

Under such circumstance, the response of the ATAN reduces to a quasi-sine pattern. Additionally, the results of a Monte Carlo simulation justify the theoretical analysis.

Figure 4-8 shows the behavior of the discriminators in very low post-COH SNR. From the simulation results by symbols, the ATAN discriminator yields the largest bias while the DD-ATAN2 discriminator bias is slightly smaller, and the DD discriminator produces the least bias.

Besides the bias, the discriminator reveals the nonlinear relation between the observations , $\bar{I}_{p,k}^{Sig}$ and $\bar{Q}_{p,k}^{Sig}$, and the phase $\bar{\varphi}_k$ to be estimated. The variance of a CC discriminator is given by Humphreys et al. (2005) as

$$Var\left(\bar{n}_e^{CC}\right) = \frac{N_0}{2CT_{COH}}\left(1 + \frac{N_0}{2CT_{COH}}\right) \tag{4.16}$$

where

$1 + \frac{N_0}{2CT_{COH}}$ results from the product of noise at I and Q arms, termed squaring loss.

For the DD discriminator, noise at the I COH correlation contributes to the BER in estimating the bit sign. The noise variance only originates from noise at the Q branch, equal to

$$Var\left(\bar{n}_e^{DD}\right) = \frac{N_0}{2CT_{COH}} \tag{4.17}$$

Variances of the ATAN and DD-ATAN2 discriminators are defined on the basis of the conditional PDF given by eq. (4.13) as

$$Var\left(\bar{n}_e^{ATAN}\right)=\int_0^{\frac{\pi}{2}} e_k^2\left[\,p\left(e_k|0\right)+p\left(-\pi+e_k|0\right)\right]de_k + \int_{-\frac{\pi}{2}}^{0} e_k^2\left[\,p\left(e_k|0\right)+p\left(\pi+e_k|0\right)\right]de_k \quad (4.18)$$

$$Var\left(\bar{n}_e^{DD-ATAN2}\right)=\int_{-\pi}^{\pi} e_k^2\,p\left(e_k|0\right)de_k$$

Table 4-2: Elements for discriminators' bias and noise variance amplification

| Discriminator | Bias | Noise variance amplified by nonlinearity |
|---|---|---|
| CC | $sin(\cdot)$ | $\bar{n}_{p,I,k}^{Sig}\cdot\bar{n}_{p,Q,k}^{Sig}$ |
| DD | $sin(\cdot)+BER$ | $No$ |
| ATAN | $\left(\bar{n}_{p,I,k}^{Sig},\bar{n}_{p,Q,k}^{Sig}\right)$ | $a\tan(\cdot)+(\cdot/\cdot)$ |
| DD-ATAN2 | $\left(\bar{n}_{p,I,k}^{Sig},\bar{n}_{p,Q,k}^{Sig}\right)+BER$ | $a\tan 2(\cdot)+(\cdot/\cdot)$ |

Figure 4-9 shows variance results from the four types of discriminators studied here. From this figure, the variance differs between discriminators once the $SNR_{COH}$ is below 10 dB. The DD-ATAN2 PD produces the largest noise variance and the DD discriminator yields the lowest variance. The discriminator-induced bias and noise variance determine the tracking performance of a PLL.

Table 4-2 summarizes the sources contributing to the discriminators' measurement bias, and the nonlinear operation amplifying the noise variance.

A general linearized loop model is implemented, based on the examination of the discriminator's behaviour in the presence of noise, shown in Figure 4-10.

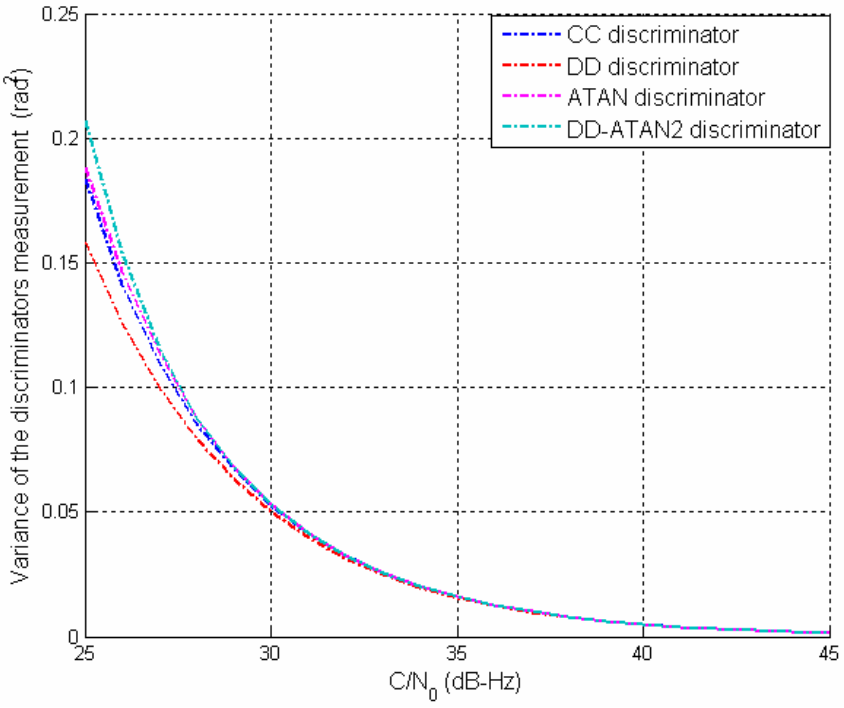


Figure 4-9: Variance of discriminators' measurement in various $C/N_0$ with $T_{COH} = 10\ ms$

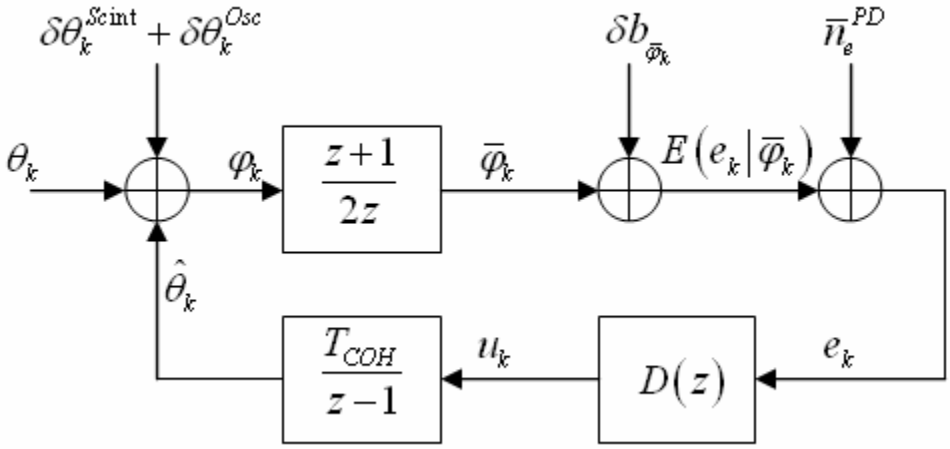


Figure 4-10: Linearized discrete model for a Costas loop

This model is based on eq (4.5). Compared with the model in Humphreys et al. (2005), Figure 4-10 accounts for more errors including the oscillator-induced phase jitter, scintillation-related phase noise and amplitude fading, and discriminators' bias in the context of

linear system theory, where

$\theta_k$ is the carrier phase of the received sample,

$\hat{\theta}_k$ is the local estimate of $\theta_k$,

$\delta\theta_k^{Osc}$ models the PHN induced by the instability of the OSC,

$\delta\theta_k^{Scint}$ depicts the phase variation resulting from the ionospheric scintillation whose PSD is modeled as $Tf^{-p}$ (Pullen et al. 1998, Hegarty et al. 2001),

$z+1/2z$ represents the "Accum & Dump" unit (Humphreys et al. 2005) in Figure 4-1,

$\delta b_{\bar{\varphi}_k}$ accounts for the bias due to noise disturbance or sine characteristic of the discriminator. This bias is jointly determined by the type of the discriminator, the post-COH SNR, and phase $\bar{\varphi}_k$ to be measured. The deep amplitude fading trigged by the scintillation causes the variation of post-COH SNR; therefore, the larger bias in a weak signal scenario further jeopardizes the carrier tracking operation,

$\bar{n}_{e,k}^{PDs}$ is noise associated with the normalized additive noise at $\bar{I}_{p,k}^{Sig}$ and $\bar{Q}_{p,k}^{Sig}$. Eq. (2.18) quantifies the variance of additive noise, $\bar{n}_{p,I,k}^{Sig}$ and $\bar{n}_{p,Q,k}^{Sig}$. The variance of $\bar{n}_{e,k}^{PDs}$ also depends on the type of discriminator; nonlinear operation of the discriminator amplifies the noise power, and thus excites a larger carrier tracking error. Humphreys et al. (2005) proves that the product operation of CC discriminator produces a larger

noise power, termed squaring loss, and therefore degenerates the carrier tracking capability. Noise variance for other types of the PDs are explicitly evaluated by eqs. (4.17)-(4.18).

$E\left[e_k|\bar{\varphi}_k\right]$ or $E\left[f(\bar{\varphi}_k)|\bar{\varphi}_k\right]$ as in eq. (4.5), denotes the response of the discriminator. The raw measured error $e_k$ is much noisier because of a wider noise bandwidth of $1/T_{COH}$; subsequently this error signal is de-noised by the loop filter $D(z)$ from which the output is used to drive the NCO.

The impact of the noise and perturbations on the carrier tracking performance is determined by

$$\sigma_n^2 = \int_0^{+\infty} S_n(f)\left|H_n(f)\right|^2 df \tag{4.19}$$

where

$S_n(f)$ is the one-sided PSD of the disturbance or noise,

$H_n(f)$ is the loop noise transfer function, which regards the input as the disturbance and output as the phase tracking error - more specifically $\bar{\varphi}_k$ in Figure 4-10.

Following Humphreys et al. (2005), two transfer functions, upon implementing the linearized general loop model, are used to determine the phase tracking error arising from the modeled disturbances or noises. The transfer functions are determined by both forward (input of disturbance to phase tracking error) and feedback (phase tracking error to input of disturbance) expressions.

The loop transfer function

$$H(z)=\frac{\left(\frac{z+1}{2z}\right)\left(\frac{T_{COH}}{z-1}\right)D(z)}{1+\left(\frac{z+1}{2z}\right)\left(\frac{T_{COH}}{z-1}\right)D(z)} \tag{4.20}$$

is related to the phase tracking error induced by the phase scintillation and the oscillator PHN.

The loop-AWGN transfer function

$$H_{\bar{n}_e^{PDs}}(z)=\frac{\left(\frac{T_{COH}}{z-1}\right)D(z)}{1+\left(\frac{z+1}{2z}\right)\left(\frac{T_{COH}}{z-1}\right)D(z)} \tag{4.21}$$

is used to determine the phase tracking error originating from the discriminator bias and the noise induced by the AWGN at normalized accumulations.

Using $z=1+j2\pi f$, we can acquire the analog counterparts, $H(f)$ and $H_{\bar{n}_e^{PDs}}(f)$, for transfer functions by eqs. (4.20) and (4.21). This linear transform is valid if only $\left|2\pi f\cdot T_{COH}\right|<<1$ can be satisfied. With the increase of the COH accumulation time, the loop roots for the digital PLL deviate away from the original ones under the assumption of a small $B_L T_{COH}$ (Stephens & Thomas 1995), thus causing the loop to become unstable. Correspondingly, the single-sided loop bandwidth and loop AWGN bandwidth take the forms of

$$B_L=\int_0^{+\infty}\left|H(f)\right|^2 df \tag{4.22}$$

$$B_{\bar{n}_e^{PDs}}=\int_0^{+\infty}\left|H_{\bar{n}_e^{PDs}}(f)\right|^2 df \tag{4.23}$$

In this chapter, three loop filter configurations will be used, namely Kaplan (1996), Parkinson & Spilker (1996), and Stephens & Thomas (1995). Table 4-3 clearly lists the parameters for each configuration and establishes the relationship between the parameters and loop transfer function. Stephens & Thomas (1995) eliminates the deviation resulting from the linear approximation caused by bilinear or box-car transform. Therefore, this design makes the bandwidth of digital filter perfectly match the desired value.

Table 4-3: Three CBPLL configurations

<table>
<tr><td></td><td colspan="2">Stephens & Thomas(1995)</td><td>Parkinson & Spilker (1996)</td><td>Kaplan (1996)</td></tr>
<tr><td></td><td>10 ms</td><td>20 ms</td><td>$T_{COH}$</td><td>$T_{COH}$</td></tr>
<tr><td>$K_1$</td><td>0.3248</td><td>0.5139</td><td colspan="2">$b_3^{(0)} T_{COH} \omega_0$</td></tr>
<tr><td>$K_2$</td><td>0.04147</td><td>0.1175</td><td colspan="2">$a_3^{(0)} T_{COH}^2 \omega_0^2$</td></tr>
<tr><td>$K_3$</td><td>0.001847</td><td>0.00976</td><td colspan="2">$\omega_0^3 T_{COH}^3$</td></tr>
<tr><td rowspan="3">$B_L = 15Hz$</td><td colspan="2" rowspan="3">$\frac{\hat{\theta}(z)}{\theta(z)} = \frac{z^2 \sum_{i=1}^{3} K_i + z(-K_2 - 2K_1) + K_1}{(z-1)^3}$</td><td>$b_3^{(0)} = 2$</td><td>$b_3^{(0)} = 2.4$</td></tr>
<tr><td>$a_3^{(0)} = 2$</td><td>$a_3^{(0)} = 1.1$</td></tr>
<tr><td>$\omega_0 = 1.2 B_L$</td><td>$\omega_0 = B_L / 0.7845$</td></tr>
</table>

Due to the Accum & Dump filter, the loop-AWGN bandwidth is not equal to the loop bandwidth (Humphreys et al. 2005). Figure 4-11 shows that, regardless of the Accum & Dump unit being accounted for or not, the loop-AWGN bandwidth increases the extension of the COH segment, i.e. there is a tradeoff between the gain obtained from the longer COH accumulation and the increase in noise power. When the Accum & Dump unit is considered (solid lines in Figure 4-11), the loop-AWGN bandwidth extends to 37 Hz conditioned on $T_{COH}$ of 20 ms. This bandwidth is wider than the case where the Ac-

cum & Dump is not considered (dashed line in Figure 4-11). Additionally, the root-controlled design of digital loop by Stephens & Thomas (1995) effectively solves the deviation caused by the transform from analog domain to digital domain. Using Table V in Stephens & Thomas (1995), the loop parameters for $B_L T_{COH} = 15 \times 0.02 = 0.3$ can be obtained. Under this configuration, the loop-AWGN bandwidth exactly meets the expectation of 15 Hz when excluding the Accum & Dump unit, or decreases from 37 Hz to 22 Hz when accounting for the Accum & Dump unit. Figure 4-11 displays the loop-AWGN bandwidth for a third-order loop, with the configuration described in Kaplan (1996) and a loop bandwidth of 15 Hz.

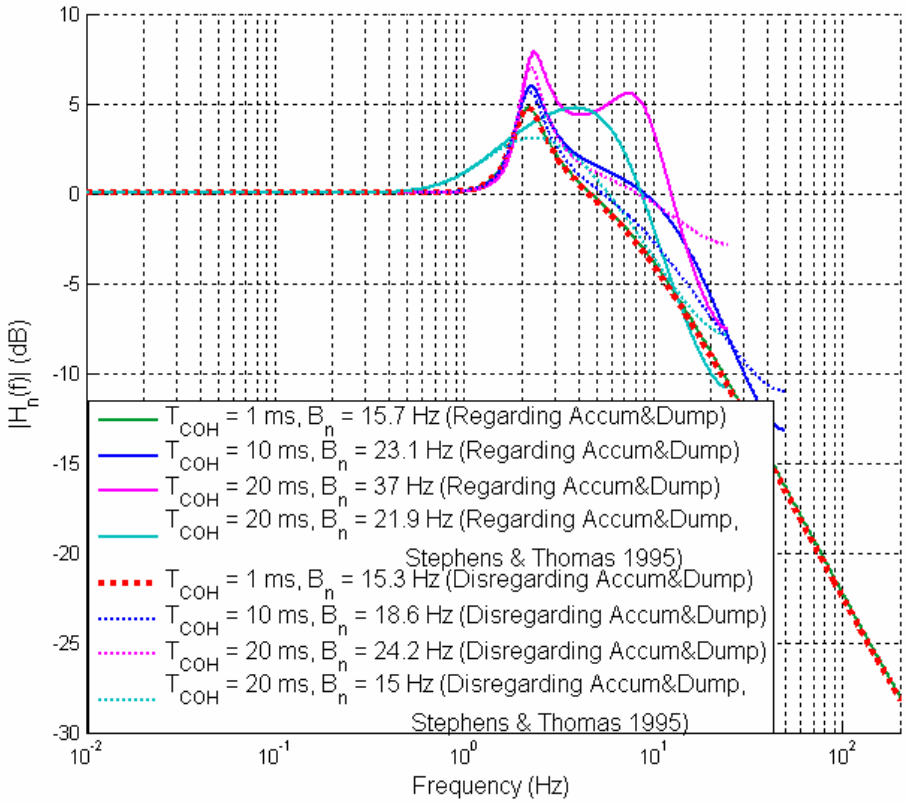


Figure 4-11: Equivalent noise bandwidth vs. $T_{COH}$ with $B_L = 15$ Hz

In Table 4-4, the one-sided PSD and transfer function for each perturbation are listed. Applying these items to eq. (4.19), the phase tracking error from each interference can be

derived. The total error (1-sigma) is the second root of the sum of square (SoS) of each error component. The transfer function in eq. (4.19) is equal to or is a function of $H(f)$ and $H_{\bar{n}_e^{PDs}}(f)$. The PSD of $\bar{n}_{e,k}^{PDs}$ varies for different discriminators; the nonlinearity of the discriminator causes the variance of $\bar{n}_{e,k}^{PDs}$ to be greater than that of $\bar{n}_{p,I,k}^{Sig}$ and $\bar{n}_{p,Q,k}^{Sig}$. Assuming that $\bar{n}_{e,k}^{PDs}$ is a stationary random process, $S_{\bar{n}_e^{PDs}}(f)$ for CC discriminator is

$$Var\left(f_{CC}\left(\bar{\varphi}_k\right)\middle|\bar{\varphi}_k\right)\cdot T_{COH}=\frac{N_0}{C}\left(1+\frac{N_0}{2CT_{COH}}\right) \tag{4.24}$$

(Humphreys et al. 2005) and for the DD discriminator is

$$Var\left(f_{DD}\left(\bar{\varphi}_k\right)\middle|\bar{\varphi}_k\right)\cdot T_{COH}=\frac{N_0}{C} \tag{4.25}$$

For ATAN and DD-ATAN2, $Var\left(f\left(\bar{\varphi}_k\right)\middle|\bar{\varphi}_k\right)\cdot T_{COH}$ can only be derived by numerical integration of the conditional PDF in eq. (4.13).

Table 4-4: PSD and transfer functions for each perturbation

| Perturbation | $H_n(f)$ | $S_n(f)$ | Affected by amplitude scintillation |
|---|---|---|---|
| $\bar{n}_{e,k}^{PDs}$ | $H_{\bar{n}_e^{PDs}}(f)$ | $Var\left(f\left(\bar{\varphi}_k\right)\middle|\bar{\varphi}_k\right)\cdot T_{COH}$ | Yes |
| $\delta b_{\bar{\varphi}_k}$ | $H_{\bar{n}_e^{PDs}}(f)$ | $\delta b_{\bar{\varphi}_k}^2\cdot\delta(f)$ | Yes |
| $\delta\theta_k^{Osc}$ | $1-H(f)$ | $\sum_{i=-2}^{0} h_i f^{i-2}$ | No |
| $\delta\theta_k^{Scint}$ | $1-H(f)$ | $Tf^{-p}$ | No |

These carrier tracking results demonstrate that, compared with the DD loop, other types of loop produces a larger phase tracking error due to the nonlinearity operation on the

noise. The results for CBPLL performance are described in section 4.1.2 for the interference of AWGN, in section 4.1.3 for OSC-induced PHN, and in section 4.1.4 for the case of ionospheric scintillation.

### 4.1.2 Optimization of a CBPLL in the Presence of Thermal Noise

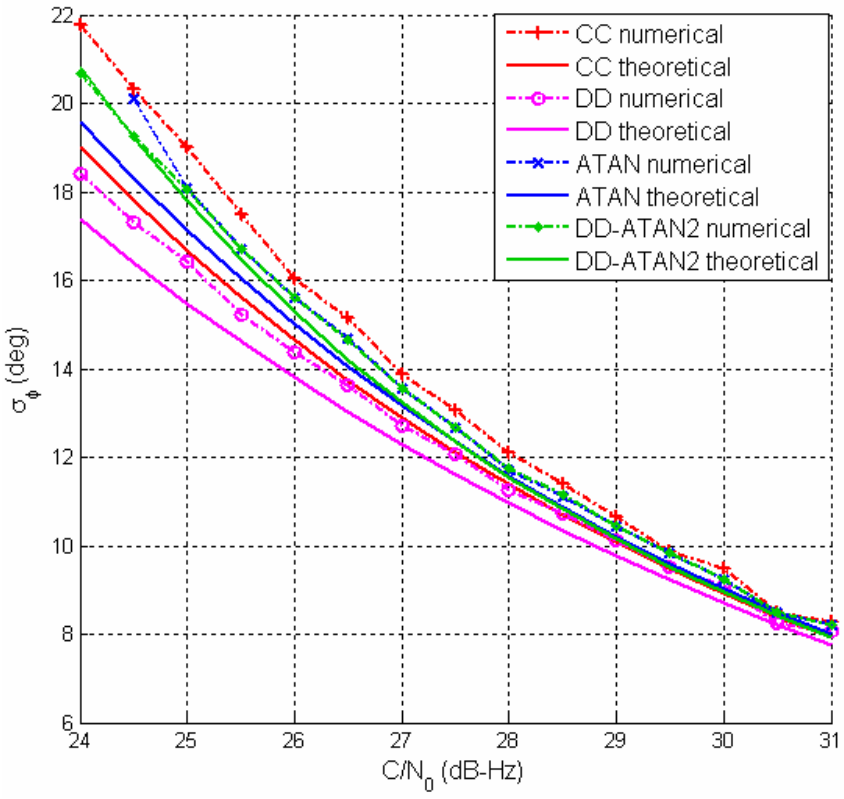


Figure 4-12: Phase tracking error induced by additive WGN

Figure 4-12 depicts the on-threshold behavior of the CBPLLs. In this region, nonlinear characteristics of the discriminators CC, ATAN, and DD-ATAN2 amplify the noise variance and result in a severe bias problem, subsequently creating a larger tracking error and then increasing the probability of loss of lock. Besides increasing the noise variance, the larger bias induced by CC, ATAN and DD-ATAN2 discriminators in the low $C/N_0$ re-

gion degrades the performance. In Figure 4-12 the dash-symbol lines from the numerical experiment validate the theoretical predictions (solid lines) based on theory described in section 4.1.1. The DD outperforms other types of CBPLLs due to the better behavior and absence of nonlinear loss in the low $C/N_0$ region. Correspondingly, in considering the dash symbol lines in Figure 4-13, the DD loop has a lower probability of cycle slips and shows about 2 dB sensitivity improvement compared with other types of CBPLLs at the threshold for occurrence of cycle slips.

The comprehensive analysis based on both Figure 4-12 and the dash symbol lines in Figure 4-13 proves that cycle slips may occur once the phase tracking error exceeds the rule-of-thumb threshold of 15 degrees (Kaplan 1996). Figure 4-12 and the dash symbol lines in Figure 4-13 are generated based on the Kaplan (1996) configuration for a 3rd-order loop and boxcar transform. The COH accumulation interval is set to 10 ms and the loop bandwidth is 15 Hz. As shown in Figure 4-11, the digital loop design by Kaplan (1996) causes the noise bandwidth of the digital loop to become wider than the target bandwidth set for its analog counterpart. The method proposed by Stephens & Thomas (1995) parameterizes the digital loop to meet its target bandwidth based on $B_L T_{COH}$, equal to 0.15 for the case presented by Figure 4-12 and the solid symbol lines in Figure 4-13. Utilizing the values in Table 4-3, the parameters for the 3rd-order loop can be quantified to implement a simulation under the identical conditions. The results shown in Figure 4-13 and Figure 4-14 demonstrate that (1) the phase tracking error has been re-

duced by 2 degrees in weak signal conditions, and (2) the sensitivity in suppressing the cycle slip improves by 1 to 1.5 dB.

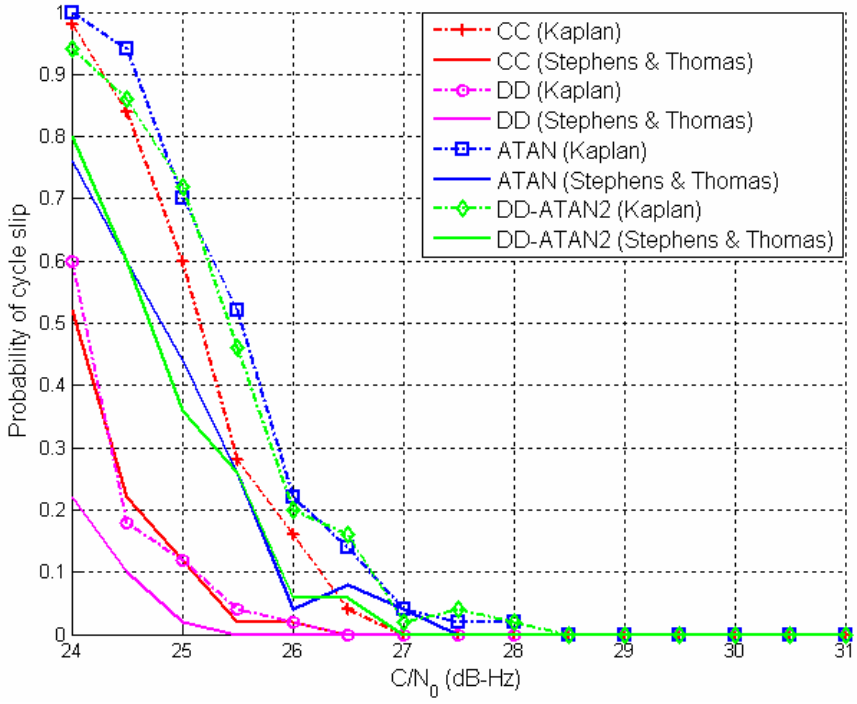


Figure 4-13: Probability of cycle slip (Kaplan configuration vs. Stephens & Thomas configuration)

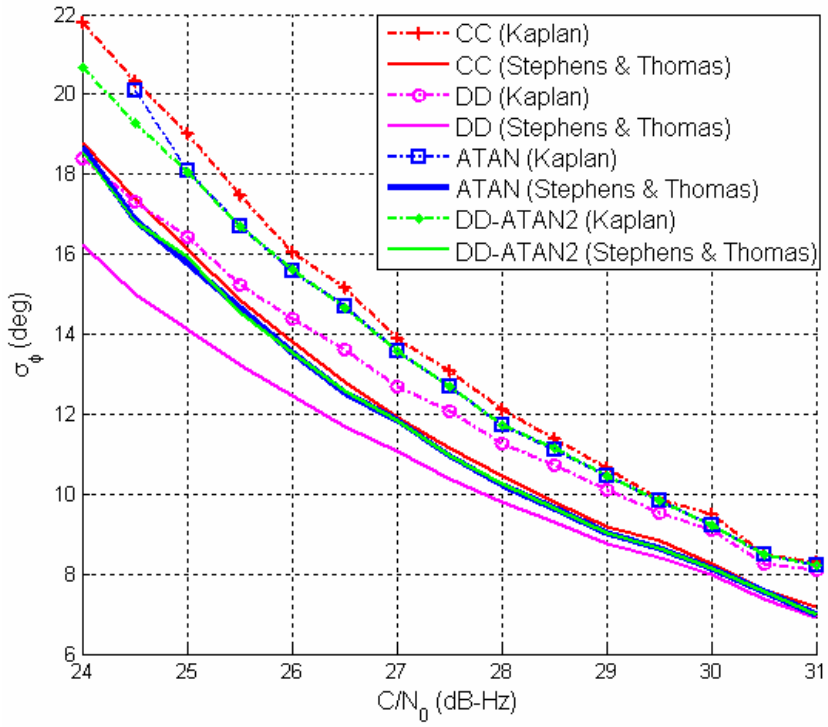


Figure 4-14: Phase tracking error (Kaplan configuration vs. Stephens & Thomas configuration)

### 4.1.3 Optimization of a CBPLL in the Presence of Oscillator Phase Noise

Figure 4-15 compares the phase error caused by the OSC's PHN for different oscillators and loop configurations. Parkinson & Spilker (1996) and Kaplan (1996) present two loop configurations that adopt different loop filter parameters. Both settings are widely used by a GPS receiver and are evaluated here. The results prove (1) the Parkinson configuration outperforms the Kaplan parameter in mitigating the phase error, and (2) the tracking error is primarily determined by the short-term stability of the oscillator, which is associated with the WFM. The PHN-induced tracking error is not significantly different for different CBPLLs.

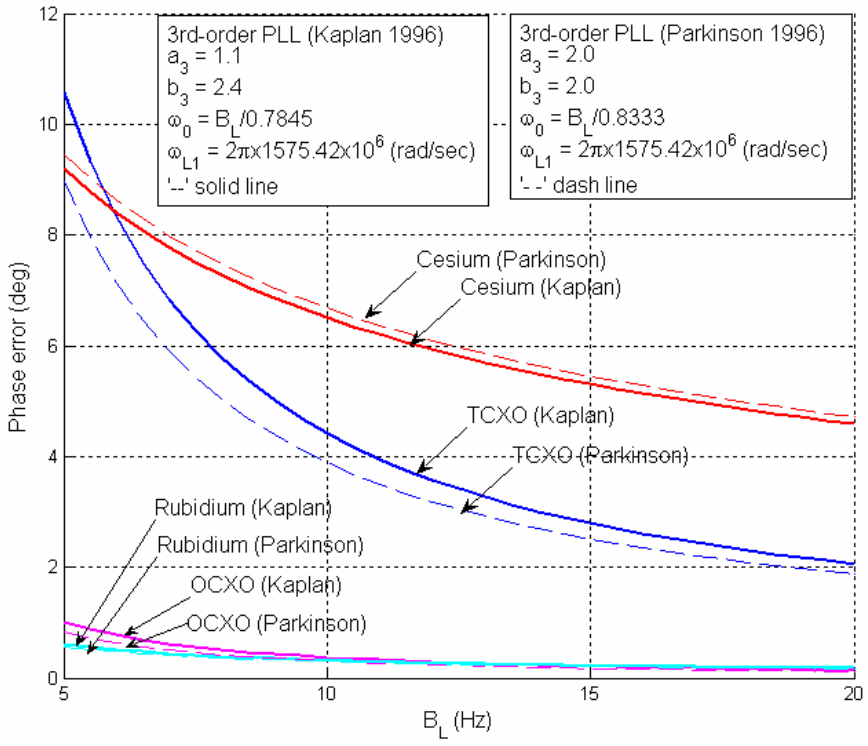


Figure 4-15: Phase tracking error induced by OSC's PHN

### 4.1.4 Optimization of a CBPLL in the Presence of Ionospheric Scintillation

Thus far, no real data has been recorded for studies during ionospheric scintillation because the magnetic activity is at a "solar minimum." To quantify the phase tracking performance under controlled ionospheric disturbances, we simulate the oscillator's PHN and ionospheric scintillation effects to add errors to the GPS signal. The black line in Figure 4-16 to Figure 4-19 represents the rule-of-thumb tracking threshold (Kaplan 1996). Figure 4-16 illustrates the carrier tracking results of CBPLLs under different scintillation intensities. Here a strong phase scintillation is assumed, i.e. $\sigma_{\delta\theta^{Scint}} = 0.6$ , and the amplitude scintillation ranges from weak to strong, which is negatively correlated with scintillation-related phase fluctuation by -0.6. The DD loop (square-dash line) consistently displays a 1-2 dB sensitivity improvement compared with the ATAN and CC loops. This

figure demonstrates that the strength of the amplitude scintillation (Table 2-3) is closely associated with the carrier tracking performance. The minimum signal strength in keeping carrier lock increases from 28 dB-Hz for weak amplitude scintillation to 43 dB-Hz for strong amplitude scintillation. The deep power fades intensify the nonlinear behaviour of the discriminator's response, thus resulting in the susceptibility of losing phase lock.

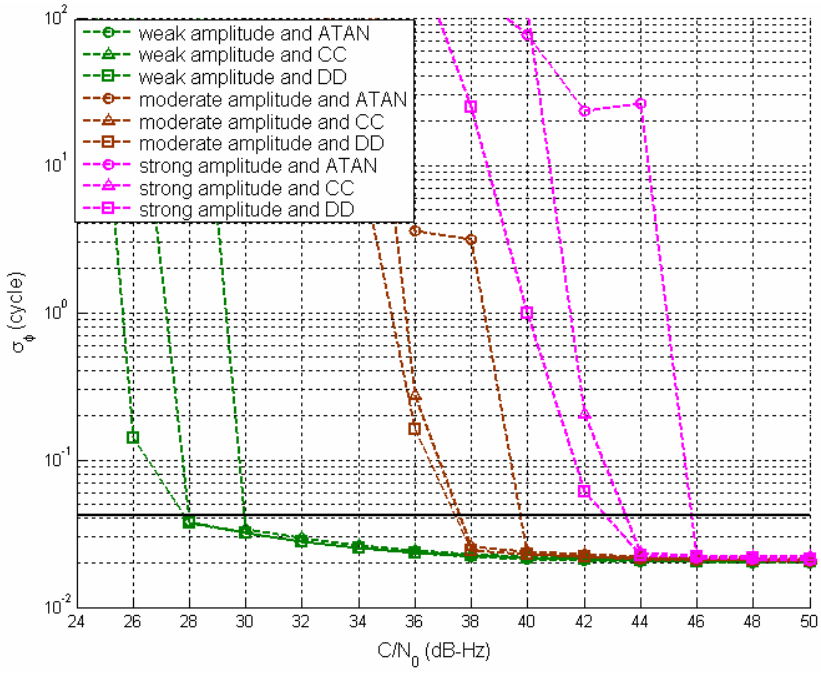


Figure 4-16: Phase tracking error for different levels of amplitude scintillation (TCXO assumed)

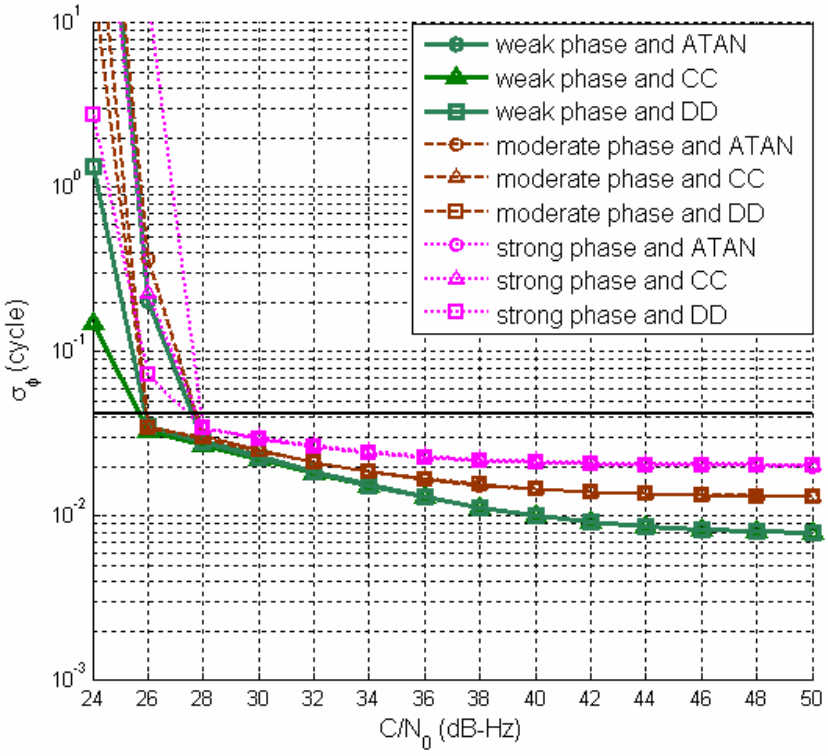


Figure 4-17: Phase tracking error for different levels of phase scintillation (TCXO assumed)

Compared with the intensity of amplitude variation, the strong phase variation triggered by scintillation does not apparently degrade the tracking performance as shown in Figure 4-17. This figure assumes constant weak amplitude scintillation (Table 2-3). Because the SNR value is stable, in this case, during the occurrence of small power variations associated with scintillation, the phase tracking error arising from the additive WGN and the measurement bias are less variable. This figure proves that the SNR condition is more important in determining the phase tracking capability and accuracy.

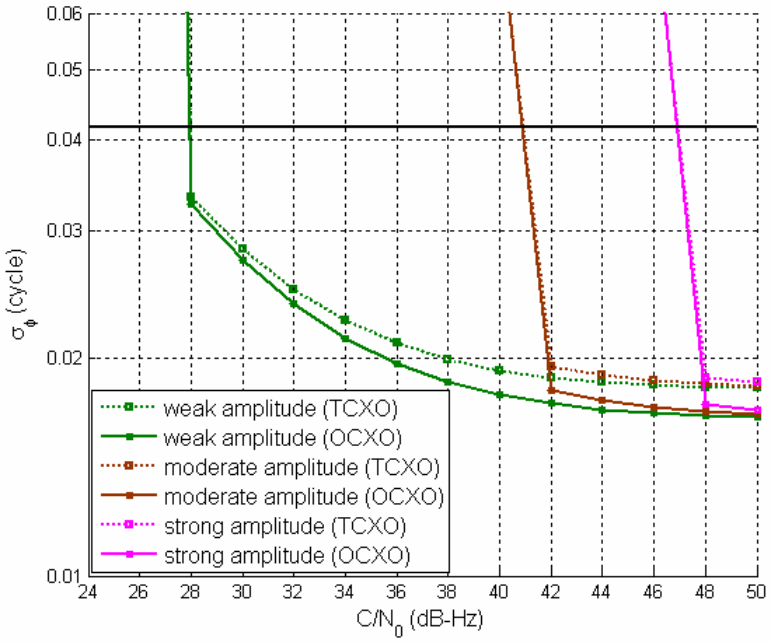


Figure 4-18: Phase tracking error for different levels of amplitude scintillation under two types of OSCs

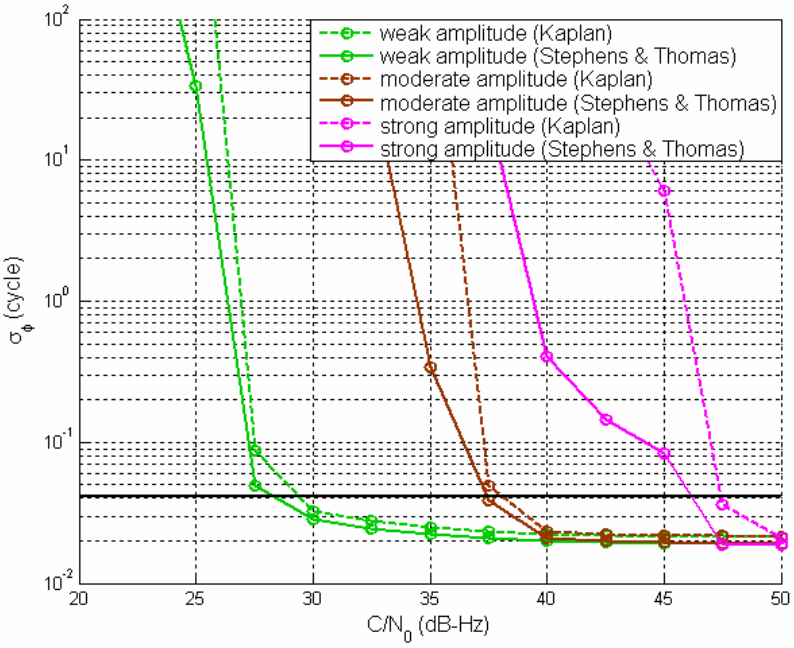


Figure 4-19: Phase tracking error for different levels of amplitude scintillation under two types of loop configurations (Kaplan vs. Stephens & Thomas)

The results shown by the above two figures are consistent with those presented in Hegarty et al. (2001). A TCXO is assumed in the simulations conducted for Figure 4-16 and Figure 4-17. To evaluate the tracking performance as a function of OSC, Figure 4-18 demonstrates that the use of a high quality OSC such as OCXO does not provide obvious sensitivity improvement; however the tracking error is slightly mitigated. This conclusion is consistent with the description for Figure 2-18, where the carrier tracking performance is determined by the short-term stability of the receivers' OSC due to the update rate of 20 ms. With the deployment of new GNSS systems, the pilot channel allows a sensitivity improvement through extending the COH accumulation interval. Under such circumstance, the tracking performance will be associated with the medium- to long-term stability of OSCs. The high quality OSC results in performance improvement. Figure 4-18 again assumes a strong phase scintillation with amplitude scintillation varying from weak to strong.

In generating the previous figures, a target loop bandwidth of 15 Hz with the Kaplan (1996) configuration is assumed. As previously mentioned, the loop additive WGN bandwidth deviates from the desired expectation due to the nonlinear effect missed by bilinear or box-car transform. This effect cannot be neglected when $B_L T_{COH}$ is greater than 0.1 (Stephens & Thomas 1995). By adopting the parameters given in Stephens & Thomas (1995), the bandwidth is much closer to the desired design. Figure 4-19 illustrates the tracking performance improvement. Here, the sensitivity is enhanced by about 1 to 2 dB for different levels of amplitude scintillation. At the same time, by fixing the conditions of the numerical experiment, the Stephens & Thomas (1995) setting also mitigates the phase tracking error compared with the Kaplan (1996) configuration.

## 4.2 Adaptive Carrier Tracking Enhancement

A carrier tracking loop can be optimized through reconfiguring each unit in the loop (Figure 4-1), namely the COH accumulation time, the type of PDs, the loop order, and the loop filter. The constant loop filter with configuration of Kaplan (1996) and Parkinson & Spilker (1996) is widely used in a GPS receiver. Lindsey (1981) and references therein extensively study the adaptive carrier tracking approaches enable better phase tracking in the presence of strong error sources. As described previously, the normalized noise variance is inversely proportional to SNR; therefore the low SNR causes a larger phase tracking jitter. Reducing the loop AWGN bandwidth can mitigate the effect of this noise; nevertheless doing so increases the tracking error caused by the PHN and ionospheric phase scintillation. Besides the noise power, under low SNR condition, Figure 4-8 well illustrates the bias resulting from on-threshold behaviour of the discriminators; thus, the phase should be derived in tight tracking mode to guarantee that the discriminator operates within a linear region. However, this becomes quite difficult when occurring the intensive phase variation and amplitude fades, e.g. in the presence of ionosphere scintillation. Therefore, a KF can be used because the bandwidth chosen by this estimator is optimal in the sense of minimum mean square error (MMSE) based on the assumption of WGN. The concept of this adaptive tracking approach is reviewed by Lindsey & Chie (1981). Psiaki (2001b) and its references initialize to build a KF based carrier tracker. This estimator provides a constant Kalman gain by only solving the steady-state Recatti equation. The resultant filtering estimates are then optimized by a smoothing algorithm. Additionally, it does not deal with the ambiguity of the data modulation (suppressed carrier) in a soft approach (Humphreys et al. 2005). To enhance this technique in tracking

weak signals, Psiaki & Jung (2002) implement the extended KF that is specially designed for tracking weak carrier-suppressed GPS signals and is summarized here. This algorithm propagates based on the square root information filtering (SRIF) technique.

### 4.2.1 Square Root Information Filtering Technique

The basics of the KF technique are reviewed in Bierman (1977). KF can be used to describe a system based on a dynamic and an observation model. The dynamic model reflects the variation of systematic states over time, and the observation model is a function of the systematic states. KF is built on linear system theory, however nonlinearity is unavoidable in many real applications. In this case, the Taylor expansion is used to derive a linear approximation for both the dynamic and observation models epoch by epoch, reducing the problem into the linear system context.

The normal KF propagates the state estimation and performs the observation update based on the covariance matrix

$$P^{est} = E\left[\left(x - x^{est}\right)\left(x - x^{est}\right)^{T}\right] \tag{4.26}$$

where

$x$ is the actual state vector, and

$x^{est}$ is the estimated state, which could be a priori estimate $\tilde{x}$, and posteriori estimate $\hat{x}$, correspondingly associated with

$\tilde{P}$, the priori covariance matrix and,

$\hat{P}$ posteriori covariance matrix.

The priori estimate results from all the observations up to previous epoch, while the posteriori estimate includes update with the current observation.

Bierman (1977) describes that the KF generates an optimal $\hat{x}$ by minimizing the cost function of

$$J(x) = (x - \tilde{x})^T \tilde{P}^{-1} (x - \tilde{x}) + (z - Ax)^T (z - Ax) \tag{4.27}$$

where

$z - Ax$ is the measurement noise equal to the actual observation minus the system-derived observation, and $A$ reveals the relationship between the observation and systematic states, called the design matrix.

$\tilde{P}^{-1}$ is the inverse of covariance matrix, called the information matrix.

According to eq. (4.26), $P^{est^{-1}}$ is the positive definite matrix that can be factored into a lower triangle matrix $R^{est^T}$ times its transpose $R^{est}$. The SRIF propagates the KF estimator based on the upper triangle factor of $R^{est}$. The square root filter has inherently better stability and numeric accuracy than does normal Kalman filter (Bierman 1977). The improved numerical behaviour of square root algorithms is due in great part to the reduction of the numerical ranges of the variables (Bierman 1977).

Based on the above basic concepts, the implementation of an extended KF based carrier tracking algorithm is developed based on Psiaki & Jung (2002), Psiaki & Humphreys (2006) and Bierman (1977).

### 4.2.2 Extended Kalman Filter based Carrier Tracking

The extended KF based carrier tracking algorithm developed by Psiaki & Jung (2002) is derived at a very basic level, and the reference provides detailed information in realizing this algorithm.

The dynamic model is (Psiaki & Jung 2002)

$$\begin{bmatrix} \varphi \\ \omega_d \\ \dot{\omega}_d \\ a \end{bmatrix}_{k+1} = \begin{bmatrix} 1 & \delta t_k & \frac{\delta t_k^2}{2} & 0 \\ 0 & 1 & \delta t_k & 0 \\ 0 & 0 & 1 & 0 \\ 0 & 0 & 0 & 1 \end{bmatrix} \begin{bmatrix} \varphi \\ \omega_d \\ \dot{\omega}_d \\ a \end{bmatrix}_k + \begin{bmatrix} -\delta t_k \\ 0 \\ 0 \\ 0 \end{bmatrix} \hat{\omega}_{d,k} + \begin{bmatrix} 1 & 0 & 0 & 0 & 0 \\ 0 & 1 & 0 & 0 & 0 \\ 0 & 0 & 1 & 0 & 0 \\ 0 & 0 & 0 & 0 & 1 \end{bmatrix} \begin{bmatrix} w_\varphi \\ w_\omega \\ w_{\dot{\omega}} \\ w_j \\ w_a \end{bmatrix}_k \quad (4.28)$$

where

$[\varphi, \omega_d, \dot{\omega}_d, a]^T$ is the vector of states to be estimated. These elements respectively represent the phase misalignment, actual angular Doppler inherited in the signal, the drift of the angle Doppler, and the natural logarithm of the amplitude.

$\hat{\omega}_d$ is the locally estimated angular Doppler,

$\delta t_k$ is the COH accumulation time. Due to the LOS motion, COH time is not always a constant, and is related to the carrier Doppler and drift of Doppler as $\delta t_k = \frac{\omega_{L1} T_{COH}}{\omega_{L1} + \omega_{d,k} + 0.5\dot{\omega}_{d,k} T_{COH}}$ (Psiaki & Jung 2002)

which is simply noted as

$$x_{k+1} = \Phi_{k|k-1} x_k + \Gamma_{xk} \hat{\omega}_{d,k} + \Gamma_{wk} w_k \quad (4.29)$$

This mode assumes an acceleration-varying dynamic model which is driven by a random jerk. The phase differenc at $k+1$ results from the difference of actual Doppler accumulation $\omega_{d,k} \cdot \delta t_k$ and estimated Doppler accumulation of $\hat{\omega}_{d,k} \cdot \delta t_k$ .

The observation of COH accumulations at I and Q channels is (Psiaki & Jung 2002)

$$y_k = h(x_k, w_k) = \begin{bmatrix} \bar{I}_{p,k}^{Noise} \\ \bar{Q}_{p,k}^{Noise} \end{bmatrix} = \begin{cases} \dfrac{\tilde{A}_k}{\sigma_s / \sqrt{N_k^{COH}}} \cdot d_{m,k} \cdot cos(\bar{\varphi}_k) + \bar{n}_{p,I,k}^{Noise} \\ \dfrac{\tilde{A}_k}{\sigma_s / \sqrt{N_k^{COH}}} \cdot d_{m,k} \cdot sin(\bar{\varphi}_k) + \bar{n}_{p,Q,k}^{Noise} \end{cases} \tag{4.30}$$

after eqs. (3.1) and (3.2).

where $\tilde{A}_k$ and $\bar{\varphi}_k$ are associated with the estimated state as (Psiaki & Jung 2002)

$$\begin{cases} \tilde{A}_k = e^{a_k + 0.5 w_k} \\ \bar{\varphi}_k = C_k x_k + D_{xk} \hat{\omega}_{d,k} + D_{wk} w_k \end{cases} \tag{4.31}$$

where

$$C_k = \begin{bmatrix} 1 & \dfrac{\delta t_k}{2} & \dfrac{\delta t_k^2}{6} & 0 \end{bmatrix}$$

$$D_{xk} = -\frac{\delta t_k}{2}$$

$$D_{wk} = \begin{bmatrix} 0 & 0 & 0 & 1 & 0 \end{bmatrix}$$

and the $d_{m,k}$ term does not switch its polarization during a nominal interval of 20 ms.

The observations can be regarded as a Taylor expansion at the prediction point,

$$y_k = h\left(\tilde{x}_k, 0\right) + \left.\frac{\partial h}{\partial x^T}\right|_{\left(\tilde{x}_k, 0\right)} \left(x_k - \tilde{x}_k\right) + \left.\frac{\partial h}{\partial w^T}\right|_{\left(\tilde{x}_k, 0\right)} w_k \tag{4.32}$$

in which $\tilde{x}_k$ is an a priori estimation of the $x_k$ based on the all the observations up to epoch $k-1$, and

the two derivatives respectively are

$$\begin{aligned} \frac{\partial h}{\partial x^T} &= \frac{\tilde{A}_k}{\sigma_s / \sqrt{N_k^{COH}}} d_{m,k} \begin{bmatrix} -\sin\bar{\varphi}_k C_k & \cos\bar{\varphi}_k \\ \cos\bar{\varphi}_k C_k & \sin\bar{\varphi}_k \end{bmatrix} \\ \frac{\partial h}{\partial w^T} &= \frac{\tilde{A}_k}{\sigma_s / \sqrt{N_k^{COH}}} d_{m,k} \begin{bmatrix} -\sin\bar{\varphi}_k D_{wk} & 0.5\cos\bar{\varphi}_k \\ \cos\bar{\varphi}_k D_{wk} & 0.5\sin\bar{\varphi}_k \end{bmatrix} \end{aligned} \tag{4.33}$$

In addition,

$$\tilde{y}_k = h\left(\tilde{x}_k, 0\right) \tag{4.34}$$

which is a term in eq. (4.32) called predicted measurement.

The goal of the KF approach is to determine the optimal estimation of $\left(\hat{x}_k, \hat{w}_{k-1}\right)$ that minimizes the cost function of (Psiaki & Jung 2002)

$$\begin{aligned} J = &\frac{1}{2}\left[\tilde{R}_{xxk}\left(x_k - \tilde{x}_k\right)\right]^T \left[\tilde{R}_{xxk}\left(x_k - \tilde{x}_k\right)\right] + \frac{1}{2}\left[\tilde{R}_{wwk} w_k\right]^T \left[\tilde{R}_{wwk} w_k\right] + \\ &\frac{1}{2}\left[y_k - h\left(x_k, w_k\right)\right]^T \left[y_k - h\left(x_k, w_k\right)\right] \\ s.t. \\ &x_{k+1} = f\left(x_k, w_k\right) \end{aligned} \tag{4.35}$$

This cost function has one additional term compared with that for the standard well-known KF estimator. The second term in eq. (4.35) indicates that the process noise is included in the KF, where the state vector to be estimated becomes $\left[w_k^T, x_k^T\right]^T$. The optimal estimate results in the global minimum of $J$. Herein, the square root informa-

tion filtering (SRIF) technique is adopted to drive the propagation of this KF estimator. The following derivations provide necessary background for the realization of this technique.

Transforming eq. (4.29) into

$$x_k = \Phi_{k|k-1}^{-1}\left(x_{k+1} - \Gamma_{xk}\hat{\omega}_{d,k} - \Gamma_{wk}w_k\right) \tag{4.36}$$

and applying eq. (4.36) into the first term of eq. (4.35) results in

$$\tilde{R}_{xxk}\left(x_k - \tilde{x}_k\right) = \left(\tilde{R}_{xxk}\Phi_k^{-1}\right)x_{k+1} - \left(\tilde{R}_{xxk}\Phi_k^{-1}\Gamma_{wk}\right)w_k - \tilde{R}_{xxk}\left(\Phi_k^{-1}\Gamma_{xk}\hat{\omega}_{d,k} + \tilde{x}_k\right) \tag{4.37}$$

The third item on the right side of eq. (4.35), on the condition of the eqs. (4.32) and (4.36), is equivalent with

$$\begin{aligned} & y_k - h\left(\tilde{x}_k,0\right) + \frac{\partial h\left(\tilde{x}_k,0\right)}{\partial x^T}\tilde{x}_k \\ &= \frac{\partial h\left(\tilde{x}_k,0\right)}{\partial x^T}x_k + \frac{\partial h\left(\tilde{x}_k,0\right)}{\partial w^T}w_k \\ &= \frac{\partial h\left(\tilde{x}_k,0\right)}{\partial x^T}\Phi_k^{-1}x_{k+1} + \left(\frac{\partial h\left(\tilde{x}_k,0\right)}{\partial w^T} - \frac{\partial h\left(\tilde{x}_k,0\right)}{\partial x^T}\Phi_k^{-1}\Gamma_{wk}\right)w_k \\ &\quad - \left[\frac{\partial h\left(\tilde{x}_k,0\right)}{\partial x^T}\Phi_k^{-1}\Gamma_{xk}\hat{\omega}_{d,k} + \left(y_k - h\left(\tilde{x}_k,0\right) + \frac{\partial h\left(\tilde{x}_k,0\right)}{\partial x^T}\tilde{x}_k\right)\right] \end{aligned} \tag{4.38}$$

Based on the eqs. (4.37) and (4.38), the cost function $J$ in eq. (4.35) can be expressed in a matrix layout as

$$J=\frac{1}{2}\left\|\begin{bmatrix}\tilde{R}_{wwk} & 0\\ -\tilde{R}_{xxk}\Phi_k^{-1}\Gamma_{wk} & \tilde{R}_{xxk}\Phi_k^{-1}\\ \dfrac{\partial h\left(\tilde{x}_k,0\right)}{\partial x^T}-\dfrac{\partial h\left(\tilde{x}_k,0\right)}{\partial x^T}\Phi_k^{-1}\Gamma_{wk} & \dfrac{\partial h\left(\tilde{x}_k,0\right)}{\partial x^T}\Phi_k^{-1}\end{bmatrix}\begin{bmatrix}w_k\\ x_{k+1}\end{bmatrix}-\right.$$
$$\left.\begin{bmatrix}0\\ \tilde{R}_{xxk}\left(\Phi_k^{-1}\Gamma_{xk}\hat{\omega}_{d,k}+\tilde{x}_k\right)\\ \dfrac{\partial h\left(\tilde{x}_k,0\right)}{\partial x^T}\Phi_k^{-1}\Gamma_{xk}\hat{\omega}_{d,k}+\left(y_k-h\left(\tilde{x}_k,0\right)+\dfrac{\partial h\left(\tilde{x}_k,0\right)}{\partial x^T}\tilde{x}_k\right)\end{bmatrix}\right\|^2 \tag{4.39}$$

QR factorization is used here to minimize the cost $J$. Assuming

$$\begin{bmatrix}\tilde{R}_{wwk} & 0\\ -\tilde{R}_{xxk}\Phi_k^{-1}\Gamma_{wk} & \tilde{R}_{xxk}\Phi_k^{-1}\\ \dfrac{\partial h\left(\tilde{x}_k,0\right)}{\partial w^T}-\dfrac{\partial h\left(\tilde{x}_k,0\right)}{\partial x^T}\Phi_k^{-1}\Gamma_{wk} & \dfrac{\partial h\left(\tilde{x}_k,0\right)}{\partial x^T}\Phi_k^{-1}\end{bmatrix}=Q_G\begin{bmatrix}R_G\\ 0\end{bmatrix} \tag{4.40}$$

(Psiaki & Jung 2002) and

$$\begin{bmatrix}0\\ \tilde{z}_k\\ \hat{z}_k\end{bmatrix}=\begin{bmatrix}0\\ -\tilde{R}_{xxk}\Phi_k^{-1}\Gamma_{xk}\hat{\omega}_{d,k}\\ \dfrac{\partial h\left(\tilde{x}_k,0\right)}{\partial x^T}\Phi_k^{-1}\Gamma_{xk}\hat{\omega}_{d,k}+\left(y_k-h\left(\tilde{x}_k,0\right)+\dfrac{\partial h\left(\tilde{x}_k,0\right)}{\partial x^T}\tilde{x}_k\right)\end{bmatrix} \tag{4.41}$$

the cost function $J$ of eq. (4.39) is finalized as

$$J=\left\|\begin{bmatrix}R_G\\ 0\end{bmatrix}\begin{bmatrix}w_k\\ x_{k+1}\end{bmatrix}-Q_G^T\begin{bmatrix}0\\ \tilde{z}_k\\ \hat{z}_k\end{bmatrix}\right\|^2 \tag{4.42}$$

Thus the optimal estimation

$$\begin{bmatrix} \hat{w}_k^{+(0)} \\ \tilde{x}_{k+1}^{+(0)} \end{bmatrix} = \left[R_G\right]^{-1} Q_G^T \begin{bmatrix} 0 \\ \tilde{z}_k \\ \hat{z}_k \end{bmatrix} \tag{4.43}$$

minimizes the cost function, where

$\tilde{x}_{k+1}^{+(0)}$ represents the priori estimates based on all the observations up to epoch $k$ and $\hat{w}_k^{+(0)}$ is the initial filtering estimate of the noise.

The superscripts of $\tilde{x}_{k+1}^{+(0)}$ and $\hat{w}_k^{+(0)}$ indicate the solution given by eq. (4.43) results from the Gauss-Newton approximation. This method does not account for the second-derivative terms of $\frac{\partial^2 J}{\partial x\, \partial x^T}$, $\frac{\partial^2 J}{\partial w\, \partial w^T}$, $\frac{\partial^2 J}{\partial x\, \partial w^T}$ and $\frac{\partial^2 J}{\partial w\, \partial x^T}$ (Psiaki & Jung 2002). The last two items are transposes of each other. Applying the estimated $\begin{bmatrix} \hat{w}_k^{+(0)^T} & \tilde{x}_{k+1}^{+(0)^T} \end{bmatrix}^T$, eq. (4.43), into eq. (4.36), we achieve the initial filtering estimate of

$$\hat{x}_k^{+(0)} = \Phi_k^{-1}\left(\tilde{x}_{k+1} - \Gamma_{xk}\hat{\omega}_{d,k} - \Gamma_{wk}\hat{w}_k^{+(0)}\right) \tag{4.44}$$

and a Gauss-Newton approximation with measurement at epoch $k$ is adopted. With the dynamic model of eq. (4.29), we achieve

$$\tilde{x}_{k+1}^{-(0)} = \Phi_k \tilde{x}_k + \Gamma_{xk}\hat{\omega}_{d,k} \tag{4.45}$$

which is a prediction based on the observations up to epoch $k-1$.

Taking the second-derivative terms into consideration, the estimate that minimizes the cost $J$ is in the range $\begin{bmatrix} \tilde{x}_k & \hat{x}_k^{+(0)} \end{bmatrix}$, which maps the optimal a priori estimate for epoch $k+1$ into $\begin{bmatrix} \tilde{x}_{k+1}^{-(0)} & \tilde{x}_{k+1}^{+(0)} \end{bmatrix}$, and estimation of processing noise into $\begin{bmatrix} 0 & \hat{w}_k^{+(0)} \end{bmatrix}$.

A step-size decaying method is employed to search the locally optimal estimation. This

approach is more reliable than the use of Hessian matrix in Psiaki & Jung (2002), and saves the power to update the Hessian matrix at each iteration. The optimal solutions are $\hat{x}_k \in \left[ \tilde{x}_k \quad \tilde{x}_k + r_{decay}\left(\hat{x}_k^{+(0)} - \tilde{x}_k\right) \right]$ , $\tilde{x}_{k+1} \in \left[ \tilde{x}_{k+1}^{-(0)} \quad \tilde{x}_{k+1}^{-(0)} + r_{decay}\left(\tilde{x}_{k+1}^{+(0)} - \tilde{x}_{k+1}^{-(0)}\right) \right]$ , and $\hat{w}_k \in \left[ 0 \quad r_{decay} \cdot \hat{w}_k^{+(0)} \right]$, where $r_{decay} \in (0,1)$ defines the step size. This algorithm is realized by the iteration as

$$\begin{cases} \hat{x}_k^{(j)} = \tilde{x}_k + r_{decay}^j \left(\hat{x}_k^{+(0)} - \tilde{x}_k\right) \\ \tilde{x}_{k+1}^{(j)} = \tilde{x}_{k+1}^{-(0)} + r_{decay}^j \left(\tilde{x}_{k+1}^{+(0)} - \tilde{x}_{k+1}^{-(0)}\right) \\ \hat{w}_k^{(j)} = r_{decay}^j \hat{w}_k^{+(0)} \end{cases} \tag{4.46}$$

in order to force the cost decrease if necessary, where $j$ is a natural integer incrementing from 1.

According to the aforementioned derivation, the optimal priori and posteriori values can be obtained to drive the KF estimator. In the context of weak signal tracking, the BPSK modulation is corrupted by strong noise, increasing the uncertainty in determining the polarization of navigation bits. The DD loop, however, reveals the degradation in tracking performance because the increase in BER at weak signal condition yields a larger bias to measure the phase, as in Figure 4-6. The DD discriminator determines the bit sign based on the accumulated correlations at I branch up to one data period. The incorrect determination, in the low $C/N_0$ region, results in cycle slip occurrence and in severe cases loss of lock (Yu et al. 2006c). Therefore, Psiaki & Jung (2002) adopts the Bayesian approach to treat the uncertainty of the data bits. This method simultaneously runs two KF carrier estimators. One estimator propagates the state and performs an update under

the assumption that $d_{m,k} = 1$ (Humphreys et al. 2005); the other operates in a similar manner under the assumption that $d_{m,k} = -1$. In real applications, the pair of KFs can run independently using two threads, and thus can propagate in parallel. The residual between the estimated measurement and observation is used to determine the a posteriori probabilities for each bit sign assumption. These a posteriori probabilities, in turn, are used to synthesize an optimal combination that drives the NCO of the PLL in the sense of minimum mean square error (MMSE).

Suppose that the final results from eq. (4.46) are $\tilde{x}_{k+1}^{(+)}$ and $\tilde{R}_{xxk+1}^{(+)}$ (Psiaki & Jung 2002) for the assumption that the navigation bit is +1; therefore the solution $\tilde{x}_{k+1}^{(-)}$ and $\tilde{R}_{xxk+1}^{(-)}$ denotes the alternative assumption of $d_{m,k} = -1$. Eq. (4.35) provides the cost to each of the solutions, termed $J_{min}^{(+)}$ and $J_{min}^{(-)}$. The cost function reflects the misclosure between the assumption and actual observation; therefore, the a posteriori probabilities for alternative bit sign can be inversely correlated with the costs under both assumptions, i.e. the correct hypothesis produces less cost and vice versa. Psiaki & Jung (2002) presents a robust way to measure the probabilities, which includes the confidence of the bit sign decision. The a posteriori probabilities ( $\hat{p}_{k+1}^{(+)}$ and $\hat{p}_{k+1}^{(-)}$), based on the observation up to epoch $k$, depend on the a priori probability ( $p_k^{(+)}$ and $p_k^{(-)}$), where the observation at epoch $k$ is not used. The calculation of $\hat{p}_{k+1}^{(+)}$ and $\hat{p}_{k+1}^{(-)}$ is clearly given in Psiaki & Jung (2002). The a priori probabilities are determined as (Psiaki & Humphreys 2006)

$$p_{k+1}^{(s)}\Big|_{s=+/-} = \begin{cases} 0.5 & \left(\textit{epoch } k+1 \textit{ is the start of a bit}\right) \\ \hat{p}_k^{(s)}\Big|_{s=+/-} & \left(\textit{epoch } k+1 \textit{ isn't the start of a bit}\right) \end{cases} \tag{4.47}$$

, which means there is no preference for either +1 or -1 at the start of a bit. The probabilities are cumulatively updated along with the observation updates within one data bit.

The Bayesian law then yields a linear weighted combination that minimizes the MSE on condition of the a posteriori estimates. The synthesized estimate is

$$\tilde{x}_{k+1}^{mix} = \hat{p}_{k+1}^{(+)} \tilde{x}_{k+1}^{(+)} + \hat{p}_{k+1}^{(-)} \tilde{x}_{k+1}^{(-)} \tag{4.48}$$

and the synthesized covariance matrix is

$$\tilde{P}_{k+1}^{mix} = \sum_{s=+/-} \hat{p}_{k+1}^{(s)} \left[ \tilde{P}_{k+1}^{(s)} + \left( \tilde{x}_{k+1}^{(s)} - \tilde{x}_{k+1}^{mix} \right) \left( \tilde{x}_{k+1}^{(s)} - \tilde{x}_{k+1}^{mix} \right)^T \right] \tag{4.49}$$

(Psiaki & Jung 2002). This mixing process characterizes the nature of the bit uncertainty. Additionally, this synthesis is equivalent to a “soft-decision” PD as opposed to the DD discriminator.

Derivation of the synthesized state is straightforward, as shown in eq. (4.48). While the covariance estimate, eq. (4.49), consists of two components: the weighted sum of two covariance and terms that increases the covariance due to the difference between the mixed estimate and the estimation under the two-bit sign assumption. One of these estimates is better than the mixed product if the bit sign is known. The unknown bit increases the uncertainty of the estimate. In order to propagate the extended KF-based PLL in the context of SRIF, it is assumed that

$$\tilde{P}_{k+1}^{mix} = \left( \tilde{R}_{k+1}^{mix^T} \tilde{R}_{k+1}^{mix} \right)^{-1} = \tilde{R}_{k+1}^{mix^{-1}} \left( \tilde{R}_{k+1}^{mix^{-1}} \right)^T \tag{4.50}$$

and eq. (4.49) becomes

$$\tilde{R}_{k+1}^{mix^{-1}}\left(\tilde{R}_{k+1}^{mix^{-1}}\right)^T = \hat{p}_{k+1}^{(+)}\left(\tilde{R}_{k+1}^{(+)}\right)^{-1}\left\{I + \tilde{R}_{k+1}^{(+)}\left(\tilde{x}_{k+1}^{(+)} - \tilde{x}_{k+1}^{mix}\right)\left[\tilde{R}_{k+1}^{(+)}\left(\tilde{x}_{k+1}^{(+)} - \tilde{x}_{k+1}^{mix}\right)\right]^T + \frac{\hat{p}_{k+1}^{(-)}}{\hat{p}_{k+1}^{(+)}}\tilde{R}_{k+1}^{(+)}\left(\tilde{R}_{k+1}^{(-)}\right)^{-1}\left[\tilde{R}_{k+1}^{(+)}\left(\tilde{R}_{k+1}^{(+)}\right)^{-1}\right]^T + \frac{\hat{p}_{k+1}^{(-)}}{\hat{p}_{k+1}^{(+)}}\tilde{R}_{k+1}^{(+)}\left(\tilde{x}_{k+1}^{(-)} - \tilde{x}_{k+1}^{mix}\right)\left[\tilde{R}_{k+1}^{(+)}\left(\tilde{x}_{k+1}^{(-)} - \tilde{x}_{k+1}^{mix}\right)\right]^T\right\}\left[\left(\tilde{R}_{k+1}^{(+)}\right)^{-1}\right]^T \tag{4.51}$$

Therefore,

$$\tilde{R}_{k+1}^{mix^{-1}} = \sqrt{\hat{p}_{k+1}^{(+)}}\left(\tilde{R}_{k+1}^{(+)}\right)^{-1}\left[I,\ \ \tilde{R}_{k+1}^{(+)}\left(\tilde{x}_{k+1}^{(+)} - \tilde{x}_{k+1}^{mix}\right),\ \sqrt{\frac{\hat{p}_{k+1}^{(-)}}{\hat{p}_{k+1}^{(+)}}}\tilde{R}_{k+1}^{(+)}\left(\tilde{R}_{k+1}^{(+)}\right)^{-1},\ \sqrt{\frac{\hat{p}_{k+1}^{(-)}}{\hat{p}_{k+1}^{(+)}}}\tilde{R}_{k+1}^{(+)}\left(\tilde{x}_{k+1}^{(-)} - \tilde{x}_{k+1}^{mix}\right)\right] = \sqrt{\hat{p}_{k+1}^{(+)}}\left(\tilde{R}_{k+1}^{(+)}\right)^{-1}\bar{R} \tag{4.52}$$

which satisfies eq. (4.49). The QR factorization results in

$$\bar{R} = \left[\breve{R} \quad 0\right]\breve{Q} \tag{4.53}$$

where $\breve{R}$ is the upper triangle matrix and $\breve{Q}$ is a unit orthogonal matrix. Therefore, the synthesized square-root information matrix becomes

$$\tilde{R}_{k+1}^{mix} = \sqrt{\frac{1}{\hat{p}_{k+1}^{(+)}}}\breve{R}^{-1}\tilde{R}_{k+1}^{(+)} \tag{4.54}$$

(Psiaki & Jung 2002), which drives the propagation of the EKF-PLL.

To avoid numerical overflow resulting from the very small probability values in the denominator of eq. (4.52), the aforementioned calculation assumes that $\hat{p}_{k+1}^{(+)} \geq \hat{p}_{k+1}^{(-)}$. For the case that $\hat{p}_{k+1}^{(+)} < \hat{p}_{k+1}^{(-)}$, then eqs. (4.52) and (4.53) can take the same form except interchanging the $(+)$ and $(-)$ superscripts.

Again, the Bayesian synthesis is critical to successful implementation of the extended KF carrier tracker for low $C/N_0$ . The bit sign, under such cases, is difficult to determine. The Bayesian approach achieves a compromised solution, superior to the one in which the bit sign is mistakenly estimated, while inferior to the one in which the bit sign is correctly determined. The Bayesian solution is optimal in the sense of MMSE.

### 4.2.3 Performance evaluation of Extended KF based Carrier Tracking

Due to the soft mode in dealing with uncertainty of the bit sign, an extended KF based tracker is expected to exceed the CBPLL in sensitivity. Figure 4-20 compares the threshold behavior of CBPLLs and extended KF-based PLL in the presence of additive WGN. The phase tracking error is based on 50 numerical trials, each with a 10 second data segment. The tracking error originating from the CBPLLs cannot be examined for $C/N_0$ values lower than 23 dB-Hz, because cycle slips occur in every trial. This is shown in Figure 4-21. Compared with Figure 4-13 (Kaplan configuration), Figure 4-21 proves that the extended KF-based tracker has an improvement of about 4 dB in mitigating cycle slips. As the Stephen & Thomas design shows another 1 to 1.5 dB improvement in mitigating the cycle slip (Figure 4-13), the improvement by extended KF decays to 2.5 - 3 dB once the root-controlled approach is used to build the digital CBPLLs.

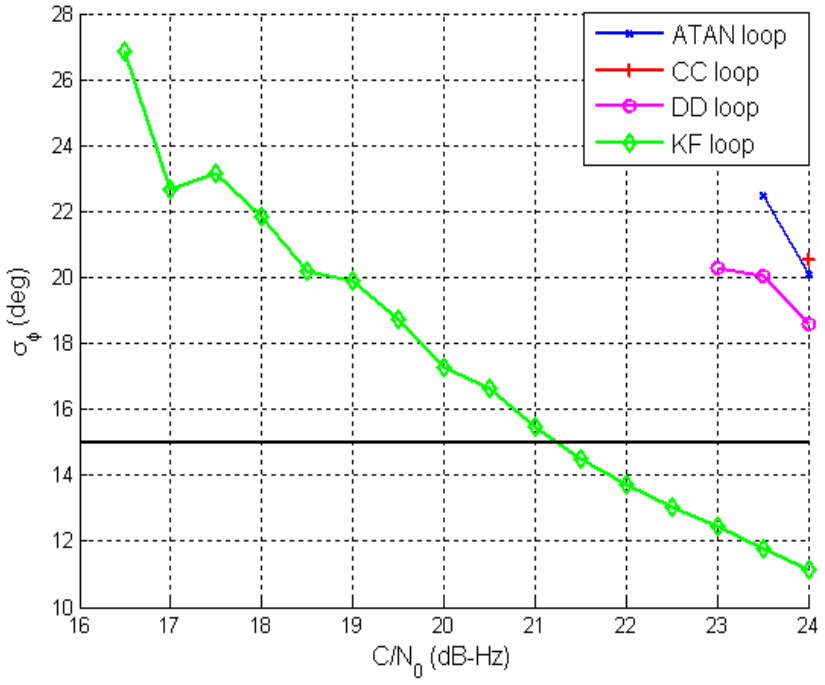


Figure 4-20: Phase tracking error at very low $C/N_0$

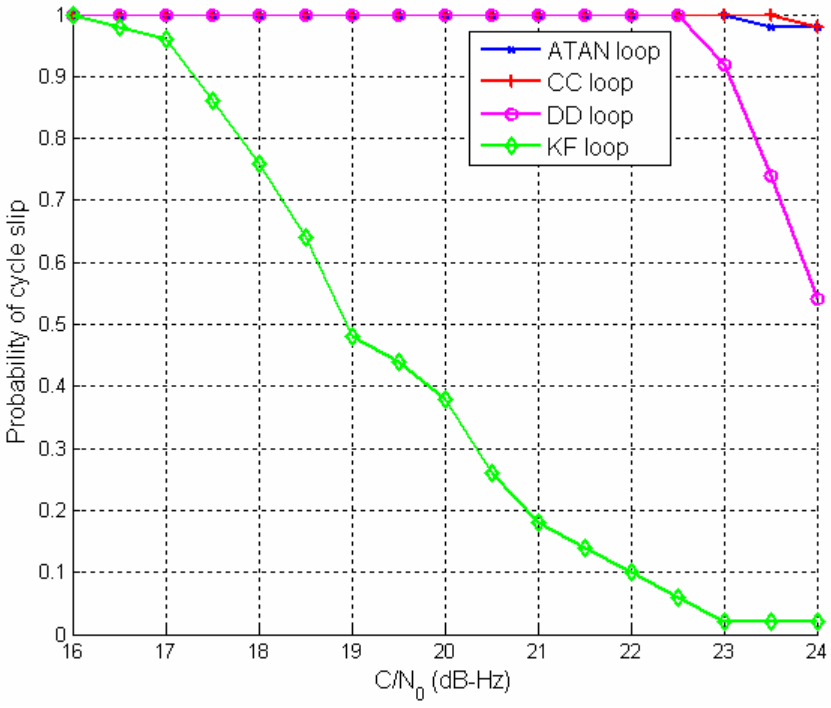


Figure 4-21: Percentage of cycle slips at very low $C/N_0$

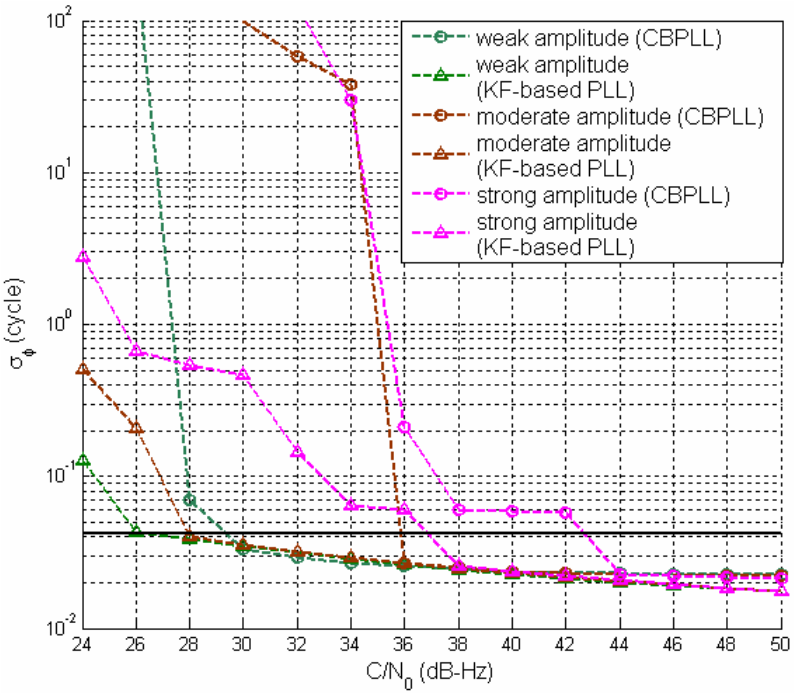


Figure 4-22: Phase tracking performance of a KF-based PLL against a CBPLL in the presence of ionospheric scintillation

In the presence of ionospheric scintillation, the extended KF-based PLL allows a more reliable tracking capability as opposed to the CBPLLs. Figure 4-22 shows that the KF approach improves the tracking sensitivity by 4 dB in the presence of the superficial power fades caused by weak scintillation. This result corresponds well with those presented in Figure 4-20 and Figure 4-21 because the additive WGN dominates the carrier tracking behavior. When strong amplitude scintillation occurs, the KF-based tracking loop reveals a 7 dB improvement. Due to the soft-decision, this result proves that the KF method exihibits a good potential to work in high dynamic applications. As shown in Figure 4-17, the carrier tracking divergence is more sensitive to SNR degradation than to rapid phase variations; this technique becomes more advantageous to build a scintillation monitoring reference receiver. The CBPLLs refered in this section are built on Kaplan

configuration with 15 Hz loop bandwidth.

# Chapter 5 Conclusions and Recommendation for Future Work

## 5.1 Conclusions

By implementing new mathematical models using software simulations rigorous mathematical analysis, this work demonstrates that DFC outperforms the conventional NCH approach during the acquisition of weak GPS signals. The processing loss induced by NCH can be decreased through the use of DFC by approximately 2.5 dB at low $C/N_0$ values. This improvement suggests promising potential to reduce the acquisition time. A Monte Carlo simulation verified theoretical predictions.

Statistical properties including probability of false alarm and probability of detection are essential to set a detection threshold, which identifies a decision variable level (and corresponding signal to noise ratio) beyond which a desired performance of acquisition and tracking can be achieved. Conditional PDFs of the DFC-based DV are necessary to analyze detector performances in a statistical sense, but are too complicated to express in a closed-form formula. Based on the statistical expectation and variance of the decision variable, this work uses curve fitting to approximate conditional PDFs produced by Monte Carlo simulations. The curve-fitting results, although not rigorously accurate, can provide a practical reference for this complex problem. Analysis of the resultant conditional PDFs substantiates that, due to the lower processing loss, the DFC is superior to

NCH in improving the sensitivity by 1.2 to 1.6 dB provided the false alarm is fixed to 0.1% and the detection threshold is set to 90%.

To enable better carrier tracking, the performance of several carrier configurations is evaluated for wideband GPS data with inclusion of selected interferences. A six-state dynamic model driven by Gaussian-distributed random samples is used to simulate the PHN resulting from an imperfect crystal unit. The numerical verification proves that the noise samples satisfy the expectation in a statistical sense. An ionospheric scintillation model is implemented and verified to replicate the power and phase variations induced by ionospheric irregularities.

CBPLLs and adaptive bandwidth loops are examined theoretically, based on the model, and results are then validated using the simulated wideband samples. Discriminators have a critical impact on carrier tracking capability, due to the severe bias induced by the nonlinear characteristics and the increase in noise variance resulting from the nonlinear operation. Four discriminators, commonly used in a GPS carrier tracking unit, are investigated from a statistical sense. The results provide an insight into the worse performance of the ATAN loop and the best behaviour of DD loop in low SNR conditions. The conventional digital filter design, obtained from its analog counterpart through binear or box-car transform, causes a deviation of the loop bandwidth and noise bandwidth. Under such circumstances, the loop performs worse than the theoretical prediction or even reveals unstable behaviour. Root-controlled design provides an effective solution; this configuration improves the sensitivity by about 1.5 dB. A KF-based tracking approach, com-

pared with 15 Hz constant-bandwidth loops, lowers the lock threshold by 7 dB in the presence of strong ionospheric scintillation; this suggests potential for application during occurrence of ionospheric scintillation. The improvement benefits from the soft treatment of the ambiguity of the bit sign, and from the optimal estimation by the Kalman filter in minimizing the MSE. During weak scintillation or in its absence , the tracking strategy for the KF demonstrates a 4 dB improvement in tracking sensitivity and immunity to cycle slips.

## 5.2 Recommendation for Future Work

The analysis in Chapter 3 neglects the MAI caused by the coexisting signals from other satellites. However, the cross-correlation peaks are detrimental to acquire and track weak signals in the presence of strong channels. Successive interference cancellation provides a way to partially eliminate this type of disturbance; nevertheless the residual between the local reconstruction and the incoming signal will degrade the detection performance (Progri et al. 2006). Thus far, the blind channel idenfication has been extensively investigated to jointly estimate the parameters for multiple signals. This approach cannot only detect the weak signal that is 15 dB lower than the coexisting strong signal (Progri et al. 2006), but also identify the multipath parameters for each channel (Amleh & Li 2005). The classification of multipath delays can improve the accuracy of the pseudorange measurements. The major limitation of this algorithm to be adopted widely arises from the high processing power requirements. With the development of high-end processors

and the innovation to simplify the numerical computation, this method is promising to build advanced GPS receivers. Since the KF based tracking strategy shows an attractive improvement in term of sensitivity, the further evaluation of this algorithm under the real scintillation samples provides a valuable reference to build them into a commercial receiver.

# REFERENCES

Abramowitz, M. and I.A. Stegun (1965), Handbook of Mathematical Functions, Dover Publications, NY

Allan, D.W. (1987), Time and Frequency (Time-Domain) Characterization, Estimation, and Prediction of Precision Clocks and Oscillators, in *IEEE Transactions. On Ultrasonics, Ferroelectrics, and Frequency Control*, Vol. UFFC-34, No. 6, pp.647-654

Amleh, K. and H. Li (2005) Joint Estimation of Carrier offser and Code timing for DS-CDMA with Performance analysis in IEEE Transactions on Wireless Communication, Vol. 4, No. 5, pp 1980-1987

Barker, B. C. et al. (2000) "Overview of the GPS M Code Signal," in *Proceedings of ION 2000 National Technical Meeting*, 26-28 January, Anaheim, CA, pp. 542-549, Institute of Navigation.

Bastide, F., O. Julien, C. Macabiau, B. Roturier (2002), "Analysis of L5/E5 Acquisition, Tracking and Data Demodulation Thresholds," in *Proceedings of ION GPS/GNSS*, 24-27 September, Portland OR, pp.2196-2207

Betz, J.W. (2002) "Binary Offset Carrier Modulations for Radionavigation," Navigation: Journal of the Institute of Navigation, Vol. 48, Number 4, Winter 2001, pp. 227-246.

Bierman, G. J. (1977), Factorization Methods for Discrete Sequential Estimation, Academic Press, NY

Cannon, M. E. (2005) *Satellite Positioning*, ENGO 561 Course Notes, Department of Geomatics Engineering, University of Calgary, Canada

Cannon, M. E., G. Lachapelle , G. MacGougan , R. Klukas , P. Boulton , and A. Read (2003) *Mobile Telephony: Testing a High Sensitivity GPS Receiver in Weak Signal Environment*, GPS World, Mar. 1

Chaffee, J. W.,(1987), Relating the Allan Variance to the Diffusion Coefficients of a Linear Stochastic Differential Equation Model for Precision Oscillators, in *IEEE Transactions On Ultrasonics, Ferroelectrics, and Frequency control*, Vol. UFFC-34, No. 6, pp. 655-658

Chang, H. (1982), "Presampling Filtering, Sampling and Quantization Effects on Digital Matched Filter Performance, " in *Proceedings of the International Telemetering Conference*, San Diego, CA, pp. 889-915

Choi. H., D.J. Cho, S.J. Yun, Y. B. Kim, and S. J. Lee (2002) “A Novel Weak Signal Acquisition Scheme for Assisted GPS,” in *Proceedings of ION GPS/GNSS*, 24-27 September, Portland, OR, pp. 177-183.

Conker, R. S., M. B. El-Arini, C. J. Hegarty and T. Hsiao (2003), Modeling the effects of ionospheric scintillation on GPS satellite-based augmentation system availability, in *Radio Science*, Vol. 38, No. 1

Davis, J. A., C. A. Creenhall, and P. W. Stacey, (2005), A Kalman filter clock algorithm for use in the presence of flicker frequency modulation noise, *Metrologia 42*, Institute of Physics Publishing, pp. 1-10

Directorate-General Energy and Transportation (2006), *Program Phases of European Satellites Navigation System*, http://europa.eu.int/comm/dgs/energy_transport/galileo/programme/phases_en.htm#3, last assessed Feb. 6, 2006

Doherty, P. H., S. H. Delay, C. E. Vallardes, and J. A. Klobuchar (2000) “Ionospheric Scintillation Effects in the Equatorial and Auroral Regions,” in *Proceedings of ION GPS/GNSS*., 19-22 September, Salt Lake City, UT, pp 662-671

Dong, L. (2003) *IF GPS Signal Simulator Development and Verification*, MSc Thesis, Department of Geomatics Engineering, University of Calgary, Canada (Available at http://plan.geomatics.ucalgary.ca)

Enge P., and A. J. Van Dierendonck (1996), “Wide Area Augmentation System,” [Chapter 4] in *Global Positioning System: Theory and Application*, Volume II, Astronautics and Aeronautics, Washington D.C, pp. 117-142.

European Commission (1999), *GALILEO Involving Europe in a New Generation of Satellite Navigation Services*, COM 54 Final, May 7

Fenton, P. and J. Jones (2005), “The Theory and Performance of NovAtel Inc.’s Vision Correlator,” in in *Proceedings of ION GPS/GNSS*., 13-16 September, Long Beach, CA, 9 pages.

Gierkink, S. L. J. (1999), *Control Linearity and Jitter of Relaxation Oscillators*, Eindhoven, The Netherlands

Glennon, E. P. and A. G. Dempster (2004), “A Review of GPS Cross Correlation Mitigation Techniques,” in *Proceedings of the International Symposium on GNSS/GPS*, 6-8 December, Sydney, Australia, pp 125-137

GPS World (2005), *GNSS on Stage*, GPS World, Jan 1.

Hajimiri, A. and T. H. Lee (1998) “A General Theory of Phase Noise in Electrical Oscillators,” *IEEE Journal of Solid-State Circuits*, vol. 33, no. 2, February, pp. 179-194

Hegarty, C., M.B. El-Arini, T. Kim, and S. Ericson (2001) Scintillation modeling for GPS/Wide Area Augmentation System receivers, in *Radio Science*, Vol.36, No.5, pp 1221-1231

Hoffman-Wellenhof, B., H. Lichtenegger, & J. Collins (2001) *GPS Theory and Practice.* Springer-Verlag Wein, New York NY.

Holtzman, J. M. (1994) “DS/CDMA Successive Interference Cancellation,” in *Proceedings. of IEEE Third International Symposium on ISSSTA*, 4-6 July, 1994, pp.69-78

Humphreys, E. D., M. L. Psiaki, and P. K. Kinter, Jr., (2005), “GPS Carrier Tracking Loop Performance in the Presence of Ionospheric Scintillation,” in *Proceedings of ION GPS/GNSS*, 13-16 Sept., Long beach CA, pp. 156-166, Institute of Navigation

ICD200C (2000) *NAVSTAR GPS Space Segment / Navigation User Interfaces*, GPS Interface Control Document.

Irsigler, M and B. Eissfeller (2002), “PLL Tracking Performance in the Presence of Oscillator Phase Noise,” *GPS Solutions*, Vol. 5, No. 4, Wiley Periodicals, Inc. NY, pp 45-57

Julien, O. (2005) *Design of Galieo L1F Receiver Tracking Loops*, Ph.D Thesis, Department of Geomatics Engineering, University of Calgary, Canada, pp. 1-15 (Available at http://plan.geomatics.ucalgary.ca)

Kaplan, E.D. & C. J. Hegarty (2006) *Understanding GPS Principles and Applications*, 2nd Ed., Artech House, Norwood MA.

Kaplan, E.D. (1996) *Understanding GPS Principles and Applications*, Artech House, Norwood MA.

Kay, S.M.(1998), *Fundamentals of Statistical Signal Processing: Detection Theory,* Vol II, Prentice Hall PTR, RI.

Klobuchar, J. A. (1996), “Ionospheric Effects on GPS,” [Chapter 12] in *Global Positioning System: Theory and Applications*, Vol I, American Institute of Aeronautics and Astronautics, Washington D.C pp 499- 500

Klukas, R., O. Julien, L. Dong, M.E. Cannon, and G. Lachapelle (2004) Effects of Building Materials on UHF Ranging Signals. **GPS Solutions,** 8, 1, 1-8.

Kohno, R., M. Hatori, and H. Imai, (1983), "Cancellation Techniques of Co-Channel Interference in Asynchronous Spread Spectrum Multiple Access Systems," Electronics and Communications, Vol. 66-A, No.5, pp 20~29

Kovach, K, and K. Van Dyke (1997) "GPS in Ten Years," in *Proceedings of the US Institute of Navigation GPS Conference,* Sept. 16-19, Kansas City, MS, USA, pp. 1251-1259.

Kristensson, M. and B. Ottersten (2001) "Optimum Subspace Methods," [Chapter 5] in *Signal Processing Advances in Wireless & Mobile Communications*, Vol I, Prentice-Hall, Inc. pp139-174

Lachapelle, G. (2005) *Advanced GPS Theory and Applications*, ENGO 625 Course Notes, Department of Geomatics Engineering, University of Calgary, Canada

Lindsey, W. C. and C. M. Chie (1981), "A Survey of Digital Phase-Locked Loops," in *Proceedings of the IEEE,* Vol. 69, No. 4, pp 410-431, April.

Liu, J. (2003) *Implementation and Analysis of GPS Ambiguity Resolution Strategies in Single and Multiple Reference Station Scenarios*, MSc Thesis, Department of Geomatics Engineering, University of Calgary, Canada (Available at http://plan.geomatics.ucalgary.ca)

Lowe, S.T. (1999), *Voltage Signal-to-Noise Ratio (SNR) Nonlinearity Resulting From Incoherent Summations*, TMO Progress Report 42-137, Tracking Systems and Application Section, 6 pages

MacGougan, G., G. Lachapelle, R. Klukas, K. Siu, L. Garin, J. Shewfelt, and G. Cox (2002) Performance Analysis of A Stand-Alone High Sensitivity Receiver. GPS Solutions, Springer Verlag, 6, 3, 179-195.

Misra, P. and P. Enge, (2001) *Global Positioning System- Signals, Measurements, and Performance*, Ganga-Jamuna Press, Lincoln, Massachusetts

Norman, C. P., and C. R. Cahn (2005) *Strong Signal Cancellation to Enhance Processing of Weak Spread Spectrum Signal*, US Patent 0032513, 7 pages.

Olynik, M (2003), *Temporal Characteristics of GPS Error Sources and Their Impact on Relative Positioning*, MSc. Thesis, Department of Geomatics Engineering, University of Calgary, Canada, (available at http://www.geomatics.ucalgary.ca/links/GradTheses.html.)

Onidi, O. (2002), *Launching Galileo*, http://www.gpsworld.com/gpsworld/article/articleDetail.jsp?id=118805, last accessed

Parkinson, B. W. and J. J. Spilker, eds. (1996) *Global Positioning System: Theory and Applications.* American Institute of Aeronautics and Astronautics, Inc., Washington DC.

Petrovski, I., S. Kawaguchi, H. Torimoto, B. Townsend, S. Hatsumoto, K. Fuji (2002) "An Impact of High Ionospheric Activity on MultiRef RTK Network Performance in Japan" in *Proceedings of ION GPS/GNSS.*, 24-27 September, Portland, OR, pp 2247-2255

Pomerantz, S. D. (2002) *E911 Caller Location ? Only the Beginning*, GPS World, Jul. 1

Progri, I. F., M. C. Bromberg, and W. R. Michalson (2006) Maximum-Likelihood GPS Parameter Estimation in *Journal of the Institude of Navigation*, Vol. 52, No. 4, pp 229-238.

Psiaki, M. L. (2001a) "Block Acquisition of Weak GPS Signals in a Software Receiver," in *Proceedings of ION GPS/GNSS.*, 11-14 September, Salt Lake City, UT, pp 2838-2850

Psiaki, M. L. (2001b) "Smoother-Based GPS Signal Tracking in a Software Receiver," in *Proceedings of ION GPS/GNSS.*, 11-14 September, Salt Lake City, UT, pp 2900-2913

Psiaki, M. L. and H. Jung(2002) "Extended Kalman Filter Methods for Tracking Weak GPS Signals," in the *Proceedings of ION GPS/GNSS*, 24-27 September, Portland OR, pp. 2539-2553, the Institute of Navigation.

Psiaki, M. L. and Humphreys, T. E. (2006) Personal communication for implementation of extended Kalman filter based tracking loops

Pullen, S., Opshaug, G., Hansen, A., Walter, T., Enge, P. and B. Parkinson, B (1998)., A preliminary study of the effect of ionospheric scintillation on WAAS user availability in equatorial regions, *Proceedings of the ION GPS* , 15-18 Sept, Alexandria, VA, pp 687-699

Raquet, J. (2006) *Advanced GNSS Receiver Technology*, ENGO 699.45 Course Notes, Department of Geomatics Engineering, University of Calgary, Canada,

Ray, J. K. (2005) *Advanced GPS Receiver Technology*, ENGO 699.73 Course Notes, Department of Geomatics Engineering, University of Calgary, Canada, pp. 291-421

Ray, J. K. (2000) *Mitigation of GPS Code and Carrier Phase Multipath Effects Using a Multi-Antenna System*, PhD Thesis, Department of Geomatics Engineering, University of Calgary, Canada (Available at http://plan.geomatics.ucalgary.ca)

Skone, S., G. Lachapelle, D. Yao, W. Yu, and R. Watson (2005) " Investigating the Impact of Ionospheric Scintillation using a Software Receiver," in *Proceedings of ION GPS/GNSS*, 13-16 Sept, Long Beach CA, pp 1126-1137

Stephens, D. R. (2002) *Phase-Locked Loops for Wireless Communications: Digital, Analog and Optical Implementations*, 2nd Ed. Kluwer Academic Publishers, Norwell MA.

Stephens, S.A. and J.B. Thomas (1995) Controlled-Root Formulation for Digital Phase-Locked Loops in *IEEE Transactions on Aerospace and Electronic Systems*, Vol.31, No. 1 pp 78-95

Sugrue, T. J., (2001) *Hearing on Wireless E911*, Before the Subcommittee on Communications of the Senate Committee on Commerce, Science and Transportation, United States Senate, 12 pages

Toran-Marti, F., and J. Ventura-Traveset (2004) "The ESA EGNOS Project: The First Step of the European Contribution to the Global Navigation Satellite System (GNSS)," NAVIGARE Conference, June 18, Winterthur, Switzerland.

U.S. Department of Defense, (2001), *Global Positioning System Standard Positioning Service Performance Standard* USA.

Vig, J. R. (1992), *Introduction to Quartz Frequency Standards*, http://www.ieee-uffc.org/freqcontrol/quartz/vig/vigcomp.htm, last assessed Oct. 1992

Viterbi, A. J. (1966) *Principle of Coherent Communication*, McGraw-Hall NY

Viterbi, A. J. (1963) "Phase-locked Loop Dynamics in the Presence of Noise by Fokker-Planker Techniques," in *Proceedings of IEEE*, vol. 51, no. 2, pp 1727-1753 December.

Watson, J. R. A. (2005) *High-Sensitivity GPS L1 Signal Analysis for Indoor Channel Modelling*, MSc Thesis, Department of Geomatics Engineering, University of Calgary, Canada, pp. 104-182 (Available at http://plan.geomatics.ucalgary.ca )

Weinberg A. and B. Liu (1974), Discrete Time Analysis of Nonuniform Sampling First- and Second-Order Digital Phase Lock Loops, in *IEEE Trans. on Communications*, Vol. 22, No. 2, pp123-137.

Yu, W. (2006a) *Appendix_to_Scint_Noise_OscJitter_PLL_WeiY_16Jan06*, Internal Reports, PLAN Group, The University of Calagry, Calgary AB.

Yu, W., B. Zheng, R. Watson, G. Lachapelle, (2006b) Differential Combining for Acquiring Weak GPS Signals, in *EURASIP Journal on Signal Processing*,

doi:10.1016/j.sigpro.2006.08.004.

Yu, W., G. Lachapelle, S. Skone (2006c) " PLL Performance for GPS Signals in the Presence of Thermal Noise, Phase Noise, and Ionospheric Scintillation," in *Proceedings of ION GPS/GNSS*, 26-29 Sept., Fort Worth, TX, in press (17 pages)

Zarrabizadeh, M.H., and E.S. Sousa (1997), A Differentially Coherent PN Code Acquisition Receiver for CDMA Systems, in *IEEE Transactions on Communication*,Vol. 45, No. 11, pp.1456~1465

Zheng, B. (2006) Personal communication

Zheng, B. (2005) "GPS Software Receiver Enhancements for Indoor Use," in *Proceedings of ION GPS/GNSS*, 13-16 September, Long Beach, CA, pp. 1138-1142, Institute of Navigation.

Ziemer, R.E. and W.H. Tranter (2002), *Principles of Communication*, John Wiley & Sons, N.J

Zucca, C., and P. Tavella, (2005), The Clock Model and Its Relationship with Allan and Related Variances, in *IEEE Transactions On Ultrasonics, Ferroelectrics, and Frequency Control*, Vol. 52, No. 2, pp. 289-296

# Appendix A

# GPS Background

## **A.1** GPS Overview

The Global Positioning System (GPS) is a space-based radio navigation system originally developed by DoD as a military force enhancement system in 1973 (Lachapelle et al 2005). GPS comes into being based on the success of ground-based radio navigation systems such as LORAN (LOng RAnge Navigation system) and Omega and improvements of clock technology (Parkinson & Spilker 1996, Misra & Enge 2001). The latter can make it possible that time-synchronized signals be transmitted from satellites (Misra & Enge 2001). The objective in developing GPS was to offer an estimate of position, velocity, and time, for both military applications and civil use (Misra & Enge, 2001). The accuracy of the standard positioning service (SPS) is approximately 13 m in the horizontal and 22 m in the vertical at a 95% probability level (U.S. Department of Defense, 2001). GPS technologies have been progressing rapidly in the past decade, including various types of augmentation, receiver technologies, carrier phase ambiguity resolution, and advanced error mitigation or elimination approaches (Lachapelle 2005). GPS can provide a solution with accuracy ranging from metre to centimetre given the condition, measurements, and adopted methods (Misra & Enge 2001).

Currently, navigation messages are continuously transmitted over two L-band carriers termed as L1 and L2. The centre frequencies of L1 and L2 respectively are 1575.42 MHz and 1227.60 MHz (Cannon 2005). Two orthogonal signals are transmitted on L1, one for

civil users and another for DoD-authorized users. The signal broadcasted on L2 is only for authorized users (Parkinson & Spilker 1996). Every signal consists of carrier, ranging code, and navigation data. The carrier selection must account for path loss resulting from radio propagation, the influence of ionosphere and troposphere. A frequency in the L-band gives an acceptable received signal power and dual-carrier design permit to measure the ionospheric group delay (Parkinson & Spilker 1996). A binary-coded sequence with a pre-defined format contains information on ephemeris, parameters for satellite clock errors, satellite health status, and an almanac provides a reduced-precision ephemeris for all satellites operating around the orbit. Navigation bits are transmitted at a rate of 50 bps with a bit duration of 20 ms. The data signal is generated at a rate of 50 Hz, which is spread by multiplying a binary PRN valued by ±1. This form of spread spectrum is termed as direct sequence-spread spectrum (DS-SS) (Lachapelle 2005). The spreading-spectrum code has a clock rate of 1.023 MHz for the L1 C/A code and 10.23 MHz for the P code. GPS utilizes a DS-SS scheme because it provides a way to recover the timing and doppler shift by synchronizing local code and carrier replica with the received signals (Parkinson & Spilker 1996). The synchronization provides the essential information for normal and precise positioning. Besides the natural characteristics, the DS-SS system performs well in mitigating a narrow-band jamming or a tone interference with fixed power because the bandwidth of interference is broadened at the stage of correlation processing. To correlate the incoming pseudorandom spreading sequence with a local replica yields a triangular autocorrelation function. The correlation peak occurs when the local code perfectly aligns with that in the incoming signal, by which the timing information can be recovered from the signal (Misra & Enge 2001).

CDMA provides a solution where the multiple signals can be simultaneously accessed by the same frequency channels with minimal inter-channel interference. Multiple access capacity is very important for GPS as a receiver may simultaneously receive a composite signal from several satellites, wherein all signals occupy a common carrier channel (Parkinson & Spilker 1996). Assuming a perfect orthogonal property between a pair of PRN code, the inter-channel interference becomes null. However in many communication/ ranging tasks orthogonal signaling is almost impossible because the signal transmitters are by no means at identical distances from different users. To maximize the multiple access capacity and optimize the performance, the selected Gold pseudorandom codes share the same code length and are minimally correlated each other at all possible time offsets (Misra & Enge 2001).

Correlation, in general, measures the similarity of two waveforms (Misra & Enge 2001). Autocorrelation quantifies the similarity of any waveform with time shifts of itself, while cross-correlation reflects the similarity between a waveform with all time shifts of a second waveform. For binary sequence in the digital domain, the correlation is computed by simply summing the products of two digital sequences (Lachapelle 2005, Cannon 2005). The autocorrelation peak favors signal acquisition and multipath mitigation because it is far greater than the secondary peaks. The ratio of an autocorrelation peak to a secondary peak is proportional to the probability of detecting the correct peak. The received signal is always composed of the direct signal and other components that have traveled reflected paths (Lachapelle 2005). The true range information contained in the direct signal has to be extracted by receiver. The multipath signals however interfere the pseudorange measurements, because they also yield their own correlations that shadow the peak created by

the direct signal. Given that a multipath signal is delayed by more than one chip compared with the direct signal, the shadow peak can be entirely distinguished from the main correlation peak. Therefore, the short multipath limits the accuracy of GPS positioning. In indoor situations, the line-of-sight signal may not be available and the first reflected signal may be seen by the receiver as the “line-of-sight” signal.

## **A.2** Basic receiver technology

A basic GPS receiver is composed of an antenna, a RF frontend (FE), a signal processor, and a data processor. An antenna receives the RF GPS signal and filters out the interferences such as signals outside the desired band and reflected signals of left hand circular polarization (Ray 2005). Then the signal is strengthened by a low noise amplifier (LNA) housed in the antenna, and is fed into the FE. The FE down-converts the signal from L band to intermediate frequency and amplifies the signal to a workable level for digitization. A three-stage amplifier inside the FE, in general, contains at least one variable gain amplifier with a dynamic range of 30 to 40 dB. Automatic gain controller (AGC), which controls the gain of the variable gain amplifier, ensures the signal remains at a workable level required by the ADC. (Ray 2005). The ADC is a bridge between the analog and digital domain (Lachapelle 2005). Digitizing the analog signal results in a quantization distortion termed quantization loss; it decreases with an increase in number of quantization bits. The low-cost receiver is digitized by one or two bits, while a high-end or anti-jamming receiver always adopts a 2 to 8-bit ADC (Ray 2005).

OSC is a core component to drive the receiver to operate properly. It provides a basic reference frequency, on which a frequency synthesizer generates all the local frequencies

for both the RF FE and the signal processor. The frequency synthesizer is a PLL that forces the feedback frequency to lock on the reference frequency. The output frequency relates with the feedback frequency by a frequency divider; therefore by adjusting the parameters of the divider, one can generate the required output frequency. In conclusion, a high quality OSC can shorten the time to acquisition, improve the tracking capability, and increase the reliability and redundancy. However the significant cost and power consumption restricts the use of high quality OSC in commercial applications (Parkinson & Spilker 1996)

The signal processor demodulates the timing and navigation message from digital samples. It generates the pseudorange measurements based on the code NCO and the carrier phase measurements based on the carrier NCO and the cycle counter. To correctly decode the timing and navigation information necessary for measurements, a receiver should complete acquisition, tracking, $C/N_0$ estimation and bit synchronization serially.

COH and NCH integration are used to produce a statistical test for each cell in an uncertain region, which is defined by the possible Doppler due to LOS motion and aging drift of OSC, and code search step depending on the pull-in range of the DLL. For satellite-based positioning and communication, the signal is suppressed by the ambient noise; thus the integration processing is necessary to improve the SNR to meet the detection requirement. The performance of signal detection is associated with SNR of the statistical test, improved by COH and NCH approaches. In the context of stochastic signal detection, an optimal signal detector can be designed from statistical sense as the Neyman-Pearson criteria.

Signal tracking involves code wipe off and carrier wipe off. The DLL synchronizes the code phase of the local replica with the one of the incoming signal; thus the correlation process provides the dispreading gain by stripping off the PRN code of the incoming signal. The carrier tracking loop named FLL or PLL synchronizes the carrier frequency or phase with those of the incoming signals. Because of an half-cycle phase ambiguity, pure PLL does not fit GPS channels modulated by navigation message; therefore Costas loops are selected for the PLL in GPS receivers due to their insensitivity to data bit transition. Costas loops, however, introduce a squaring loss resulting from the nonlinear operation of the discriminator. The DLL operates with the carrier tracking loop in convoluted mode because the loss of lock occurring in one loop easily leads the other loop to lose lock. A PLL is a more vulnerable component than a DLL, as the dynamic stress for the DLL can be partially removed using the carrier Doppler estimated by the PLL.

Once a receiver keeps tracking the carrier phase and code offset of the incoming signal, it starts to detect the bit boundary named bit synchronization and to estimate the $C/N_0$. The estimation of $C/N_0$ is necessary because the latter $C/N_0$ is associated with the quality of tracking. Once the receiver loses lock, the estimated $C/N_0$ decreases rapidly.

A navigation processor detects the subframe preambles and then initializes the parity check on the demodulated data. The parity check is used to confirm that the demodulation process is free from errors. Once the resulting data passes through the check successfully, it is compiled into a set of meaningful parameters necessary for positioning computation. Least square and KF approaches are the most common methods to yield final solutions.